AFOSR-TR-97-0437

REPORT DOCUMENTATION PAGE	Form Approved OMB No. 0704-0188

1. AGENCY USE ONLY (*Leave blank*)	2. REPORT DATE	3. REPORT TYPE AND DATES COVERED
	May, 16 1997	October 1993-May 1997

4. TITLE AND SUBTITLE
The Control of Junction Flows

5. FUNDING NUMBERS
AFOSR F49620-93-1-0346

6. AUTHOR(S)
Dr. C. R. Smith
Dr. J. D. A. Walker

7. PERFORMING ORGANIZATION NAME(S) AND ADDRESS(ES)
Department of Mechanical Engineering and Mechanics
Lehigh University
354 Packard Laboratory, 19 Memorial Drive West
Bethlehem, Pennsylvania 18015

8. PERFORMING ORGANIZATION REPORT NUMBER
AFOSR

9. SPONSORING/MONITORING AGENCY NAME(S) AND ADDRESS(ES)
Air Force Office of Scientific Research (AFMC)
110 Duncan Avenue, Suite B115
Bolling Air Force Base, D. C. 20332-0001

10. SPONSORING/MONITORING AGENCY REPORT NUMBER

11. SUPPLEMENTARY NOTES

12a. DISTRIBUTION/AVAILABILITY STATEMENT
UNCLASSIFIED Approved for public release; distribution unlimited.

12b. DISTRIBUTION CODE

13. ABSTRACT (*Maximum 200 words*)

An experimental study of the effects of spatially-limited (i.e. localized) surface suction on unsteady laminar and turbulent junction flows was performed using hydrogen bubble flow visualization and Particle Image Velocimetry (PIV).

Results indicate that suction on the *laminar* system can effectively modify the flow topology and periodicity. Detailed analysis of laminar PIV results indicates that it is the impinging boundary layer instability which is the mechanism for vortex generation frequency in the unsteady laminar case. Application of external perturbations to the impinging boundary layer can be used to initiate "lock-on" of the vortex formation frequency to the forcing frequency over a narrow range of frequencies.

PIV results of *turbulent* junction flow indicate that surface suction effectively weakens both the instantaneous turbulent vortex and the associated surface interactions on the symmetry plane, can eliminate the *average* turbulent necklace vortex on the symmetry plane, and weakens the *average* downstream strength of the vortex. It was also determined that suction effectively reduces the Reynolds-stress levels in both the symmetry plane and cross-stream planes, as well as reducing the unsteady behavior of the turbulent vortex legs.

14. SUBJECT TERMS
Particle Image Velocimitry, PIV, Junction Flow, Horseshoe Vortices, Boundary Layers, Vortex Dynamics, Laminar Vortices, Turbulent Vortices

15. NUMBER OF PAGES
180

16. Price code

17. SECURITY CLASSIFICATION OF REPORT	18. SECURITY CLASSIFICATION OF THIS PAGE	19. SECURITY CLASSIFICATION OF ABSTRACT	20. LIMITATION OF ABSTRACT
Unclassified	Unclassified	Unclassified	UL

NSN 7540-01-280-5500

Standard Form 298 (Rev. 2-89)

FINAL REPORT
AFOSR GRANT NO. F49620-93-1-0346

The Control of Junction Flows

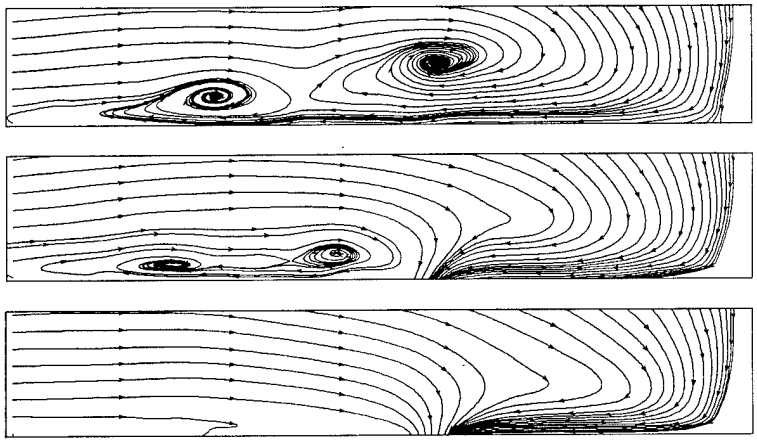

C. R. Smith and J. D. A. Walker
Dept. of Mechanical Engineering
Lehigh University
19 Memorial Dr. West
Bethlehem, PA 18015

May 1997

Executive Summary

Objectives

The current research focuses on the application of selected control methods to both laminar and turbulent junction flows in order to assess their usefulness for control and modification of the associated junction vortex system. Specifically, the effect of control on the unsteady behavior of the junction vortex, the strength of the vortex, and its downstream extensions are examined using flow visualization and Particle Image Velocimetry (PIV) in a water channel test environment. The appended thesis by C.V. Seal details the specific procedures and findings.

Laminar Flow Control

Control of an unsteady laminar necklace vortex system (formed at a cylinder-flat plate junction, in the breakaway regime) using constant-rate surface suction applied through a cross-stream slot of limited spatial extent was examined in detail using hydrogen bubble visualizations for suction rates up to 101% of the free-stream velocity U_∞ and various slot locations relative to the cylinder. It was determined that *control of this type is unable to completely eliminate the formation of a necklace vortex system.* However, it was observed that *this type of control scheme can be effective in modifying the behavior and topology* of the initial system. The modification generally takes one of four possible forms, depending on slot location and suction rate: 1) a segmentation of the unsteady necklace vortex system into two or more separate vortex systems; 2) the formation of a "braid" system, wherein a complicated interaction between two adjacent necklace vortices arises adjacent to the sides of the cylinder; 3) a modification of the strength and periodicity of the original vortex system; 4) an elimination of the advecting necklace vortex when it encounters the suction slot. Therefore, spatially-limited suction provides a viable alternative to the distributed suction methods of previous studies. It was also observed that the "braid" system displays discrete three-dimensional vortex-vortex and vortex-surface interactions reminiscent of those observed in turbulent boundary layers, making this system an ideal test-bed for the study of such three-dimensional interactions.

Analysis of detailed PIV data taken on the symmetry plane indicates that the *impinging boundary layer instability is the mechanism which dictates the frequency of the unsteady laminar system*, which suggests that the frequency of the unsteady laminar system is susceptible to control via external perturbations. Experiments showed that over a narrow range of frequencies, bracketing the natural formation/breakaway frequency, external perturbation of an unsteady laminar system can be used to override the natural formation/breakaway frequency.

In addition, several passive control devices (i.e. a fillet, control rings, and geometric modification of the flat plate), were cursorily examined using hydrogen bubble visualization to asses their impact on an unsteady laminar necklace vortex system. Interpretation of these results indicates that:

1. Control rings (circular disk-shaped fins mounted on the bluff body) can effectively modify a laminar, unsteady necklace vortex system by segmenting the original system into several smaller-scale steady and unsteady systems
2. A filleted cylinder can eliminate the unsteady necklace vortex system upstream of the cylinder, but residual, steady, vortex legs form outboard of the cylinder.
3. Location of a curved depression in flat plate upstream of a cylinder can modify the unsteady laminar necklace vortex system to a system composed of many steady vortices.

Turbulent Flow Control

The effect of spatially-limited constant-rate suction (ranging from 0% to 68% of the free-stream velocity U_∞) on a turbulent necklace vortex formed at the junction of a cylinder and flat plate was studied using PIV techniques, with data taken in the symmetry and three downstream, cross-stream, planes. Detailed analysis of these results indicates that use of spatially limited surface suction:

1. Weakens or eliminates the turbulent necklace vortex on the symmetry plane region;
2. Reduces the strength of the downstream extensions of the turbulent necklace vortex; however the effect of the suction apparently diminishes with streamwise distance;
3. effectively weakens the instantaneous vortex-surface interactions occurring within the vortex system;
4. reduces averaged Reynolds stress levels in the symmetry and downstream planes.

Therefore, spatially limited suction again provides a viable (and relatively simple) alternative to the distributed suction methods of previous studies.

Contract Information

Personnel Supported

J. D. A. Walker (Co-Principal Investigator)
C.R. Smith (Co-Principal Investigator)
M. Demir (Graduate Research Assistant)
C.V. Seal (Graduate Research Assistant)

Publications

Doligalski, T. L., Smith C. R. and Walker, J. D. A. 1994 "Vortex Interaction with Walls", *Annual Review of Fluid Mechanics* **26**, 574-616.

Smith, C. R. and Walker, J. D. A. 1995 "Turbulent Wall-Layer Vortices" in Fluid Vortices, S. I. Green (ed.), Kluwers Publishing Company, 235-283.

Seal, C.V, Smith, C.R., Akin, O., Rockwell, D. 1995 "Quantitative Characteristics of a Laminar, Unsteady Necklace Vortex System in a Rectangular Block-Flat Plate Juncture," J. Fluid Mech., 286, 117-135.

Seal, C.V., Smith, C.R., Rockwell, D. 1995 "Dynamics of the Vorticity Distribution in End-wall Junctions,", Paper No. AIAA 95-2238, San Diego, Ca. Also AIAA Journal (in press).

Smith, C.R. 1996 "Coherent Flow Structures in Flat Wall Turbulent Boundary Layers: Facts, Mechanisms, and Speculation," Keynote paper in Coherent Flow Structures in Open Channels, P.J. Ashworth, S.J. Bennett, J.L. Best, and S.J. McLelland eds., John Wiley & Sons Ltd.

Smith, C.R. and Walker, J.D.A. 1997 "Sustaining Mechanisms of Turbulent Boundary Layers: The Role of Vortex Development and Interactions," in Self-Sustaining Mechanisms of Wall Tubulence, R.L. Panton, ed., Computational Mechanics Publications, Southampton, U.K. (to appear).

Seal, C.V. and Smith, C.R. 1997 "The Control of Turbulent End-Wall Boundary Layers Using Surface Suction," Paper No. AIAA 97-2060, Snowmass, CO, (in preparation).

Praisner, T.J., Seal, C.V., Takmaz, L., and Smith, C.R. 1997, "Spatial-Temporal Turbulent Flow-Field and Heat Transfer Behavior in End-Wall Junctions," International J. of Heat and Fluid Flow, Vol. 18, No. 1.

Seal, C.V. and Smith, C.R. 1997, "Intertwining Laminar Necklace Vortices," Physics of Fluids (Gallery of Fluid Motion), (in press).

Interactions/Transitions

a. Meetings

Seal, C.V. and Smith, C.R. "Quantitative Characteristics of a Laminar, Unsteady Necklace Vortex System at a Rectangular Block-Flat Plate Juncture," 47th Meeting of Amer. Phys. Soc., Atlanta, GA, 21 Nov., 1994.

Seal, C.V. and Smith, C.R. "Dynamics of the Vorticity Distribution in End-wall Junctions," Invited Talk, 26th AIAA Fluid Dynamics Conference, San Diego, Ca., 20 June 1995.

Smith, C.R. "Flow Structure and Heat Transfer in End-Wall Boundary Layers: A Study in Complex Vortex Dynamics," Invited Seminar, Department of Mechanical Engineering, École Polytechnique Fédérale de Lausanne, Lausanne, Switzerland, 20 Feb., 1995.

Smith, C.R. "Coherent Flow Structures in Smooth/Flat Bed Turbulent Boundary Layers," Keynote Address at Conference on Coherent Flow Structures in Open Channels: Origins, Scales, and Interactions with Sediment Transport and Bed Morphology, Leeds, England, 10 April 1995.

Smith, C.R. "Fluid Dynamics and Heat Transfer in End-Wall Boundary Layers," AFOSR Contractors Meeting, Wright Patterson AFB, Dayton, OH, 15 May 1995.

Smith, C.R. "Coherent Flow Structures in Turbulent Boundary Layers: Facts, Hypothesis, Speculation," Invited Seminar, NASA Langley Flow Physics Branch, Langley, VA., 17 July 1995.

Smith, C.R. "Spatial-Temporal Turbulent Flow-Field and Heat Transfer Behavior in End-Wall Junctions," Engineering Foundation Conference on Turbulent Heat Transfer, San Diego, CA, 24 March 1996

Seal, C.V. and Smith, C.R. "Spatially-Limited Suction as a Means to Control Turbulent Junction Flows," 49th Meeting of Amer. Phys. Soc., Syracuse, NY, 26 Nov. 1996.

b. Consultative/Advisory

Smith, C.R. Consultant, Flow Physics Branch, NASA Langley. 17-19 July 1995. Consultation on noise generation by vortices, and turbulent flow structure. Contact persons: Barry Lazos, Bart Singer, Tom Gatski

New Discoveries, Inventions or Patent Disclosures

None

Honors/Awards

Honor/Award: Keynote Speaker, Conference on Coherent Flow Structures in Open Channels
Honor/Award Recipient: C.R. Smith Year Received: 1995
Awarding Organization: British Sedimentological Research Group

Honor/Award: Selected first prize winner of the Gallery of Fluid Motion (Video) at the 49th Meeting of the American Physical Society (Division of Fluid Dynamics).
Honor/Award Recipient: C.V. Seal Year Received: 1996
Awarding Organization: American Physical Society

AASERT Evaluation Report

Parent Award

Award #: AFOSR - 91-0218

Award Duration: 1 Mar 91 to 14 Sep 93

Total Funding: $378,818

Graduate Students: Takmaz Levent (1 May 91 to 15 Jan 93)
Utham Sobrun (1 May 91 to 31 Dec 91)
Charles Seal (1 Jul 91 to 31 Aug 92)
John Fitzgerald (1 Jun 91 to 31 May 93)
Metin Demir (1 Sep 91 to 31 Aug 92)

AASERT Award

Award #: F49620-93-1-0346

Award Duration: 1 Jun 93 to 31 Mar 97

Total Funding: $120,000

Graduate Students: Charles V. Seal (1 Jun 93 to 15 Mar 97)

Certification

This is to certify that Charles V. Seal is an American citizen.

Ruth Tallman 5/29/97

Ruth L. Tallman, Program Administrator
Office of Research & Sponsored Programs

The Control of Junction Flows

by

Charles V. Seal III

Presented to the Graduate and Research Committee
of Lehigh University
in Candidacy for the Degree of
Doctor of Philosophy

In
Mechanical Engineering and Mechanics

Lehigh University

May, 1997

Approved and recommended for acceptance as a dissertation in partial fulfillment of the requirements for the degree of Doctor of Philosophy.

May 6, 1997
Date

Charles R. Smith
Dissertation Advisor

5/8/97
Accepted Date

Committee Members:

Charles R Smith
Dr. Charles R. Smith
Committee Chair

Donald O. Rockwell
Dr. Donald O. Rockwell

J DA Walker
Dr. J. D. A. Walker

Alparslan Oztekin
Dr. Alparslan Öztekin

R H Sorensen
Dr. Robert Sorensen

There's Only Us
There's Only This
Forget Regret
Or Life Is Yours To Miss
No Other Road
No Other Way
No Day But Today

- from RENT
by Jonathan Larson

Acknowledgments

Acknowledgments are always a difficult thing to write. I've spent a couple of days mulling over what to say, trying to think of an eloquent way to express my gratitude to all the special people who have helped me on this journey through life called graduate school, but I'm afraid I just can't seem to find the words to fully describe depth of gratitude and love I feel for these people. Well, anyway...here goes, just realize that the following expresses only a fraction of my feelings.

Evelitsa, my sincerest thanks go to you. Your love, friendship, and unquestioning support have helped me through many difficult times and your strength has been an inspiration. I can only hope that someday I can repay half your kindness. Don't let them break you, you're better than they are.

I've been blessed with good friends throughout my life, and my time at Lehigh has been no exception. Special thanks to Eric, Ellyse, and Jay whose friendship means the world to me. Without you guys this place would be hell. Kate, thank you for being a great listener and an even better friend. Jenn, I only hope to be half as hip as you someday. Jin, Jong-Woo, and Rhett, without your friendship and the workout sessions at the gym helped me decompress and stay sane (relatively ☺). A little over three years ago I told the Boilermakers I was staying at Lehigh until we won a championship. Well, we finally did win one, so now I can leave. Thanks guys.

Amanda, the special woman in my life, I thank you for your unjudging love. You can be demanding at times, but you were always there to turn a bad day around with a

playful swipe of the paw or a soft purr. TV was often a welcome escape from my work, so I also thank NBC for "must see TV", Fox for Melrose, the Simpsons and the X-files, and UPN for Babylon 5.

I want to thank my family for enabling me to pursue my dreams and goals. Thanks Mom. Thanks Dad. Thanks Andy and Beth. I love you all. I also want to thank my Aunt Judy and Uncle Lester, my Cousins Susan and Dan, and my Grandparents for their support and encouragement.

I wish to gratefully acknowledge the help and support of my co-workers and friends John Fitzgerald, Tom Praisner, and Dan Sabatino. Their assistance and comments have been invaluable in the preparation of this work. The assistance provided by Mr. Richard Towne, Mr. Robert Minnich, Mr. James Bunderla, and Mr. Tim Nixon of the Mechanical Engineering Machine Shop, was indispensable and is also greatly appreciated. Finally, I wish to thank Jo-Ann Casciano for her administrative assistance throughout my graduate career.

I thank my advisor Professor Charles R. Smith for his patience, guidance, recommendations, and insight. He has helped make my graduate experience at Lehigh a fulfilling professional and personal experience. I also want to thank Professor J. D. A. Walker and Professor Donald Rockwell, who provided insightful comments on the present work, their help is greatly appreciated. Also, valuable comments were given by Dr. M. Visbal at Wright-Patterson AFB.

Finally, I also wish to thank the Air Force Office of Scientific Research for its support of this research under grants F49620-93-1-0346 and F49620-93-1-0217. The continuing support of the AFOSR is gratefully acknowledged.

Table of Contents

List of Tables

List of Figures

Abstract

An experimental study of the effects of spatially-limited (i.e. localized) surface suction on unsteady laminar and turbulent junction flows was performed using hydrogen bubble flow visualization and Particle Image Velocimetry (PIV). Results indicate that, in general, suction on the *laminar* system can have four possible effects: 1) cause a segmentation of the necklace vortex system, where the initial system breaks into two or more separate vortex systems; 2) stimulate the formation of a "braid" system, wherein a complicated interaction between two adjacent necklace vortices arises adjacent to the sides of the cylinder; 3) modify the strength and periodicity of the original vortex system; 4) elimination of the advecting necklace vortex when it reaches the suction slot. Preliminary experiments, involving several passive control methods, including a fillet, control rings, and approach surface contouring, show that these methods can also be effective in modifying the behavior of the laminar vortex system.

Detailed analysis of laminar PIV results indicates that it is the impinging boundary layer instability which is the mechanism for frequency selection in the unsteady laminar case. Application of external perturbations to the impinging boundary layer can, therefore, be used to initiate "lock-on" (where the formation/breakaway frequency of the vortices is equal to the forcing frequency) for a narrow range of frequencies bracketing the natural, unperturbed frequency. In addition, application of a critical disturbance will cause transition of the flow to a turbulent-like behavior.

PIV results of a turbulent junction flow indicate that surface suction effectively weakens the instantaneous turbulent vortex and associated surface interactions on the symmetry plane, can both eliminate the *average* turbulent necklace vortex on the symmetry plane, and weaken the *average* downstream extensions of the vortex. It was also determined that suction effectively reduces the Reynolds-stress levels in both the symmetry plane, and the medial and trailing edge cross-stream planes. In addition, the unsteady motion of the turbulent vortex legs is reduced by application of suction.

1.0 INTRODUCTION

1.1 General

Juncture flows are complicated three-dimensional flows formed in the junction region of a bluff-body with a relatively flat surface. Practical examples of this type of flow include the flow in wing-body junctions on aircraft, turbine blade-hub junctions in turbomachinery, the junction of tall buildings with the ground, the cooling flow past computer chips on a circuit board, and the junctions of sensor and control surfaces with ship hulls. The generic characteristics of this flow are a boundary layer approaching a wall-mounted bluff-body. This type of flow may be categorized as either laminar or turbulent depending on the nature of the impinging boundary layer.

In the laminar case, the adverse pressure gradient generated by the presence of the bluff-body causes a local flow reversal of the approaching fluid. The reversed fluid moves upstream, decelerating until it stagnates with the approaching fluid at a line of attachment (Visbal, 1991; Coon and Tobak, 1995; Hung *et al.*, 1991; and Puhak *et al.*, 1995) (figure 1.1 (b)). At this point, instead of separating in a classical two-dimensional boundary layer fashion, the fluid attaches to the surface and flows laterally around the sides of the bluff-body (figure 1.1 (b)) due to of the cross-stream pressure gradient induced by the body. Downstream of the attachment line the boundary layer destabilizes, resulting in the formation of necklace (or horseshoe) vortices (figures 1.1, 3.1, and 3.9), which are U-shaped vortices oriented with the legs extending downstream around the sides of the body.

In the turbulent case, the approaching fluid undergoes a flow reversal similar to the laminar case; however, instead of developing a line of attachment, the reversed fluid and approaching fluid meet at a line of separation (Hung *et al.*, 1991). Downstream of this separation, the flow is characterized by the formation of a large-scale turbulent necklace (or horseshoe) vortex that varies temporally in size, position, and strength (figure 1.2).

The presence of these necklace vortices has a significant impact on the flow-dependent properties in the junction region, such as the local heat transfer rates and skin friction. For example, on a submarine, the formation of a necklace vortex system at various control surface junctions along the hull can increase the local skin friction (and hence drag) below the necklace vortices by inducing large local velocity gradients, $\partial u / \partial y$, as well as increasing noise due to the vorticity concentrations. In addition, the downstream extensions of the vortex legs can impinge upon and interfere with propeller or control surface operation (Lugt, 1983). At a turbine blade-hub junction, the necklace vortex system can greatly affect the local heat transfer rates (Praisner *et al.*, 1997), increasing thermal gradients and stresses. In addition, increased skin friction due to the presence of a necklace vortex system formed at a bridge pier-river bed junction results in increased erosion at the base of the support (Gupta, 1987).

Since these necklace/horseshoe vortex systems give rise to adverse hydrodynamic and thermal effects, it is desirable to investigate possible methods of necklace vortex system control. The control may take the form of *passive* methods, such as geometric modification of the bluff-body and/or wall (e.g. a fillet, figure 1.3), or *active* control

schemes such as surface suction or periodic perturbation of the flow. The objective for applying control may be the elimination of the vortex system, modification of the system behavior, modification of the strength of the system, or even enhancement (strengthening) of the vortex system, depending on the particular flow problem under consideration.

1.2 Related Works

1.2.1 *Passive Control of Junction Flows*

The study of the passive control of junction flows has received relatively little attention in the literature (only 7 publications relating to the control of junction flows were found and easily obtainable). The data that has been published, has focused primarily on the application of a fillet to the junction region to modify the turbulent necklace vortex system.

The effect of a leading-edge fillet on the *turbulent* flow in a wing-body junction was examined by Devenport *et al.* (1992), using oil flow visualization and pressure and velocity measurements. Figure 1.3 shows the geometry used in that study, consisting of an airfoil constructed with a 3:2 elliptical nose (major axis aligned with the chord), a NACA 0020 tail, and the associated fillet. The wing was mounted on a flat plate in a low-speed wind tunnel. Devenport *et al.* concluded that at 0° angle of attack the fillet eliminated the upstream separation of the boundary layer and hence formation of the turbulent vortex around the nose of the wing. However, they point out that elimination of the upstream separation does not imply the complete absence of the vortex. They go on to point out that downstream extensions of the vortex, formed from boundary layer

vorticity which has been skewed in its passage around the body, may still be present. However, their results gave no clear indications of such structures, so they conclude that either the vortex legs were either not present or too weak to be effectively visualized (the later numerical studies of Sung *et al.* (1988), described below, suggest that the turbulent vortex persists downstream even with a fillet). Velocity data of Devenport *et al.*, consisting of streamwise u and v-velocity traces obtained with LDV, was used to illustrate the effect of a fillet on the downstream flow; figure 1.3 presents some selected results, which indicate a reduction in the streamwise turbulence normal stress levels 3 chord lengths downstream of the wing leading edge (X/C=3). The effect of the fillet on the mean streamwise velocity at X/C=3 is also shown in figure 1.3, illustrating that the fillet reduces local distortion in the contours of mean streamwise velocity (u/U_∞) associated with the rotation of the necklace vortex (i.e. contours of constant streamwise velocity flatten out with the presence of a fillet). Thus, the authors conclude that a fillet reduces the nonuniformity of turbulence structure in the wake caused by the redistribution of streamwise momentum by the vortex. Devenport *et al.* also examined the effect of the fillet-wing at an angle of attack and determined that, apart from the expected asymmetry, little qualitative difference on the flow structure could be observed for both 6° and 12° angle of attack.

The effect of a fillet on a *laminar* junction flow was examined by Kubendran *et al.* (1988) using both smoke flow visualization, and velocity and pressure measurements. They used two linear leading edge fillets, 1" and 2" long (illustrated in figure 1.4), attached to a NACA 0012 airfoil of 6" chord mounted on a flat plate in a low-speed wind

tunnel. Based on visualizations, Kubendran *et al.* conclude that the addition of a fillet results in "considerable reduction in the juncture vortical flow" by eliminating the upstream attachment line (***Note***: the authors refer to this line as a separation line in their paper, whereas more recent studies [Visbal, 1991; Coon and Tobak, 1995; Hung et al., 1991; Puhak et al., 1995] have shown it to be a line of attachment). Figure 1.4 presents some selected results illustrating the effect of the fillets on smoke wire patterns generated at constant height. In addition, the width of the juncture wake region was shown to be reduced by the addition of the fillet (also illustrated in the figure 1.4 as a reduction in the width of the downstream area relatively clear of smoke). These same qualitative effects were observed by the authors at a 4° angle of attack.

A fillet of the same shape as that used by Kubendran *et al.* (1988) was studied numerically and experimentally by Sung *et al.* (1988) for two different airfoil shapes (NACA 0012 and NACA 0020) with a *turbulent* junction flow. The study focused on the effects of a fillet on the downstream flow in the junction region (called the wake region in their paper); effects similar to those described by Kubendran *et al.* were observed. The results indicate that a fillet effectively reduces the strength of a turbulent vortex, and therefore smoothes out nonuniformities in the wake velocity profiles, but does not eliminate the vortex entirely from the wake region.

Using a surface flow visualization technique employing particles of potassium permaganate sprinkled on the flat plate surface, Gupta (1987) examined the flow modifying effects of a passive control device located in front of a pier-flat plate junction. The nature of the impinging boundary layer was not explicitly described, but the flow

parameters cited (Re_W=2175, where W is the width of the pier, and U_∞=8.7 cm/s), suggest that the impinging boundary layer was laminar (however the boundary layer could have been tripped). The control device examined was an inverted delta wing (negative angle of attack) located in front of the bluff body, as shown in the figure 1.5. The limited nature of the visualization technique did not allow detailed observation of the flow, it did, however, reveal the formation of two streamwise vortices (one to either side of the body) on the underside of the device. These streamwise vortices extend downstream very close to the sides of the body with a rotational sense opposite to the necklace vortex. The surface visualizations also indicated a modification of the original necklace vortex structure. The precise nature of the change was not determined, but Gupta suggests that the device acts as a barrier to vortex formation upstream of the body, and that the leading edge vortices of the delta wing act to reduce the width of the necklace vortex wake by bringing in, closer to the pier, more energetic fluid from the outboard areas of the pier. Gupta also noted that the addition of the control device appeared to reduce the "violence" of the flow in the near wake region near the flat plate, apparently due to some modification of the interaction of the necklace vortex legs with the Karman vortices shed from the body; however no evidence of this modification was presented in the paper.

Another interesting passive control device, designed by Bandyopadhyay (1994) consists of an array (or honeycomb) of parallel passageways, of limited length, located in a streamwise orientation within the wake (i.e. downstream) region of the necklace vortex system. A description of this device was found only in a U.S. Patent (#5,303,82), so detailed results of its performance are not available; however Bandyopadhyay states that

"the suppressor provides many small corners to prevent forming of the single large vortex" downstream of the body leading edge. Figure 1.6 shows a schematic of the device with suggested dimensions and implementation.

A final passive approach to the control of junction flow has been "dilleting" of the wall at the root of the body (Bushnell & Donaldson, 1990). Dillets are the negative of fillets in that they entail the creation of a depression or dent in the wall adjacent to the base of the body. Bushnell reports that in recent tests "elimination of a major portion of the longitudinal vorticity associated with a thick airfoil mounted on a surface has been demonstrated."

1.2.2 *Active Control of Junction Flows*

Active control of junction flows has focused exclusively on the application of wall suction to the flow in the vicinity of the junction. Goldsmith (1961) applied distributed suction, via numerous thin cross-stream slots, to a relatively large area upstream of a wing body junction to delay boundary layer transition and maintain laminar flow in the junction region. In addition to suction along the wall, additional suction was applied along the length of the intersection of the airfoil and plate to reduce the corner boundary layer growth. Figure 1.7 (a) and (b), which show the experimental geometry as well as the results of the experiment, indicates that application of suction displaces the transition line significantly downstream. Figure 1.7 (c) shows the various nondimensional suction magnitudes (V/U_0, where V is the suction velocity and U_0 is the free-stream velocity) employed. While these experiments illustrate the usefulness of suction for maintenance

of laminar flow in a junction, no reference to the junction vortices or their change with suction was made in this paper.

More recently, Phillips *et al.* (1992) used mean velocity measurements obtained via a pitot probe to examine the effect of distributed surface suction upstream of a wing-shaped bluff body on the turbulent necklace vortex system. Suction was broadly applied through a porous wall 150mm wide by 190mm long, located just upstream of a bluff-body constructed from a 102mm diameter cylinder leading edge mated to a constant-width body of 140mm to give a total length of 900mm (see figure 1.8). Phillips *et al.* took velocity measurements in a cross-stream plane, 215mm downstream of the wing nose, for suction rates of Q^*=0,1.2,1.9, and 3.5; here, Q^* is the nondimensional suction volumetric flow rate Q_s/Q_{bl}, where Q_s is the volumetric suction rate through the entire surface and Q_{bl} is the volumetric flow through a control volume enclosing the impinging boundary layer over the width of the suction surface. Vorticity fields, calculated from the velocity data, are shown in figure 1.8. The results indicate a clear reduction in the strength of the vortex; in fact the figure suggests the total elimination of the junction vortex (at this particular streamwise location). Phillips *et al.* also calculated the nondimensional circulation over a rectangular area encompassing the vortex, observing a marked decrease in circulation strength with applied suction, also shown in figure 1.8. Note that for Q^*=2.0 and above, the nondimensional circulation remains constant at approximately 0.014. Phillips *et al.* hypothesize that this is a result of the streamwise vorticity generated at the outer edges of the suction surface, which acted as a source of streamwise vorticity and could not be eliminated.

1.3 Motivation and Objectives

As the summary of previous work (described above) illustrates, most research in the area of junction flow control has focused on the application of fillets or suction. While fillets have been proven to be effective in modification of the junction flow, to be effective, a fillet must be relatively large with respect to the characteristic dimension of the bluff body and thus increase the frictional losses of whatever device they are affixed to. These devices, by their nature, are also constantly "on"; that is they are always present in the flow field and cannot be used for intermittent control, should that be desired. In addition, they are difficult to manufacture and retrofit; thus, the addition of such devices to existing equipment can be relatively difficult and/or impractical.

Suction provides another approach, which has some advantages, and of course some disadvantages, compared to a fillet. First, suction can be selectively employed so that control is applied only when needed or desired. Second, manufacture of a suction surface is relatively straightforward, since it consists primarily of machining slots and/or holes in a surface. Suction has the added benefit that it can be actively modified to optimize performance as flow conditions change, which is not possible with a fillet. A disadvantage is that suction requires power to operate; however, numerous possible situations that could utilize the control of juncture flow (such as submarines and commercial aircraft) typically have power available for such an application.

The suction studies described above used constant rate suction applied over a relatively large spatial area upstream of the bluff body. Because of its relative simplicity of manufacture and implementation, the primary focus of the present study was the

application of spatially-limited suction applied via a straight slot to both a laminar and turbulent junction flow. The intent of this study is to illustrate that effective flow modification of a laminar and turbulent junction flow is possible using this simpler configuration.

To summarize, the general objectives of the present study are to examine the effects of several control methods on both a laminar and turbulent necklace vortex system, focusing primarily on the use of spatially-limited suction. Other schemes, examined in less detail, include: control rings, wall contouring, fillets, and applied perturbations. Specifically, this study seeks to document the effects of these control schemes on the topology, temporal behavior, and strength of the vortex systems. The specific objectives are to:

1) Characterize and describe the effects of spatially-limited, constant-rate surface suction (applied upstream of the body) on flow topology and behavior for both an unsteady laminar and turbulent necklace vortex system;
2) Quantify, in both the symmetry and downstream planes, the effect of spatially-limited surface suction on the strength, vorticity distribution, and turbulence quantities of a turbulent necklace vortex system;
3) Characterize and describe the effects of externally-applied perturbations on the behavior of a laminar necklace vortex system;
4) Examine the effectiveness of several passive control methods, including control rings, wall contouring, and fillets, on control of *laminar* junction flow in terms of a change in flow topology and behavior.

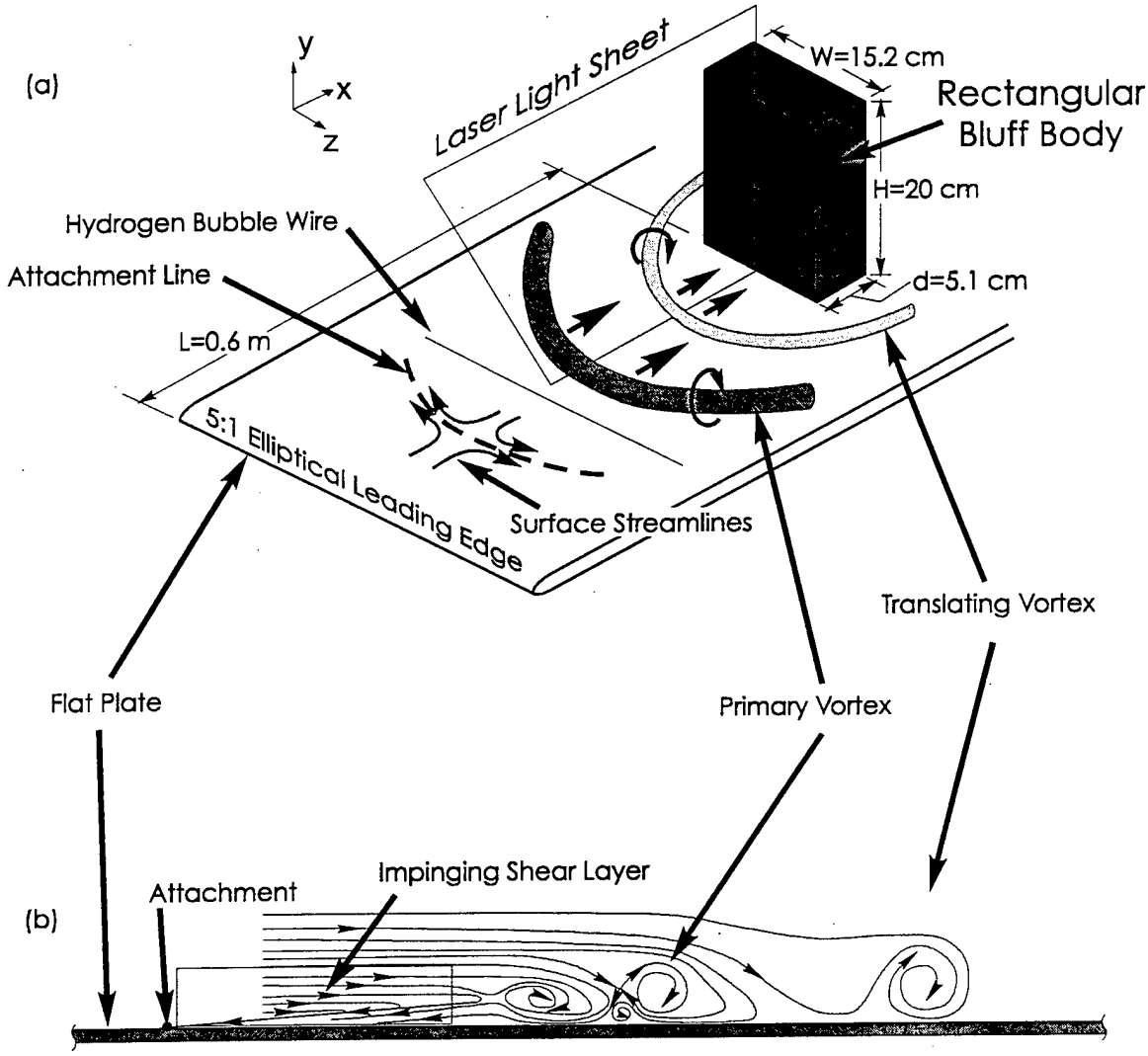

Figure 1.1 (a) Schematic of laminar necklace vortex system and experimental configuration for the laminar PIV study. (b) Symmetry plane schematic of the flow topology illustrating the attachment point and the resulting shear layer. Note that the details of the flow very near the block have been omitted. (after Visbal, 1991)

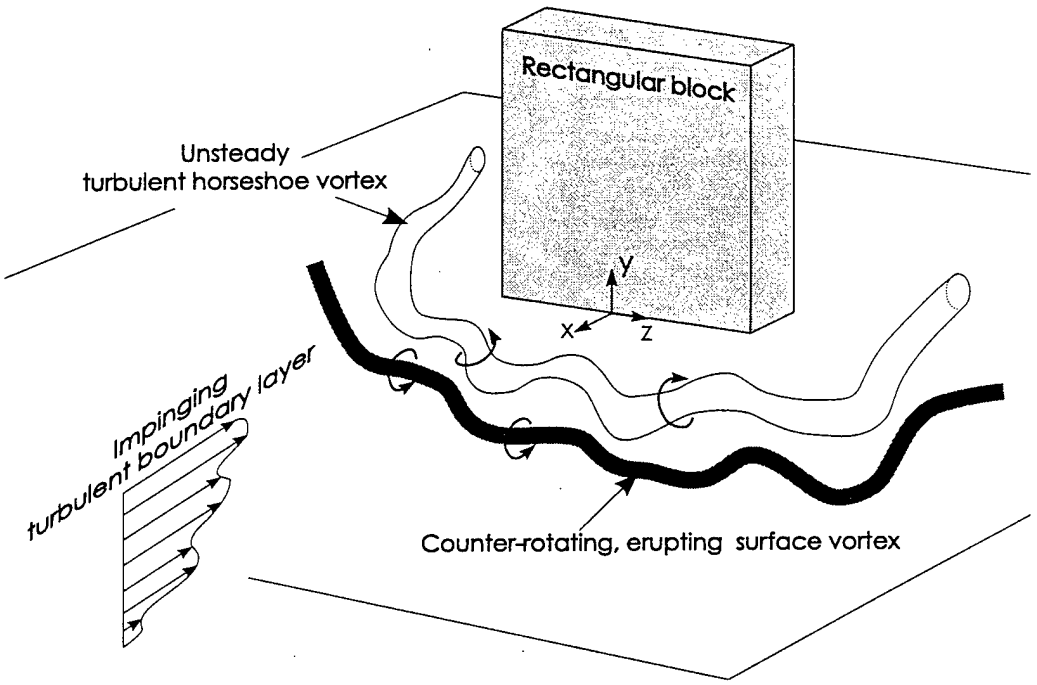

Figure 1.2 Schematic illustrating a turbulent necklace vortex system for a rectangular block.

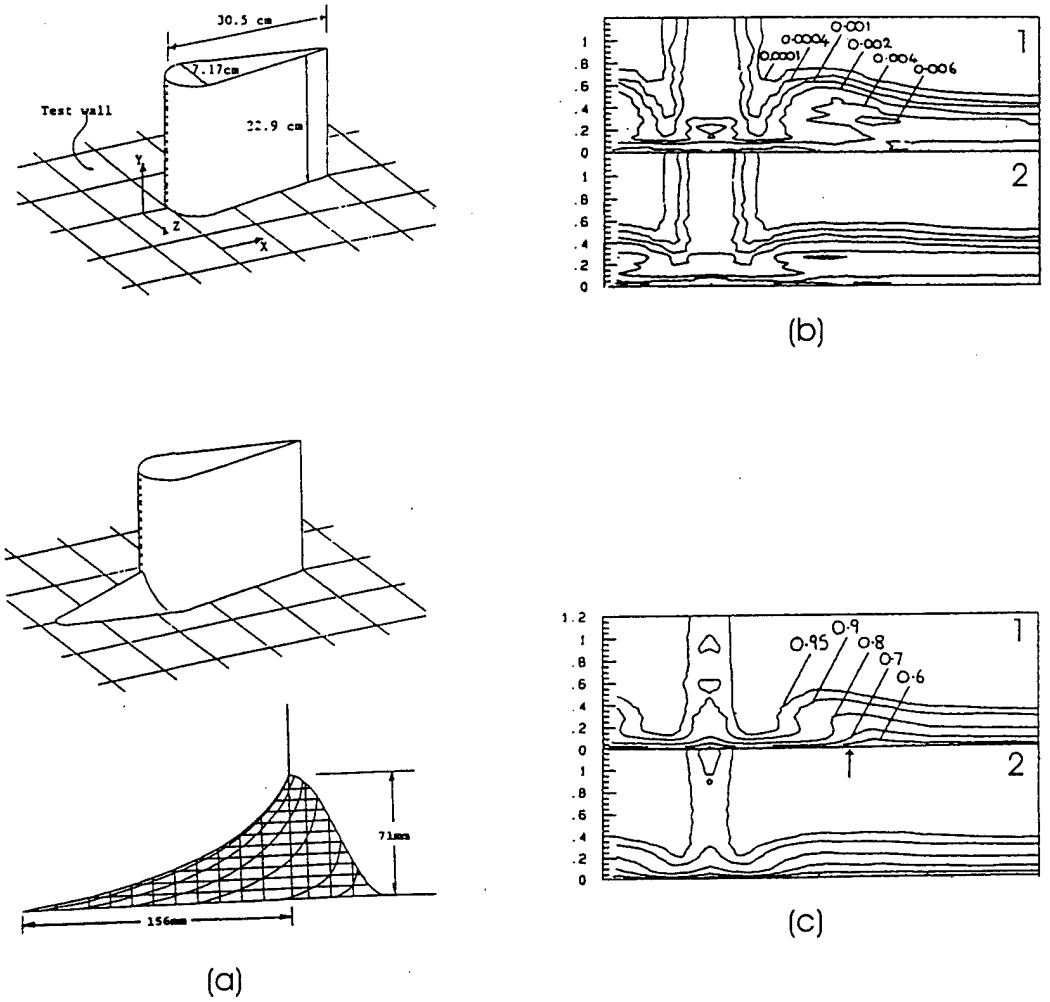

Figure 1.3 (a) Experimental schematics of Devenport *et al.* (1992) showing the baseline wing model and associated fillet. (b) Streamwise turbulence normal stress levels ($\overline{u'^2}/U_\infty$) for the baseline (no fillet case, top) and the filleted case (bottom) at x/C=3. (c) Mean streamwise velocity (u/U_∞) at x/C=3.

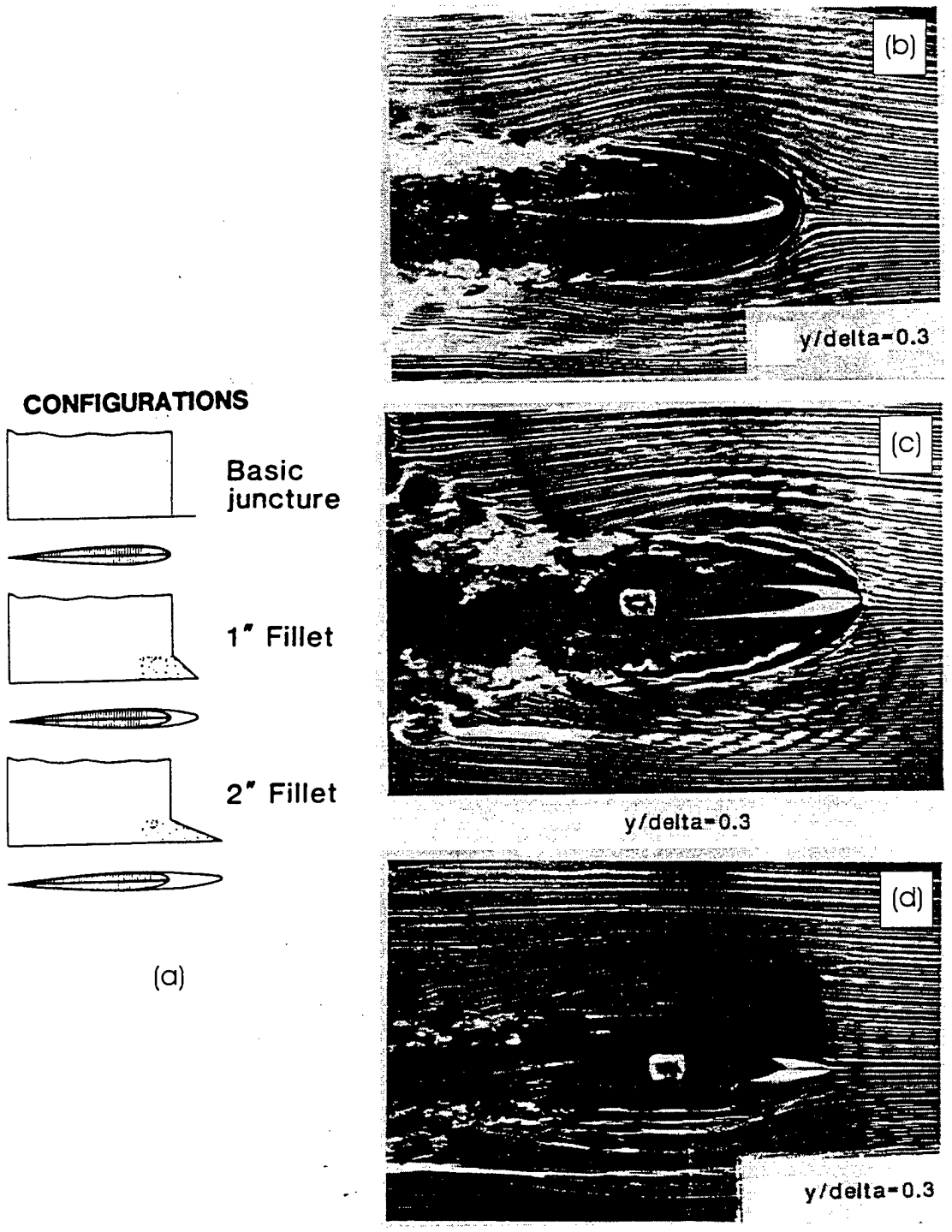

Figure 1.4 (a) Experimental schematics of Kubendran *et al.* (1988) showing the baseline wing model and associated fillets. (b)-(d) Smoke wire visualizations of the baseline wing, 1" fillet, and 2" fillet respectively at a wire height of $y/\delta=0.3$.

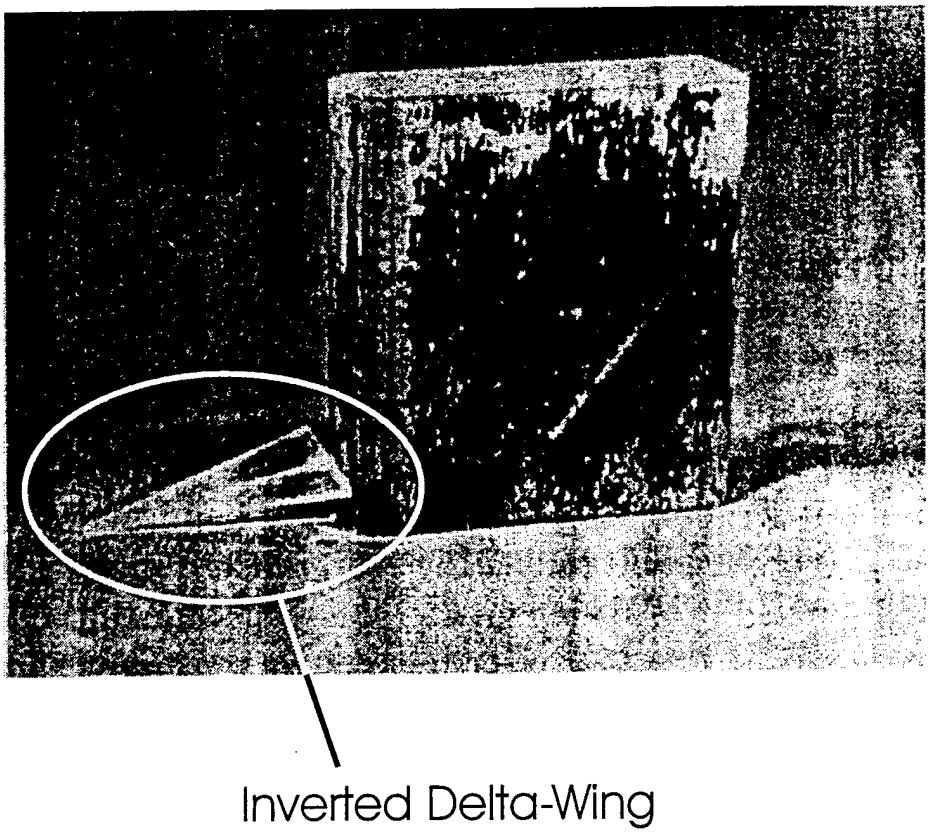

Figure 1.5 Photograph of the passive flow control device and bluff body used by Gupta (1987).

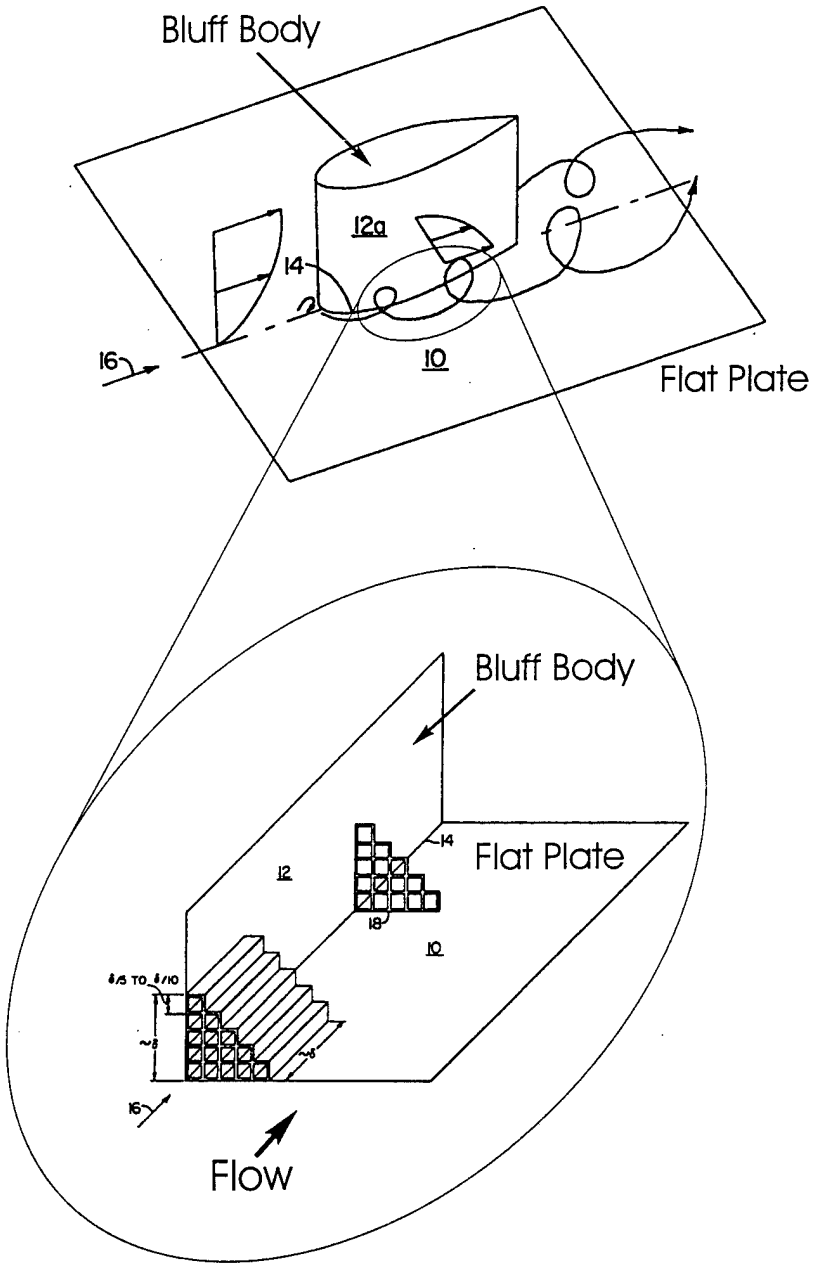

Figure 1.6 Patent drawings of the device designed by Bandyopadhyay (1994).

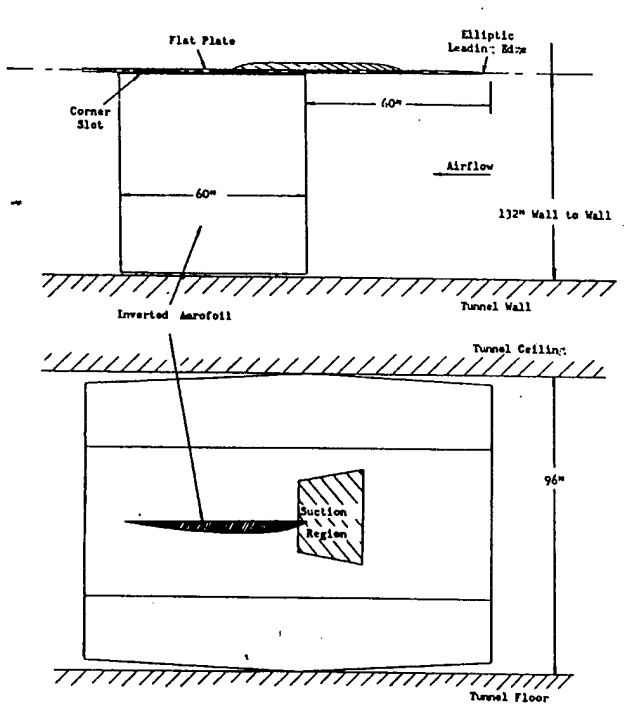

(a)

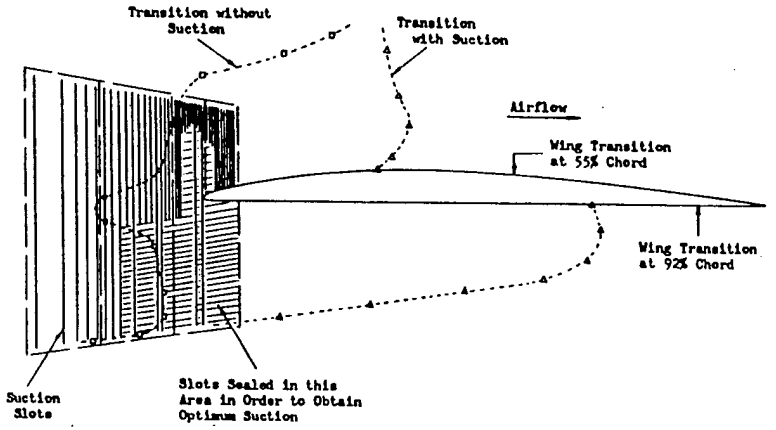

(b)

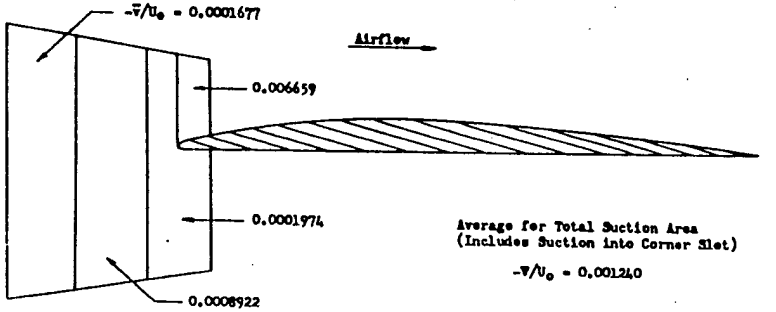

(c)

Figure 1.7 (a) Experimental schematic of Goldsmith (1961). (b) Schematic illustrating the various suction rates employed over the entire suction area. (c) Results indicating the effect of upstream suction on the location of boundary layer transition.

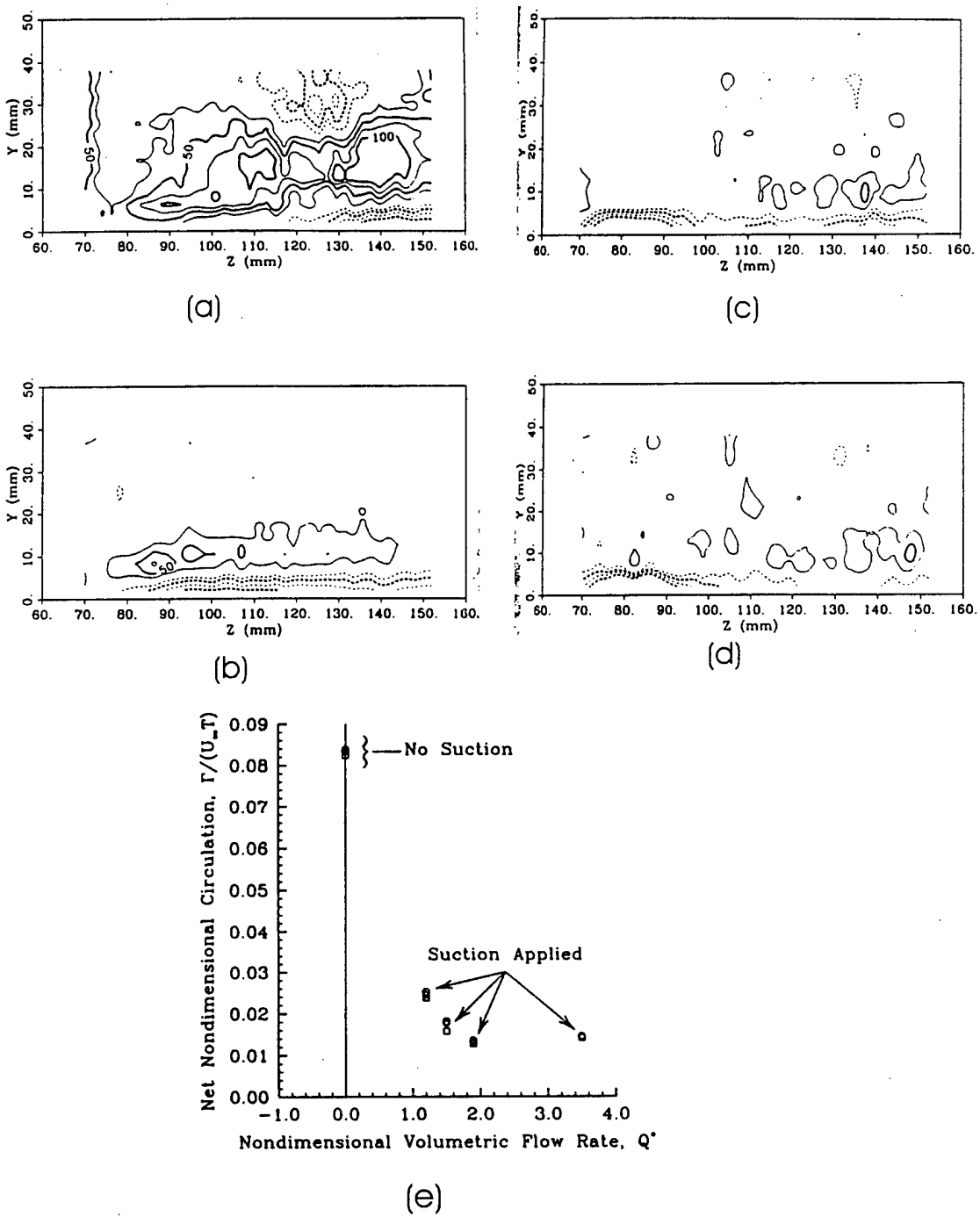

Figure 1.8 Selected results from the study of Phillips *et al.* (1992) (a)-(d) Contours of constant streamwise vorticity at a location 215mm downstream of the body leading edge for Q^{*}=0, 1.2, 1.9, and 3.5. (e) Plot of the nondimensional circulation strength calculated over a rectangular area encompassing the turbulent vortex leg vs. suction rate.

2.0 EXPERIMENTAL APPARATUS and METHOD

2.1 Water Channel

Experiments were performed in a Plexiglas free-surface water channel with a working test section 0.3m deep by 0.9m wide by 5.0m long located in the Lehigh University Fluid Dynamics Research Laboratory (figures 2.1 and 2.2). The Plexiglas construction allows for unrestricted viewing of the flow from both sides and the bottom, as well as from above. The water depth was maintained at 28.9cm for all experiments. The flow was driven by a Westinghouse variable-speed, feedback-controlled, 7.5 horsepower, DC motor connected to a split-casing centrifugal pump. The pump feeds water into the inlet tank via a distribution manifold, which then passes through a fiberglass honeycomb flow straightener (7.5cm thick, 0.8cm cell) to establish uniform flow, followed by two 20-mesh, stainless steel, turbulence control screens. A 2:1 inlet contraction is used to reduce any remaining flow irregularities prior to the working section. The flow then passes through the working section to an outlet tank, and is recirculated.

At a water depth of 28.9cm the channel provides a stable flow from 0.01 m/s to 0.4 m/s, with free-stream turbulence intensities near the beginning of the test section less than 0.2 percent at a flow velocity of 0.12 m/s (Greco, 1990).

A traversing platform mounted above the working section of the water channel was used in the present study for probe support and location. The platform rides on two

4.1m long cylindrical steel rails mounted on top of each side of the channel frame. The platform is driven by a 1.0-horsepower Reliance Electric motor capable of generating platform speeds of 0.01 m/s to 0.24 m/s in either direction. In the present study, the platform was only used for probe support. Hydrogen bubble probes were mounted on a mechanism capable of positioning the probe in three directions, which in turn was mounted on the traversing platform, allowing the probe to be located anywhere in the flow field.

2.2 Test Apparatus

2.2.1 *Plate and Cylinders*

A 1.8m long (1.9cm thick) Plexiglas flat plate with a 5:1 elliptical leading edge was used to establish a laminar boundary layer for the present studies (figures 2.2 and 2.3). When a turbulent boundary layer was required the flow was "tripped" using a threaded rod located approximately 2-3cm from the leading edge of the plate. The plate is elevated approximately 10cm above the channel floor by two streamwise support legs, providing a water depth of 17cm above the plate. Three circular cut-outs were machined in the plate to accept interchangeable suction slot plugs at three streamwise locations (45, 90, and 120cm from the leading edge). For the present study only the 90cm location was utilized. Blank inserts were used to fill the remaining two cut-outs.

The plate was designed to minimize flow blockage underneath the plate (Haidari 1990), thus reducing the pressure difference between the upper and lower flow. This was done by recessing the suction line tubing (lengths of 5.5mm i.d. brass tubing) leading to

the suction slots in the plate. In addition, the legs were located 3cm from the outside edges of the test plate. To further reduce blockage, the support legs were given a 5:1 elliptical leading edge. A 9° taper at the trailing edge was used to eliminate vortex shedding, and local flow unsteadiness. Each of the support legs contained three leveling screws, allowing the plate to be leveled.

A junction geometry was created by placing cylinders directly on the flat plate (figure 2.4). The length of the cylinders was such that they extend beyond the edge of the boundary layer, well into the free-stream. The majority of experiments were performed using an 8.8cm diameter cylinder; however, 4.4cm and 5.1cm diameter cylinders were used for some other limited studies. To maintain symmetry, the cylinders were located on the centerline of the plate, in line with the suction slot inserts.

Several slot locations relative to the leading edge of the cylinder were examined by varying the streamwise location of the cylinder. For the laminar study (§3.3.1), slot locations included 150mm, 88.5mm , 38.5mm, and 10mm upstream of the cylinder (figure 2.5). The terminology used to describe these slot locations was developed according to the position of the slot relative to the regions identified for a laminar, unsteady necklace vortex system in the breakaway regime (Seal, 1993). The terminology used was respectively: "formation+" (the slot is located upstream of *both* the attachment line and the region where the necklace vortices form); "formation" (the slot is located in the region of vortex formation); "translation" (the slot is located downstream of the formation region, wherein the vortices are advecting downstream); and "corner" (the slot

is located immediately adjacent to the cylinder). For the turbulent study (§4.2), the cylinder leading edge was located 22mm downstream of the slot.

The variation of the cylinder location in the streamwise direction, of course, had the effect of changing the baseline, no control flow. For example, for a laminar, unsteady necklace vortex system in the breakaway regime (at U_∞=constant at 8.4 cm/s) this results in a *maximum* decrease in breakaway frequency of 38% (.34 Hz to .47 Hz) from the most upstream location of the cylinder to the most downstream location. The separation line in front of the cylinder was observed to *increase* from 123mm upstream of the cylinder at the most upstream cylinder location to 133mm upstream of the cylinder at the most downstream cylinder location (figure 2.5). There would also be an associated change in strength of the vortices, but ***the general character of the flow remains unchanged*** with cylinder position for both the laminar and turbulent cases. So, effective comparison of the effect of slot location can be carried out by referencing the effect of control at any given slot location to the baseline no-suction case with that same slot location.

The cylinder was constructed of Plexiglas with carefully machined end surfaces to eliminate leakage between the cylinder and the plate. The Plexiglas construction also allowed a laser sheet to be located on the symmetry plane for visualization and PIV measurements (figure 2.4). To direct a laser sheet along the symmetry plane, an angled mirror was placed inside the cylinder, minimizing the distance the laser beam had to travel through the water, thus maximizing illumination. In addition, this configuration eliminated the possibility of mirror interference with the downstream flow (the mirror was located behind the cylinder for certain slot locations because the suction slot

apparatus interfered with the passage of the laser sheet cleanly through the bottom of the plate). End-view visualizations were performed by rotating the laser sheet to a cross-stream orientation and passing it through the bottom of the flat plate (figure 2.4). The coordinate system for this study was defined as shown in figure 2.4.

2.2.2 *Suction Slot and Apparatus*

Initially both a 1.25cm x 2mm and a 6.4cm x 2mm rectangular slot placed in a cross-stream orientation were examined (figure 2.6). Initial tests indicated that while both slots affected the symmetry plane flow, the larger of the slots held the most promise in terms of affecting the downstream extensions of the vortices. Therefore, the larger of the two slots (6.4cm x 2mm) was used for this study. This 6.4cm x 2mm slot was employed in a previous study (Haidari, 1990), where it was used for uniform injection (to generate hairpin vortices); it proved equally appropriate for the present study.

The plug consists of three separate sections. The slotted section is constructed of 0.9cm thick Plexiglas, 7.7cm in diameter. The slot itself has a base length of 3.75cm and expands to the full length of 6.4cm at the surface (figure 2.6). A hollow cylindrical section (2.4cm long and 3.75cm i.d.) is glued to the bottom of the slotted piece to form a reservoir. The inside wall of the reservoir is bored out 0.5cm below the slot, creating a step change in the inside diameter. A 15 pore/cm filter material (1cm thick) was placed against the step change to add resistance, thus distributing the suction flow rate uniformly across the slot. The plug is capped with a thin Plexiglas plate, which is connected to the suction lines via a small length of brass tube (5.5mm i.d.).

As shown in figure 2.7, Tygon tubing (6.5mm i.d.) connected the brass tube to the base of a "T" junction. Each of the upper two outlets of the "T" was connected to an Omega variable-area rotameter mounted outside the channel, below the water level. Each rotameter contained a control valve for flow rate control; one rotameter had a maximum flow rate of 1666 cc/min (Omega cat. no. FL-1347-C), and the other had a maximum flow rate of 333 cc/min (Omega cat. no. FL-1345-S). These two flow meters combined to allow precise control of the suction through the slot. The outlets of the flowmeters exhausted via Tygon tubing to a drain. The hydrostatic pressure difference provided the driving force for the suction system. When all components were assembled suction rates from 0-633 cc/min were obtainable.

In addition to the straight slots described above, a larger curved slot was constructed after testing of the straight slots was completed. Figure 2.8 is a scale plan-view drawing of the slot showing its shape, which was determined by matching the curvature of the laminar necklace vortices in the formation region for a 8.8cm diameter cylinder with leading edge located 85.6cm from the plate leading edge. The slot was 2mm wide and machined in a 40.64cm diameter Plexiglas plate, which was inserted in the flat plate. The profile of the slot, shown in figure 2.8, consists of a 2mm wide straight section which expands to 12mm at the bottom of the insert. A curved reservoir was located below the slot with thirteen 6mm diameter holes located at equidistant points along the length of the cap. Brass tubing was inserted into the holes to enable the connection of the suction lines (5.5mm i.d. Tygon tubing). A 15 pore/cm filter material was placed in the reservoir to add flow resistance and smooth out velocity variations

along the length of the slot. For this study, only 6 of the holes (see figure 2.8) were utilized; the remaining holes were plugged. The suction lines were connected as shown in the figure, with two adjacent suction lines "teed" to one line. The three resulting lines were connected to a relatively large collection tank constructed of a 16.5cm (i.d.) diameter pipe, 17.5cm long, capped at both ends. At one end 6mm diameter holes were drilled to accept the suction lines; the other end was connected to a 2.38cm (i.d.) outlet pipe. A valve on the outlet pipe allowed for suction rate control. This particular configuration allowed suction rates of up to 49.88 ml/s or suction velocities of 5.33 cm/s.

2.2.3 *Rings and Geometric Modifications*

A passive control method, in the form of "control rings" was also examined briefly. The rings, which are circular fins attached to the cylinder, were fashioned from 0.8mm thick brass sheets and could be mounted on the cylinder at various heights (h) from the flat plate (figure 2.9). Four rings, all with an inside diameter of 8.8cm, were constructed, with respective flange widths (w) of 4, 3, 2, and 1cm. Notches were cut in the rings and angle brackets mounted to the rings, with a screw connecting the brackets, so that they could be securely mounted on the cylinder (detail figure 2.9). The rings were rotated so that the clamping mechanism was on the downstream side of the cylinder.

For some limited studies, an oil based clay was used to modify the geometry of the cylinder and the plate (figure 2.10). Oil based clays have the benefit of not dissolving in water. Roma Plastlina No. 2 (purchased from a local art supply store) was used since it remained firm in water and was easily moldable. This clay was used to mold a fillet for

use with the 8.8cm diameter cylinder of the same geometric shape as that employed by Devenport *et al.* (1992) (see figure 1.3(a)). The height of the clay fillet employed in the present study was 60mm (~0.67D) at the cylinder and extended 170mm (~1.9D) upstream. In addition, the clay was used to fashion an insert for the plate in which a curved depression could molded. Two depressions (with semicircular profile shapes) were examined, each approximately semicircular in shape (radius~30mm), with a depth of approximately 2 and 4mm.

2.2.4 *Periodic Suction Control System*

In addition to the constant rate suction system described above, a system was devised to allow examination of periodic surface disturbances, or pulsations, as a means of control. This was accomplished by attaching the suction slot, via the brass and Tygon tubing, to a syringe driven by a linear actuator, which provided sinusoidal motion to the plunger (figure 2.11). The linear actuator was comprised of a computer-controlled C-series driver/indexer stepper motor (Compumotor) driving a lead-screw assembly connected to the syringe plunger. The syringe was a calibrated 10ml Fisher brand variable-volume varipet.

The periodic suction system allowed the generation of a periodic surface injection/suction cycle. The period and amplitude of the surface pulsations could be modified by varying the stepping motor speed, acceleration, and angular rotation, which allows a broad range of perturbation frequencies and amplitudes to be achieved. The computer control generated sinusoidal variations of the plunger, generating sinusoidally

varying slot velocities. This behavior was confirmed using a LVDT connected to the linear actuator. Labview© software was used to record and store the output from an A/D board connected to the LVDT. Calibration of the system was performed by visually determining the maximum volume displaced during a cycle from the calibrated Syringe at a fixed motor setting. Figure 2.12 shows several surface velocity plots covering the range of motor settings used in the present study. The solid lines represent actual surface velocity determined using the LVDT readings; The dashed lines are fitted sine functions, which illustrate the adherence to sinusoidal variations in suction velocity.

2.3 Flow Visualization

Extensive flow visualization was performed using a moveable hydrogen bubble visualization probe consisting of either a 25 or 50μm diameter platinum wire soldered taut between two insulated brass rods forming a Y-shaped support. The wire is used as the cathode in a process of electrolysis, with a variable voltage/frequency power supply providing a pulsed current density to the wire; the anode was a 6.0mm diameter carbon rod located away from the region of interest (figure 2.13). The result is the generation of fine hydrogen bubbles which visualize the flow structure. Sodium sulfate (Na_2SO_4) is added in a concentration of approximately 0.15 g/L to increase the conductivity of the water, thus improving bubble quality and reducing the voltage required to achieve the electrolytic process. The probe was used in a cross-stream orientation to generate bubble sheets parallel to the flat plate surface; the wire location was varied according to how the flow was to be marked (figure 2.13).

Lighting consisted of either (1) general illumination through the bottom or from side of the flow channel using a 1050W photographic lamp, or (2) light sheet illumination created using a 7-watt scanned argon-ion laser (Rockwell et al., 1993). The light sheet was oriented either on the symmetry plane or downstream of the body in a cross-stream plane (as illustrated in figure 2.4).

In addition, qualitative visualization of the flow was performed by seeding the channel with PIV particles (described below), illuminating the flow with a laser sheet, and using standard video (described below) to record the flow. The video shutter speed was kept at 1/60sec and the laser was scanned at >500Hz so that each video image reflected multiple particle streaks. Figure 2.14 shows a short time sequence of this type of visualization technique (for a turbulent necklace vortex interacting with a surface). This method has the benefit of providing instantaneous, whole-field streak patterns, but only in a 2-D plane. Hydrogen bubble visualization can provide limited 3-D flow information (e.g. figures 3.13-3.19), but hydrogen bubbles depend on the location of the bubble wire, which limits the region of the flow field visualized. In general, these two methods of visualization are used together in a complementary fashion.

2.4 Video System

The flow visualization experiments were recorded in real time using a SONY SSC-S20 CCD color video camera connected to a PANASONIC AG-7300 SVHS video cassette recorder recording at 60 interlaced frames per second (figure 2.15). The camera was fitted with an 18-108mm zoom lens enabling detailed observation of small-scale

structures on the order of millimeters in the flow. At the highest zoom setting a field of view 2.9cm x 2.2cm could be viewed. A SONY PVM-1943MD color video monitor was used to view the experiments as they were performed and recorded, and for later analysis of the recorded sequences.

The recorder is capable of playing the video either forwards or backwards, in slow motion or freezing a selected frame. A single-frame advance mode was also used to allow detailed analysis of the experiments. Single images from a video sequence could be digitized into a TIFF file format via a DATA TRANSLATION video frame grabber board.

In selected instances, simultaneous, 2-camera, dual-view hydrogen bubble visualizations were performed. Here two cameras were used simultaneously, one viewing an oblique view and another viewing an end view through the use of a 45° mirror (figure 2.15). A JVC video effects generator was used to combine the two video signals in a split-screen view. For these visualizations, general illumination was used for the oblique views and a cross-stream laser sheet was used to illuminate the bubble sheet for end views.

2.5 Particle Image Velocimetry (PIV)

High image-density particle image velocimetry (Adrian, 1991; Rockwell *et al.*, 1993) was used to investigate the velocity field on the symmetry plane of the laminar flow formed in a flat plate-rectangular block junction. In order to obtain sufficient spatial resolution, it was necessary to magnify the flow field, thus allowing a view of only a part

of the vortex system at one time. Therefore, two sets of data were obtained with slightly overlapping fields-of-view in order to establish collective data covering the whole vortex system (figure 2.16 (a)). The first set of experiments (Seal *et al.*, 1995) covered the translation/amalgamation region (84mm x 24mm) in which the vortices enter the field-of-view from the left, advect downstream, and amalgamate with a sustained corner vortex (see §3.2). The second set of experiments focused on the upstream formation region, to examine how the impinging boundary layer vorticity is organized into the necklace vortices. Figure 2.16 (a) shows the physical orientation of the two fields-of-view. Note that both fields of view are located downstream of the boundary layer attachment (figures 3.4 and 3.6). Data was taken at 1.0 second intervals in the translation/amalgamation region and at 0.5 second intervals in the formation region; phase-resolution of the two fields-of-view was done in post processing. In addition, a second set of data of even higher magnification was obtained for the formation region to provide finer spatial resolution.

High image-density particle image velocimetry (Adrian, 1991; Rockwell *et al.*, 1993), was also used to establish the details of the velocity field for one particular case in the turbulent regime, with an 8.8cm diameter cylinder mounted 92.3cm from the leading edge of the plate (22.3mm downstream of the suction slot, figure 2.5). The free stream velocity was set at 12.4 cm/s, which gave corresponding $Re_L=1.13x10^5$, $Re_D=1.09x10^4$ and $Re_{\delta^*}=429$, based on (1) the distance L from the leading edge to the cylinder, (2) the cylinder diameter D, and (3) the displacement thickness δ^* calculated for an equivalent unobstructed turbulent boundary layer at the cylinder location L=92.3cm. Constant rate

surface suction was applied at three different rates, $V_{suction}/U_{\infty}$=0, 0.29, and 0.68, where $V_{suction}$ is the average suction velocity computed by dividing the metered flow rate by the slot area.

The scanned laser was used to illuminate spherical, metallic-coated particles (nominal diameter of 12μm and density of 2.6 g/cm3) on the symmetry and end-view planes (figures 2.4 and 2.16 (b)). The end view planes are named according to their downstream location relative to the cylinder (i.e. medial, trailing edge, or 1 radius downstream end view). Approximately 20cm^3 of particles were mixed in the 2400 gallon water channel, which assured approximately 15 particle images within each interrogation window (1.25x1.25mm in the plane of the laser sheet on the symmetry plane, and 2.3x2.3, 2.21x2.21, and 2.14x2.14mm for medial, trailing edge, and 1 radius downstream end view locations respectively [figure 2.16 (b)]; see below). The scanned laser sheet was generated using a 72 facet rotating mirror in conjunction with a 7 watt Argon-Ion laser. The rotating mirror was mounted on a moveable platform that could be rotated so that the streamwise position and orientation of the laser sheet could be adjusted. An optical assembly employing a convex lens, concave lens, and a singlet lens (Corcoran, 1992) was used to focus the beam to a diameter of approximately 1.0mm in the region of interest (figure 2.17). A combination of a 500 Hz laser scanning rate and a 1/125 second camera exposure time was employed, which produced image photographs with 4 exposures of each particle within the viewing field. Depending on required time resolution, photographs were taken either 2 images/sec or 5 images/sec, capturing approximately 17.5 seconds or 7 seconds of data respectively on 35mm film. A NIKON

F4 35mm camera (using Kodak TMAX 400 film) was used to record the particle images (figure 2.18).

A rotating bias mirror, located immediately in front of the camera lens at an angle of 45° to the lens centerline (figure 2.18), was used to impart a uniform bias velocity to all particles during photographic recording in order to remove the directional ambiguity associated with regions of reverse (negative) flow, and decrease the dynamic range of the image patterns. The magnitude of the imposed bias was sufficiently large to overcome negative velocities associated with regions of reverse flow, but small enough such that the principal features of the actual velocity field were not obscured. The principal guidelines for determining the minimum bias velocity (Towfighi, 1992) is that a line passing through successive, multiply-exposed particle images should not turn through an angle of greater than 90°. In order to recover the actual velocity field, the uniform bias velocity was subtracted from the field of vectors obtained after evaluation of the entire image.

To evaluate the entire pattern of particle images recorded on 35mm film, a given pattern is digitized into a TIFF file format, using a Nikon LS-1000 35mm film scanner in conjunction with a PC housing one Eighteen-Eight array processor. The resolution of the digitized pattern of images was 106 pixels/mm of film. The velocity at a given location was determined from the digitized image using a single-frame autocorrelation technique involving application of two successive FFTs over an interrogation window of 80 x 80 pixels and 90 x 90 pixels in the symmetry plane and end views respectively for the turbulent case and 80 x 80 pixels for all three laminar cases. This window was sequentially scanned across and down the image (starting from the upper right corner) in

order to establish the velocity at successive locations over the entire field. In order to approximate the Nyquist sampling criterion, adjacent windows were overlapped by either 40% or 50%. For the turbulent case, this evaluation process yielded 2,312 vectors in the medial end-view case, 2,730 vectors in the trailing edge and 1 radius downstream end-view cases, and 4,042 velocity vectors on the symmetry plane. For the laminar cases, approximately 4,950 vectors were obtained. Since the magnification $M=L_f/L_a$ of the camera lens was 0.61 for the turbulent symmetry plane case, the effective width of the interrogation window in the plane of the laser sheet was $d_I/M=1.25$mm; correspondingly, the effective grid width was $\Delta l/M=0.62$mm in the laser sheet (i.e. the physical plane). The values of M, d_I/M, and $\Delta l/M$ for the turbulent end views and laminar cases are summarized in table A.1 in the Appendix.

In order to accommodate the solid boundaries of the flat plate and cylinder in the field of view, each TIFF image was cropped to a size such that the lowest row and rightmost column (in images where the cylinder was present) of vectors would fall on the solid boundaries. In this manner the no-slip condition could be ensured by setting the velocity to zero at these grid locations (on the symmetry plane the grid locations corresponding to the slot location were treated as usual). Note that due to the image shifting, the location of the cylinder was somewhat ambiguous because the image of the cylinder edge appeared as four vertical lines separated by the bias amplitude. As an approximation, the location of the cylinder was approximated as the middle of the cylinder images.

The interrogation process was not successful at all locations. Due to a variety of factors, including locally-inadequate quality of the particle images or insufficient particle concentration, the evaluation process can lead to an incorrect vector or no vector at all. In cases where the vector differed drastically from its neighbors, it was manually deleted. Each blank interrogation area was then replaced by a vector determined by bilinear interpolation (after application of the no-slip condition described above). Typically, not more than two to three percent of the vectors in the entire velocity field had to be determined using this interpolation process.

Prior to further processing, the entire field of velocity vectors was smoothed by convolving the field of vectors with a Gaussian kernel having a coefficient p=1.3, which minimizes distortion of the original field of vectors (Landreth and Adrian, 1989). No further filtering or smoothing was done in constructing the contours of constant vorticity (or any other derived quantity, such as Reynolds-stress); these contours were determined using either Spyglass Transform© or Tecplot© software. For certain plots, the levels between vorticity contours were interpolated to emphasize the structural features of the flow. The typical minimum distance between contours was approximately 1/2 of the grid width $\Delta l/M$; in a few high gradient regions it decreased to as low as 1/6 $\Delta l/M$. In addition to vorticity and Reynolds-stress contours, streamlines were obtained from the PIV data using Tecplot© software, which uses a predictor-corrector integration algorithm for calculating streamtraces, where the integration step size was allowed to vary from 25% to 2.5% of the grid size.

2.6 Flow Visualization and Experimental Techniques

Flow visualization was used to both characterize the flow behavior and determine the frequency behavior of a laminar necklace vortex system in the breakaway regime in response to several types of control. The methods of control examined via flow visualization were constant rate surface suction and surface perturbations applied through the suction slot, as well as limited smaller-scale studies of the control rings, a fillet, and contouring of the flat plate.

For the constant rate surface suction study, systematic flow visualization was done for four different slot locations relative to the cylinder (10mm, 38.5mm, 88.5mm, and 150mm from the cylinder, figure 2.5). For each slot location, the nondimensional suction velocity $V_{suction}/U_\infty$ was varied systematically from a zero to a maximum of 0.68. The free-stream velocity U_∞ was held constant at 8.26 cm/s for all cases. At each slot location and suction velocity, a video sequence of the flow (both hydrogen bubble and particle visualization) was recorded for later characterization of the flow behavior. The video was analyzed to establish the flow behavior and the frequency of events in the cases where the system behaved periodically. The frequency of periodic events was established from the recorded sequences by measuring, with a stopwatch, the time for passage of a given number of repetitive flow structures using a fixed reference point on the monitor. An uncertainty analysis (Kline and McClintock, 1953) of this technique shows a worst case uncertainty of approximately ±1.0%.

For the surface perturbation studies, a variety of perturbation frequencies and amplitudes were employed. The amplitude of the surface velocity fluctuation was computed via the formula

$$V_{perurbation} = \frac{2Sf}{A},$$

where S is the volume of fluid displaced during one stroke of the perturbation syringe, f is the frequency of plunger oscillation, and A is the area of the slot (note that this velocity represents an *average* surface velocity over one half of a cycle). Frequencies ranged from 0.14 Hz to 2.37 Hz; velocity amplitudes ranged from .028 cm/s to 2.409 cm/s. Table A.2 (Appendix) lists all amplitudes and frequencies examined. The application of the perturbations described above was carried out at a series of slot locations (21.7cm, 29.4cm, 12.9cm, 7.8cm, and 5.3cm upstream of the 8.8cm diameter cylinder) for one free-stream velocity (U_∞=8.26 cm/s).

For the more limited studies of the rings, fillet, and plate contouring, the range of parameter values examined was significantly less than those described above. To examine the effect of flat plate contouring, a smaller cylinder (4.7cm dia.) was placed on the clay insert approximately 92cm from the leading edge of the plate. The effect of the contouring was assessed for a laminar approach flow, with the free-stream velocity maintained at 12.7 cm/s. Only two sizes of the curved depression were examined. For the control rings, a single ring location of 12mm off the plate (h=12mm) was examined with the cylinder located 92.3cm from the leading edge of the plate and the free stream velocity at 9.1 cm/s. For the fillet experiments, a single free-stream velocity and cylinder location was examined.

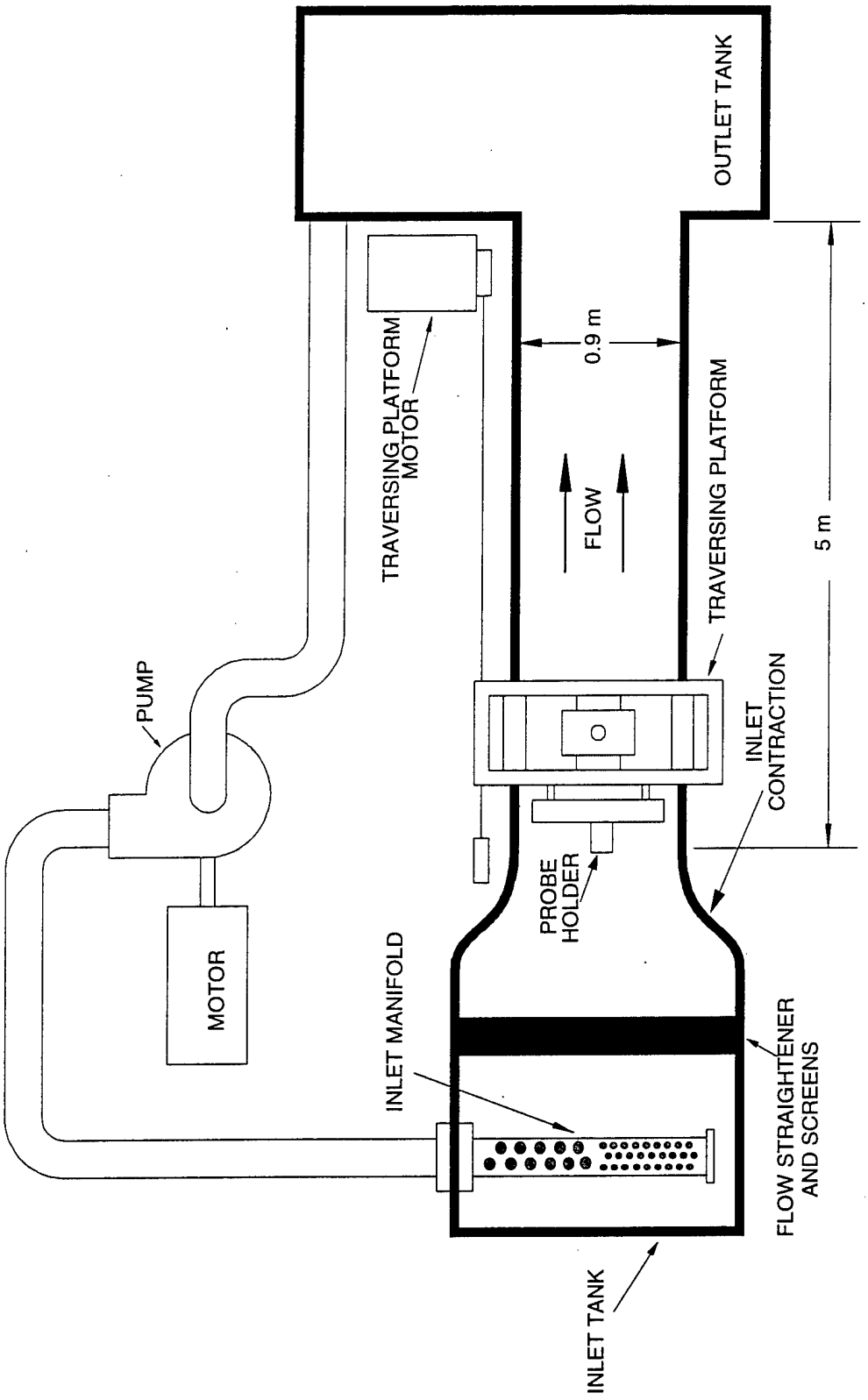

Figure 2.1 Schematic of water channel. Plan view.

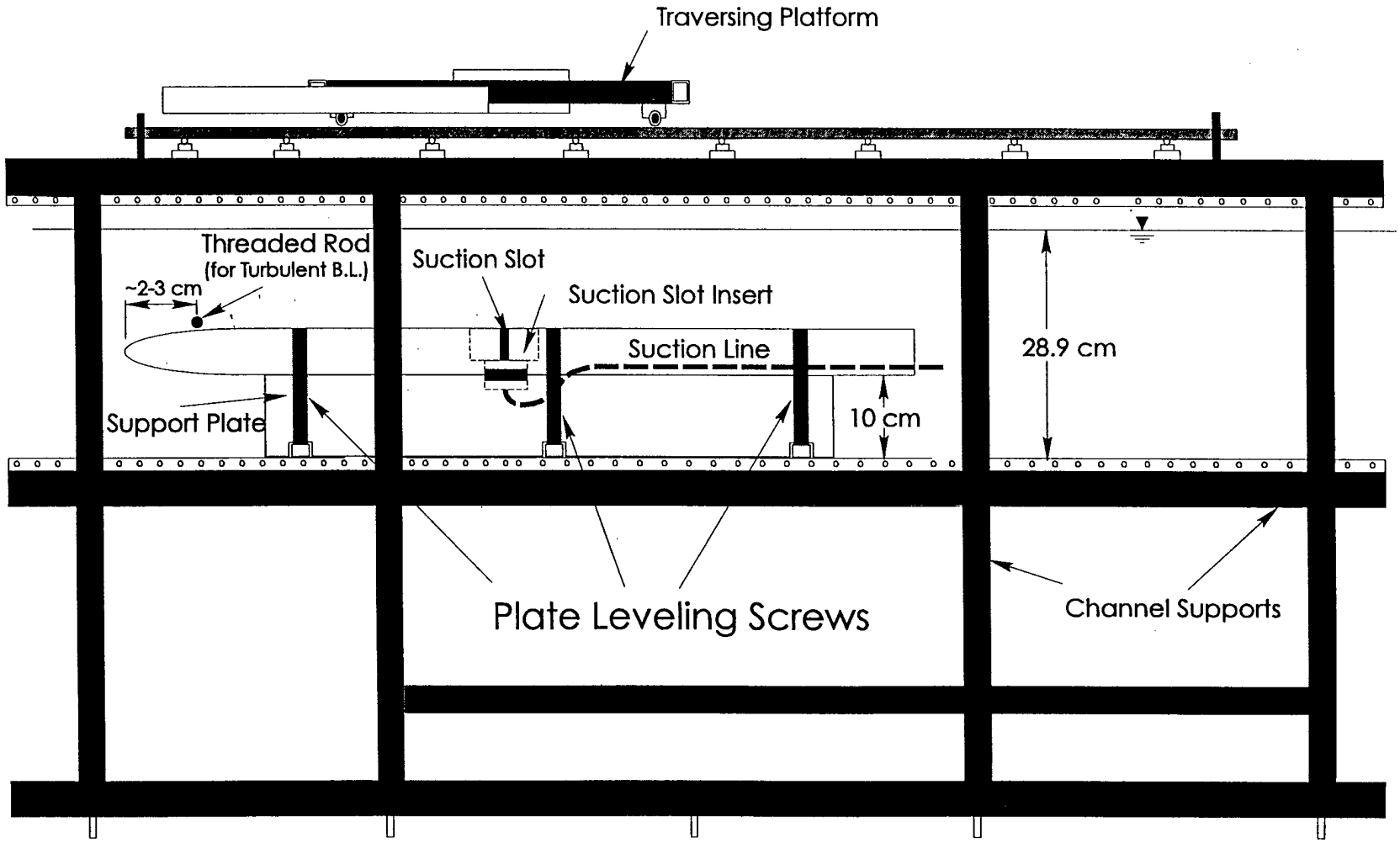

Figure 2.2 Side view schematic of the water channel and test plate.

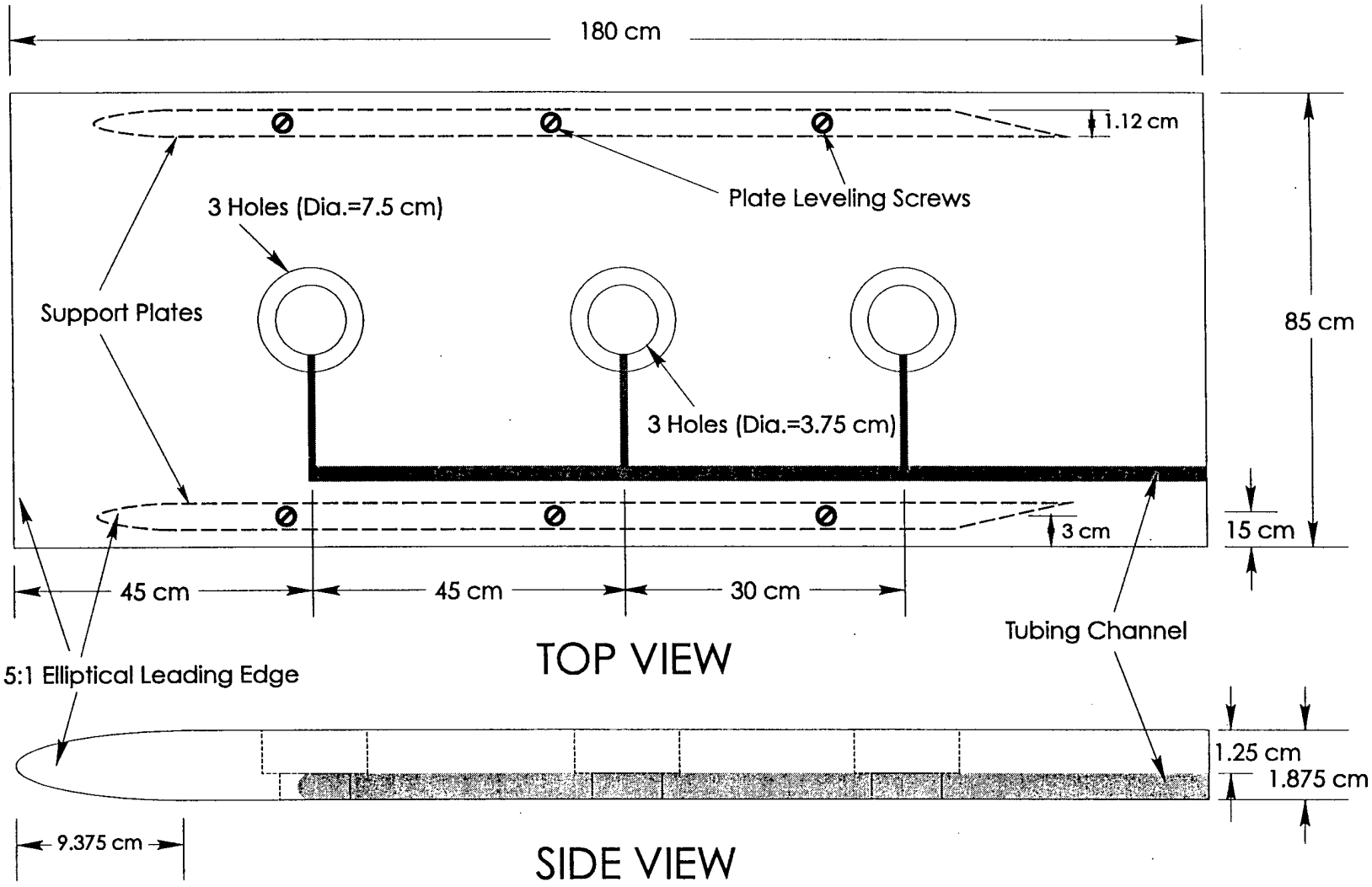

Figure 2.3 Top and side view schematic of the test plate.

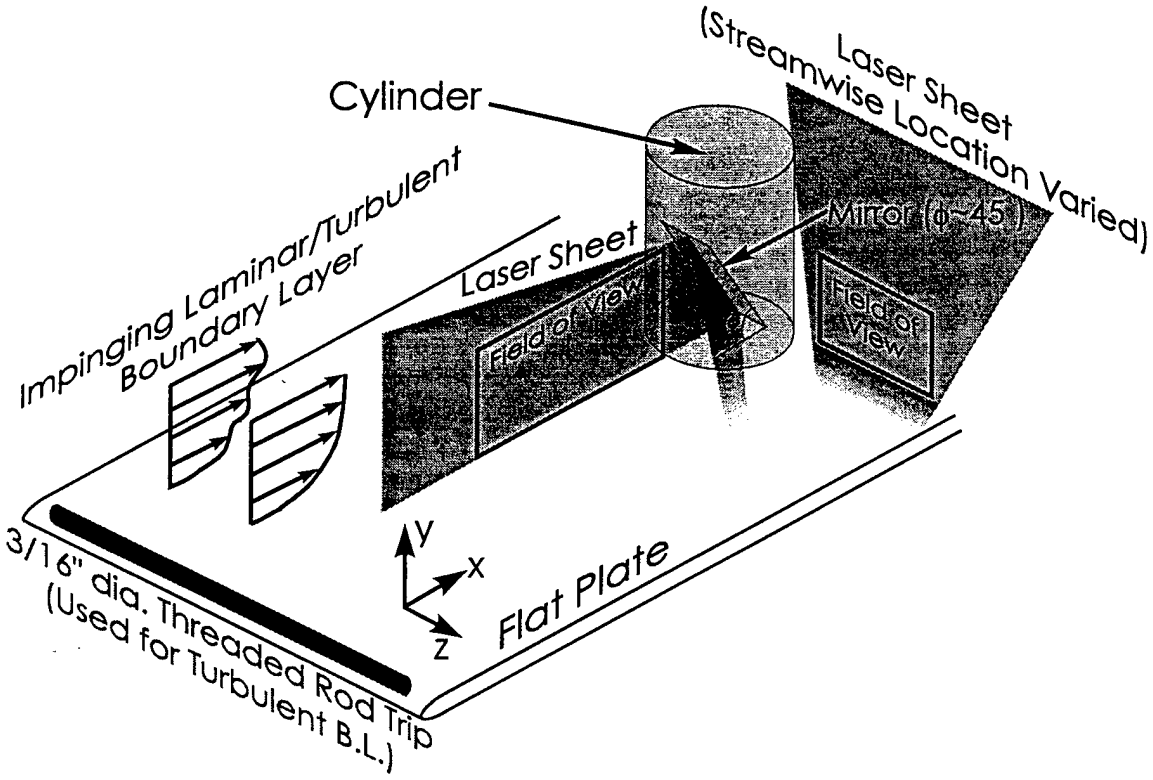

Figure 2.4 Junction geometry schematic showing the location of laser sheets.

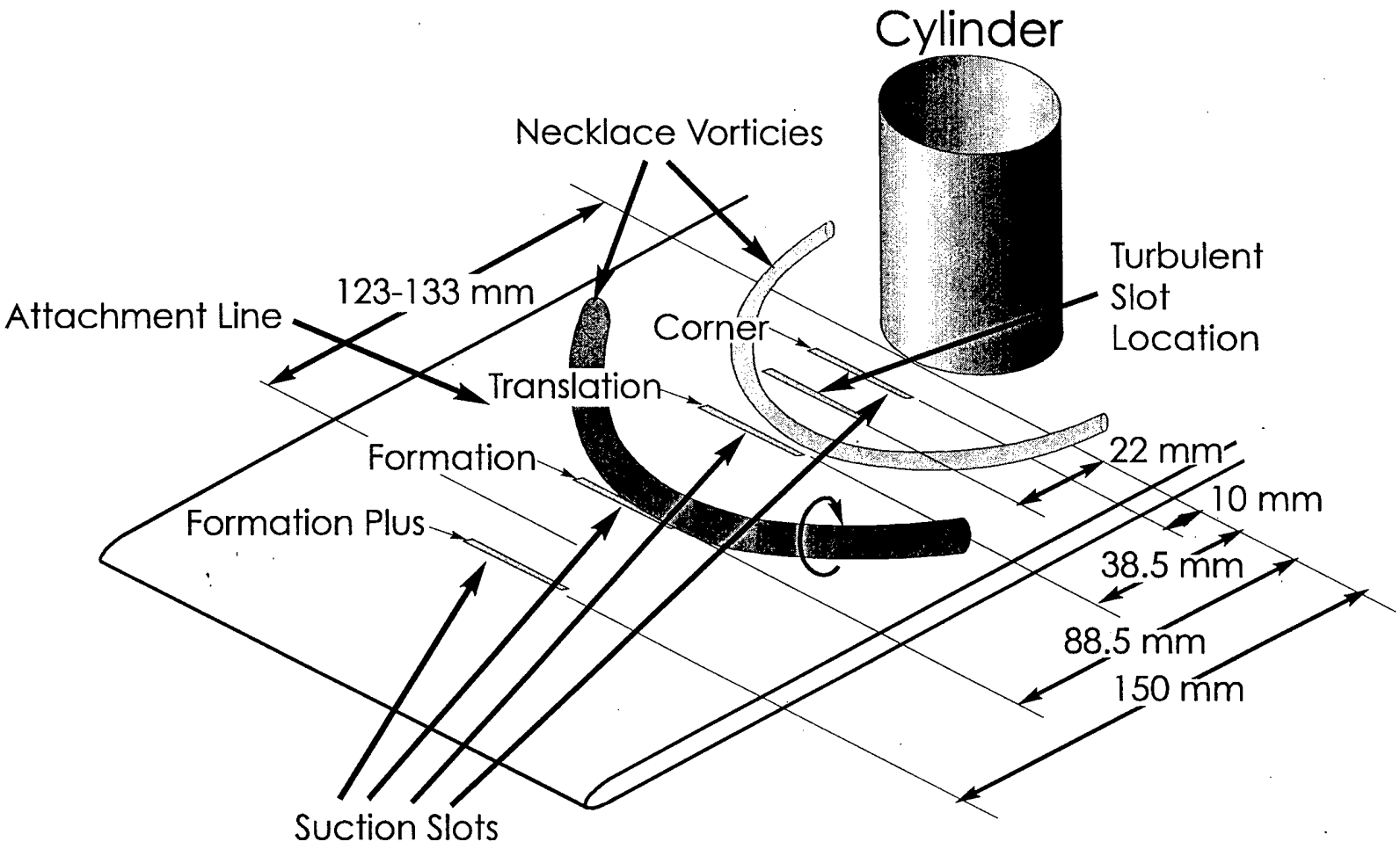

Figure 2.5 Schematic of suction slot locations used for the laminar and turbulent constant-rate suction experiments. Note that the streamwise location of the slot is constant at 90 cm from the leading edge; the cylinder location was varied.

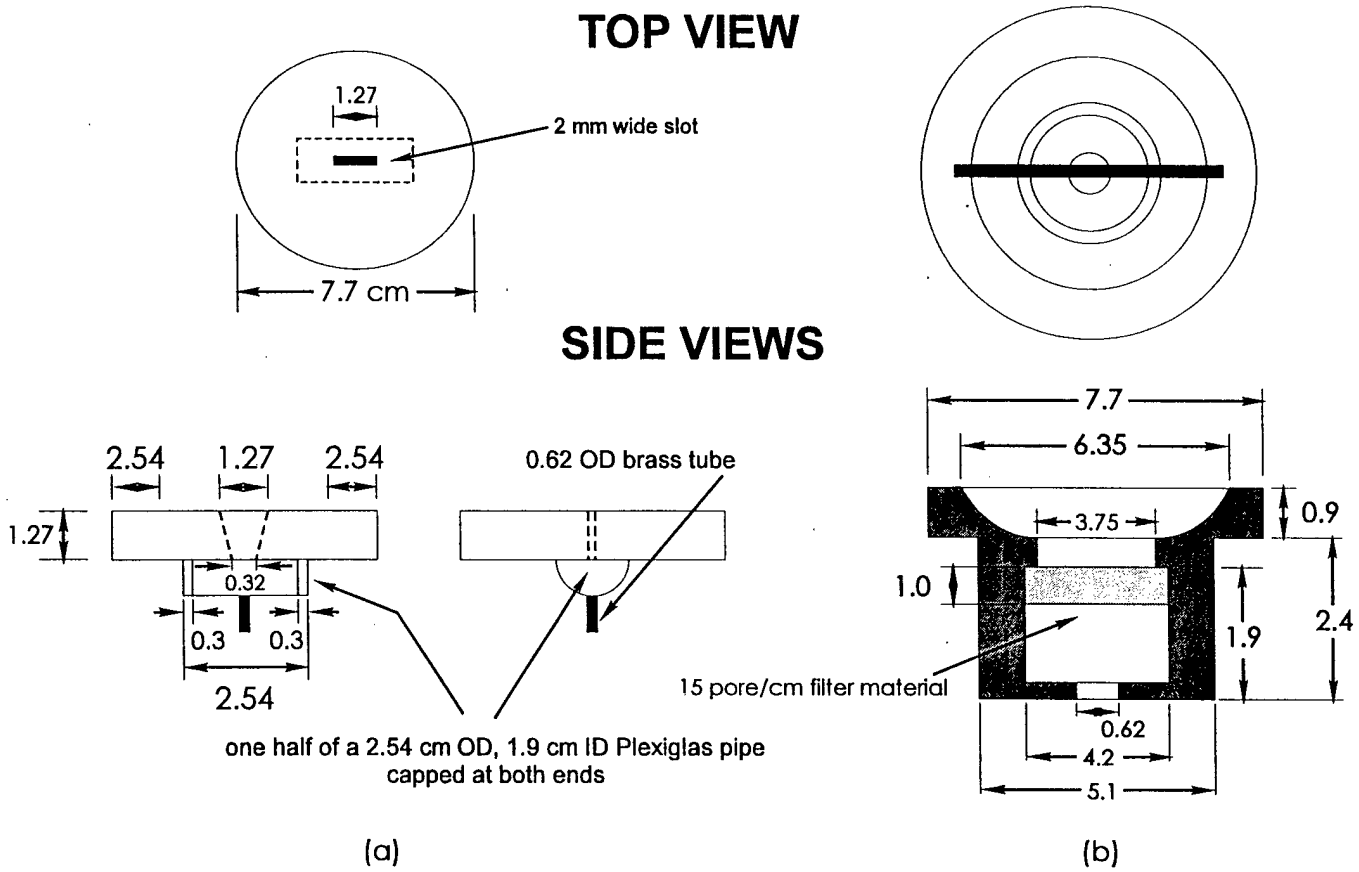

Figure 2.6 Schematic of the suction slot inserts. Dimensions are in centimeters, unless otherwise noted.

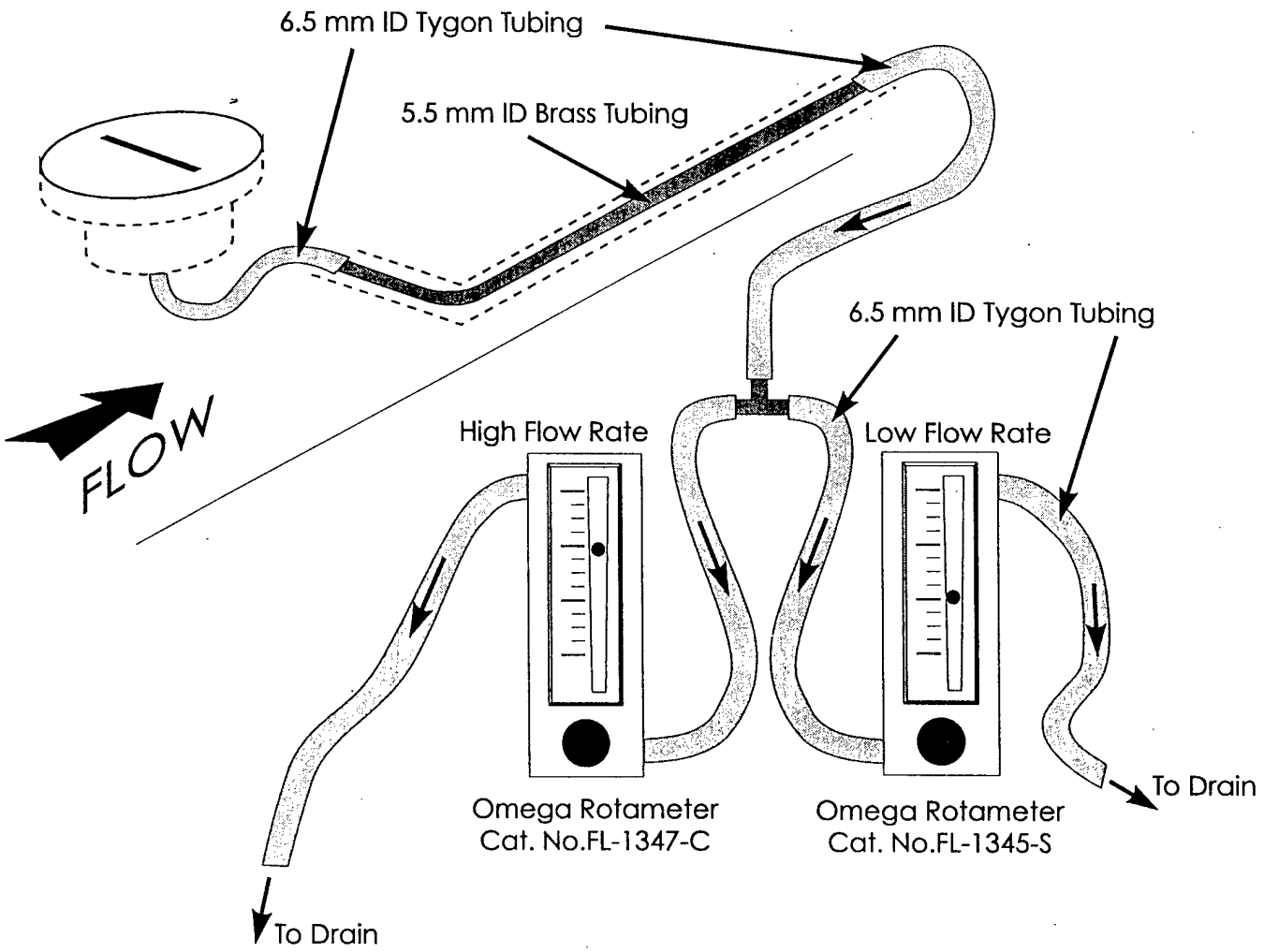

Figure 2.7 Schematic of experimental plumbing.

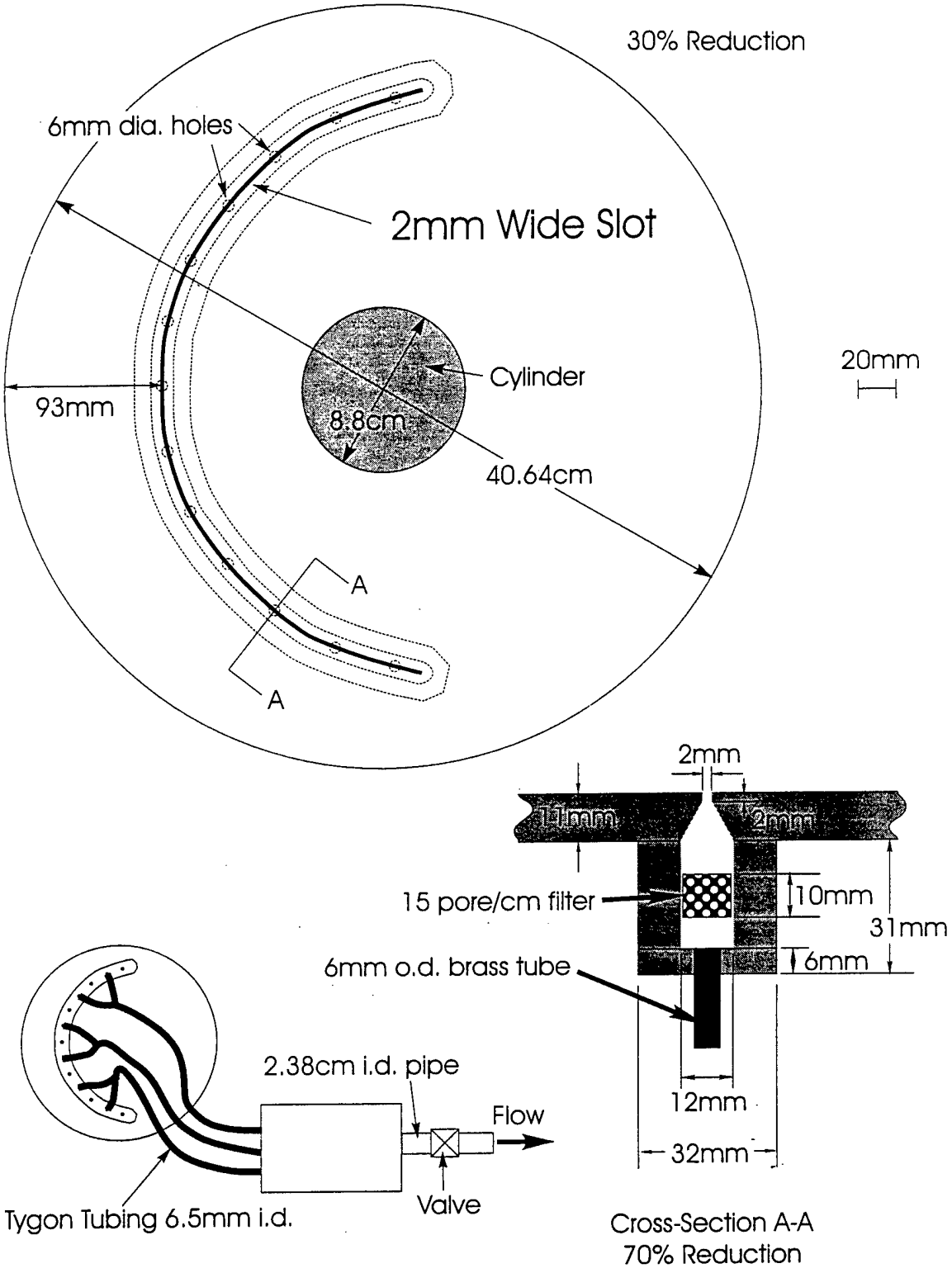

Figure 2.8 Scale drawing of curved suction slot and schematic of plumbing.

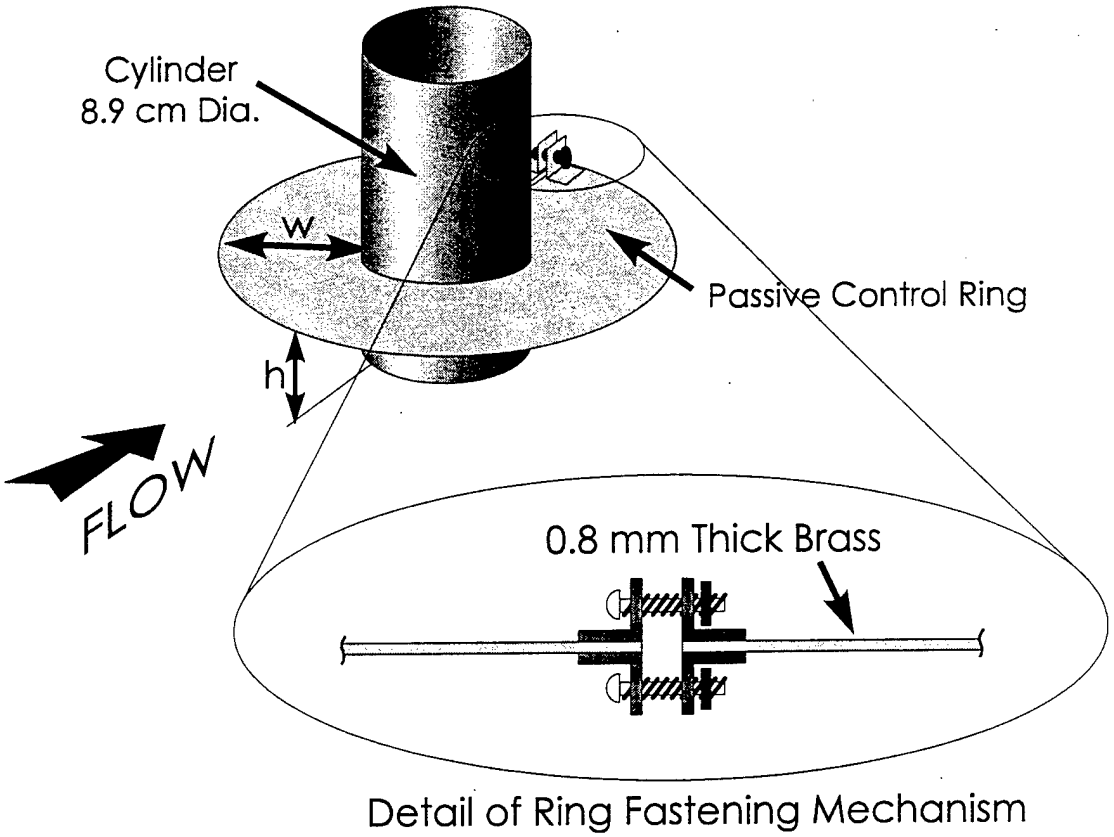

Figure 2.9 Schematic of the control rings and fastening mechanism.

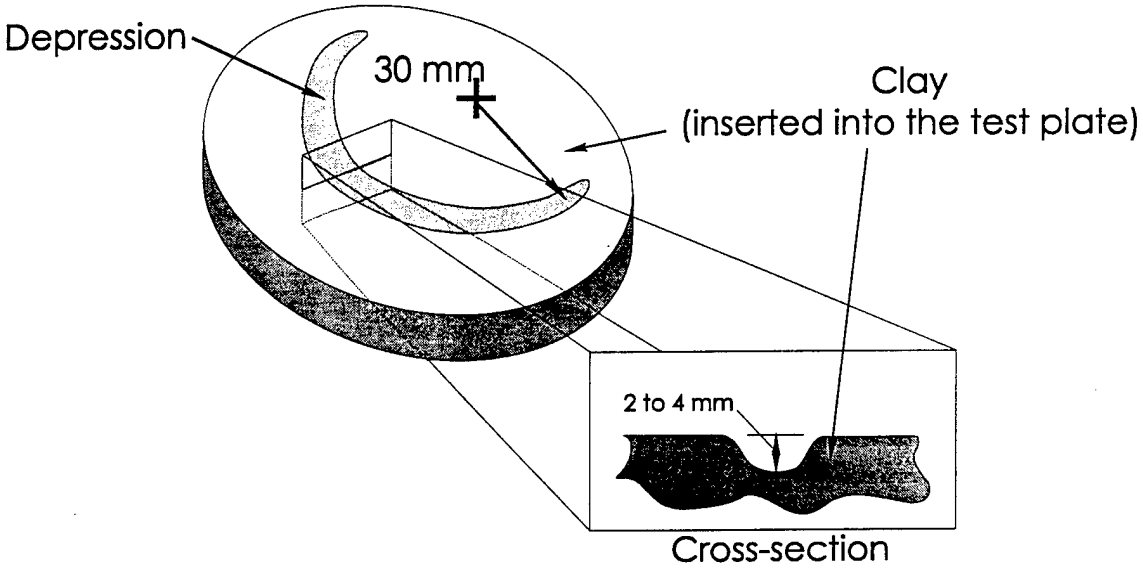

Figure 2.10 Schematic of the flat plate contouring achieved using an oil-based clay.

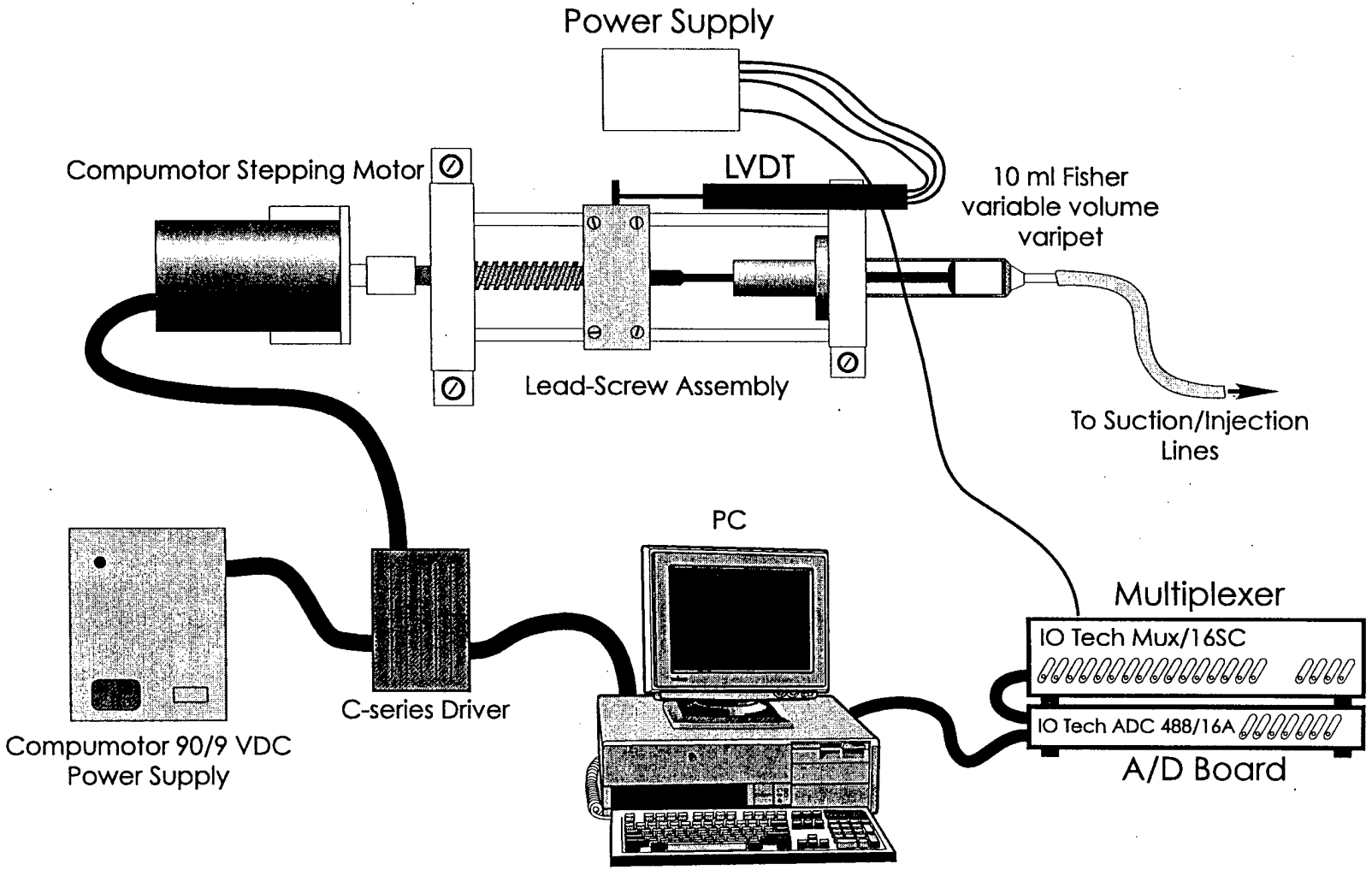

Figure 2.11 Schematic of the Compumotor driven perturbation assembly.

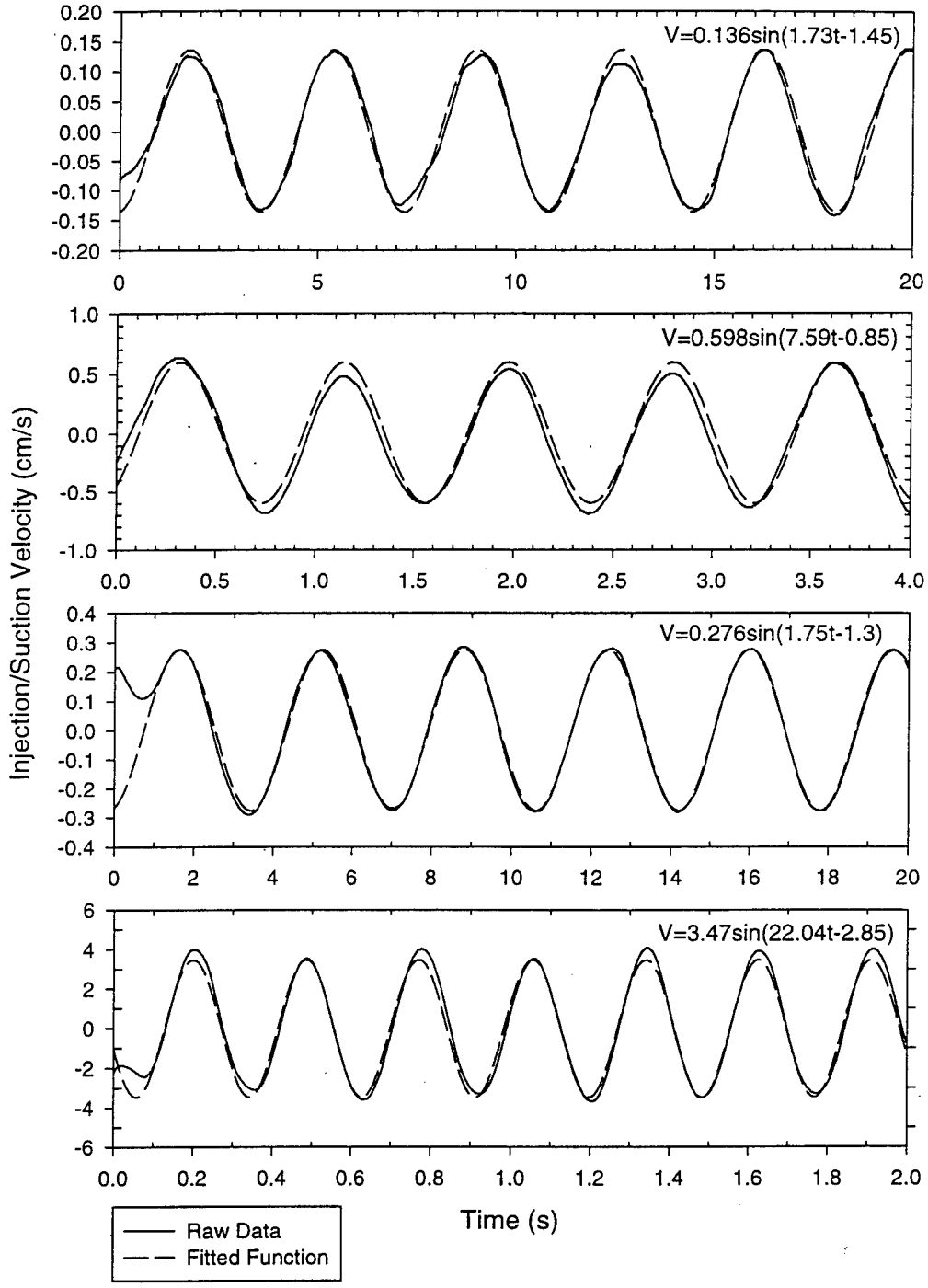

Figure 2.12 Comparison of applied surface velocity perturbations to fitted sine functions.

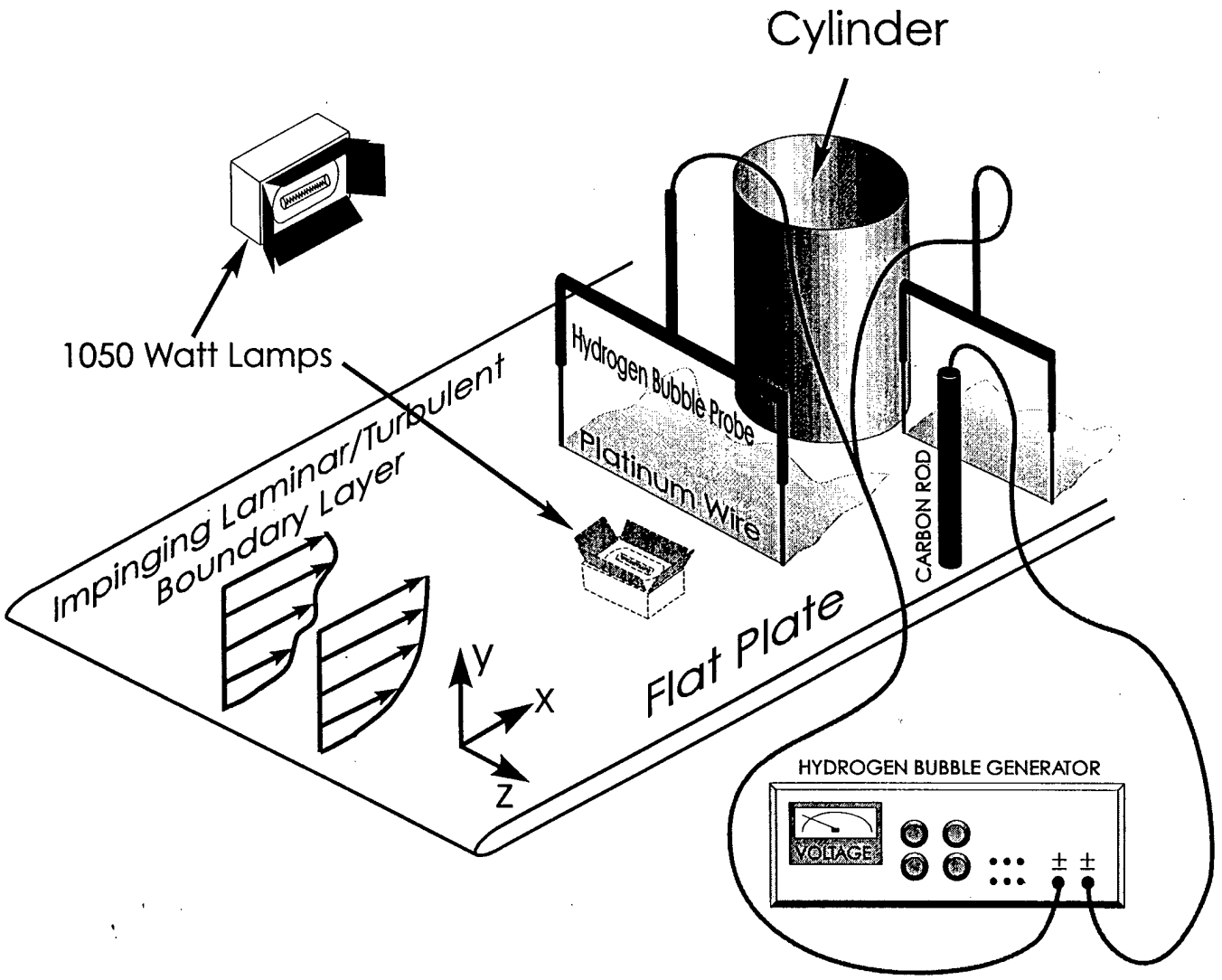

Figure 2.13 Schematic of the hydrogen bubble apparatus.

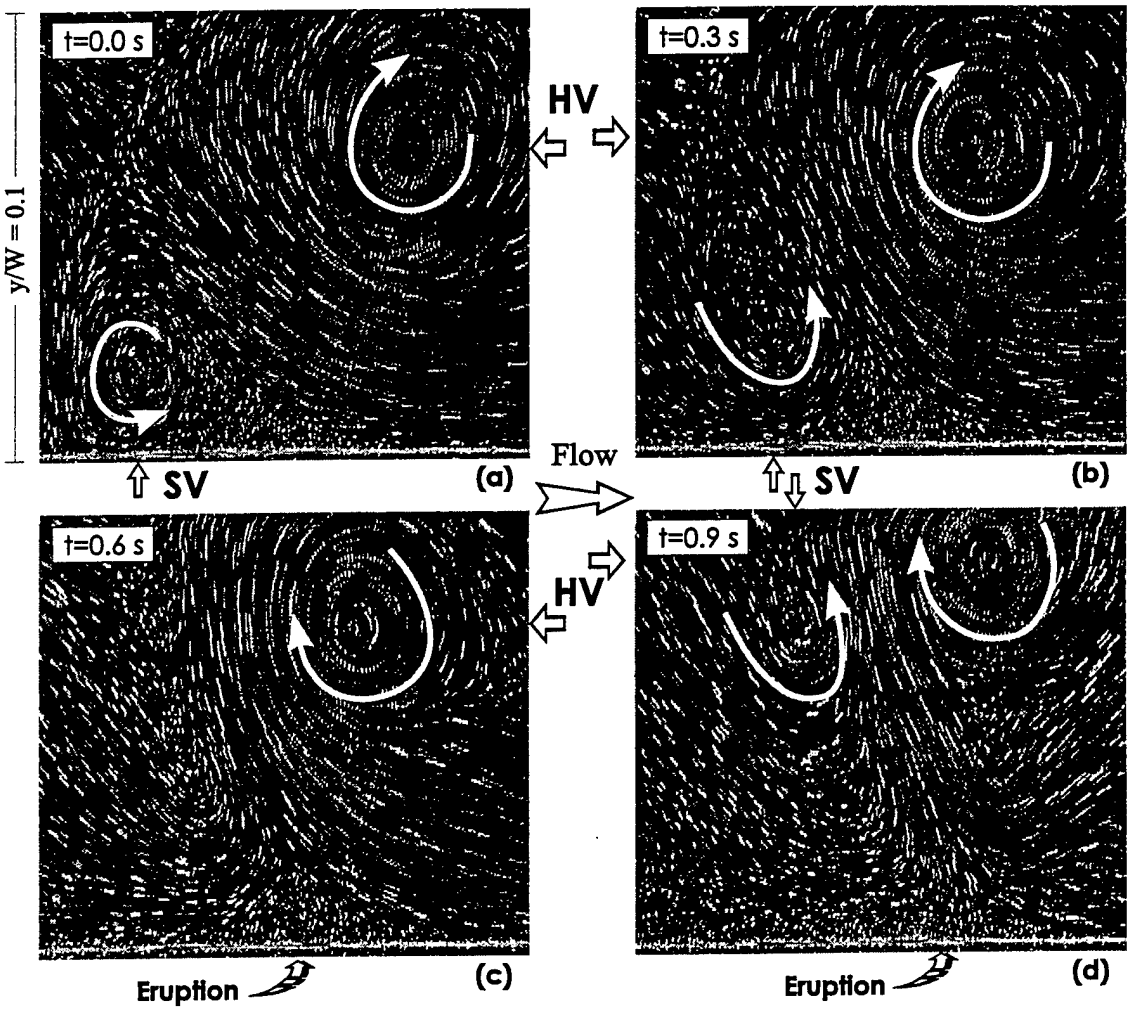

Figure 2.14 Temporal particle visualizations of a turbulent necklace/horseshoe vortex.

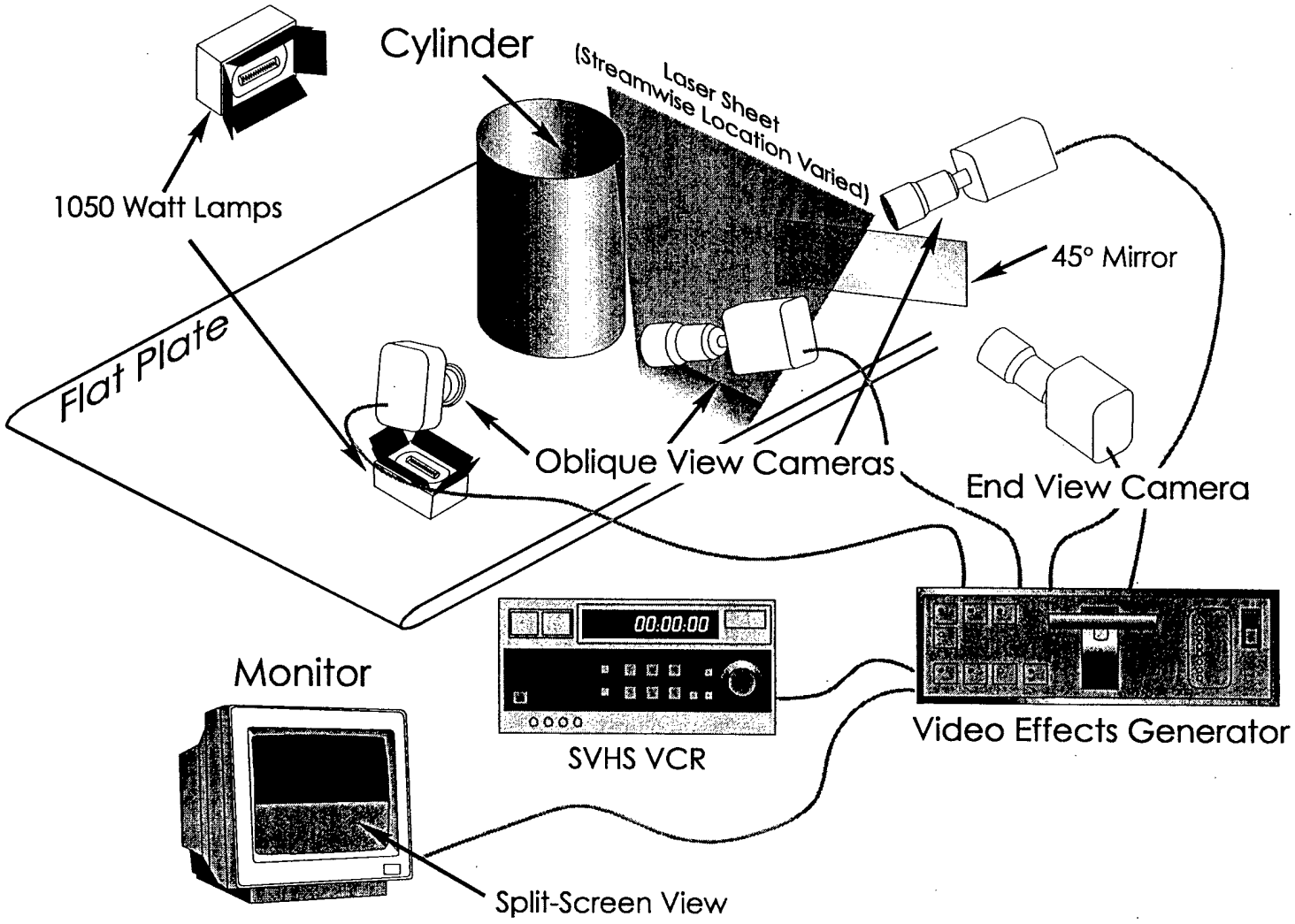

Figure 2.15 Schematic of video configurations.

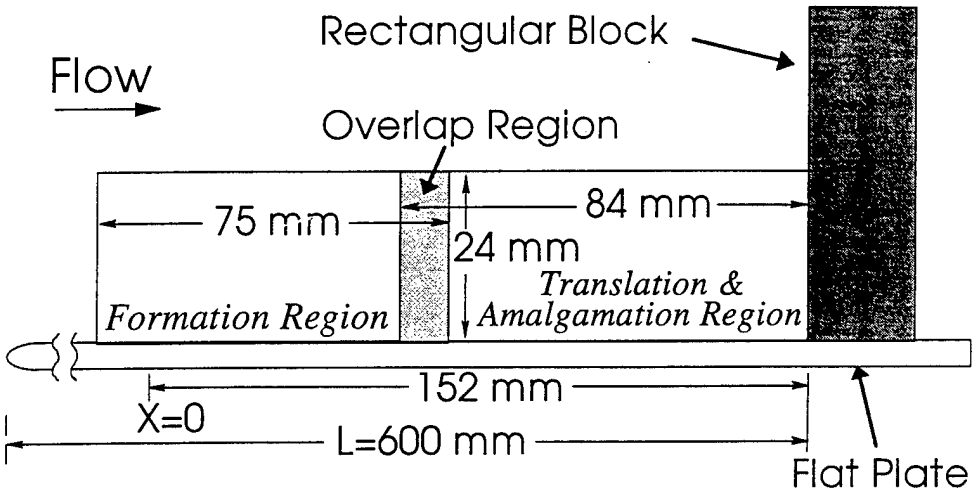

(a)

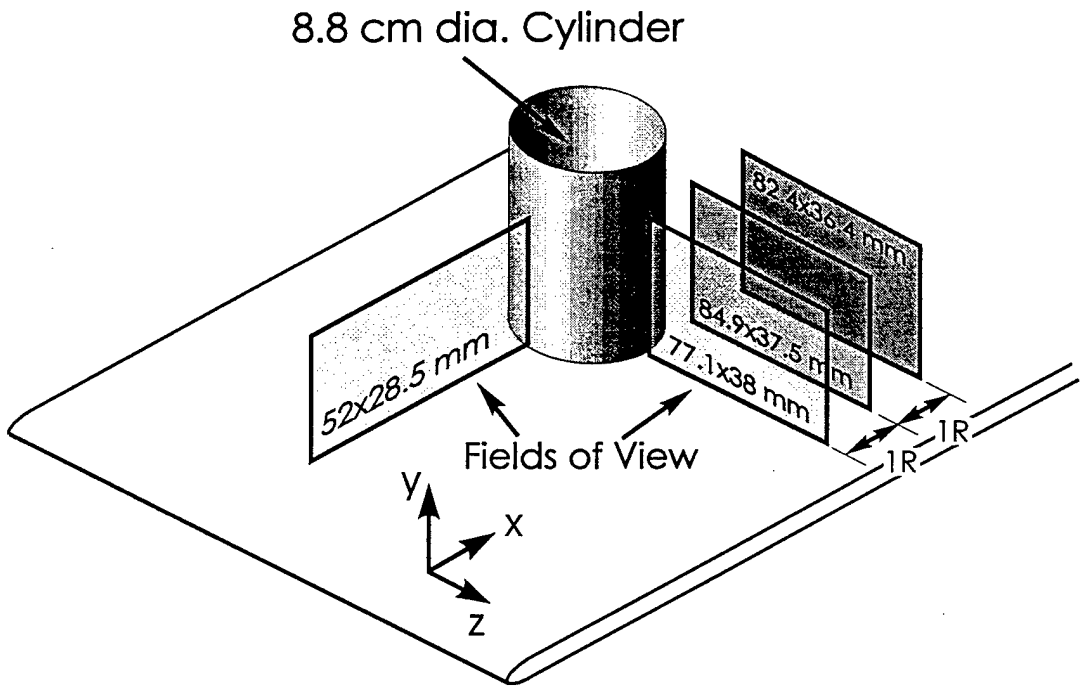

(b)

Figure 2.16 Size and location of the fields of view captured in the (a) laminar and (b) turbulent PIV experiments.

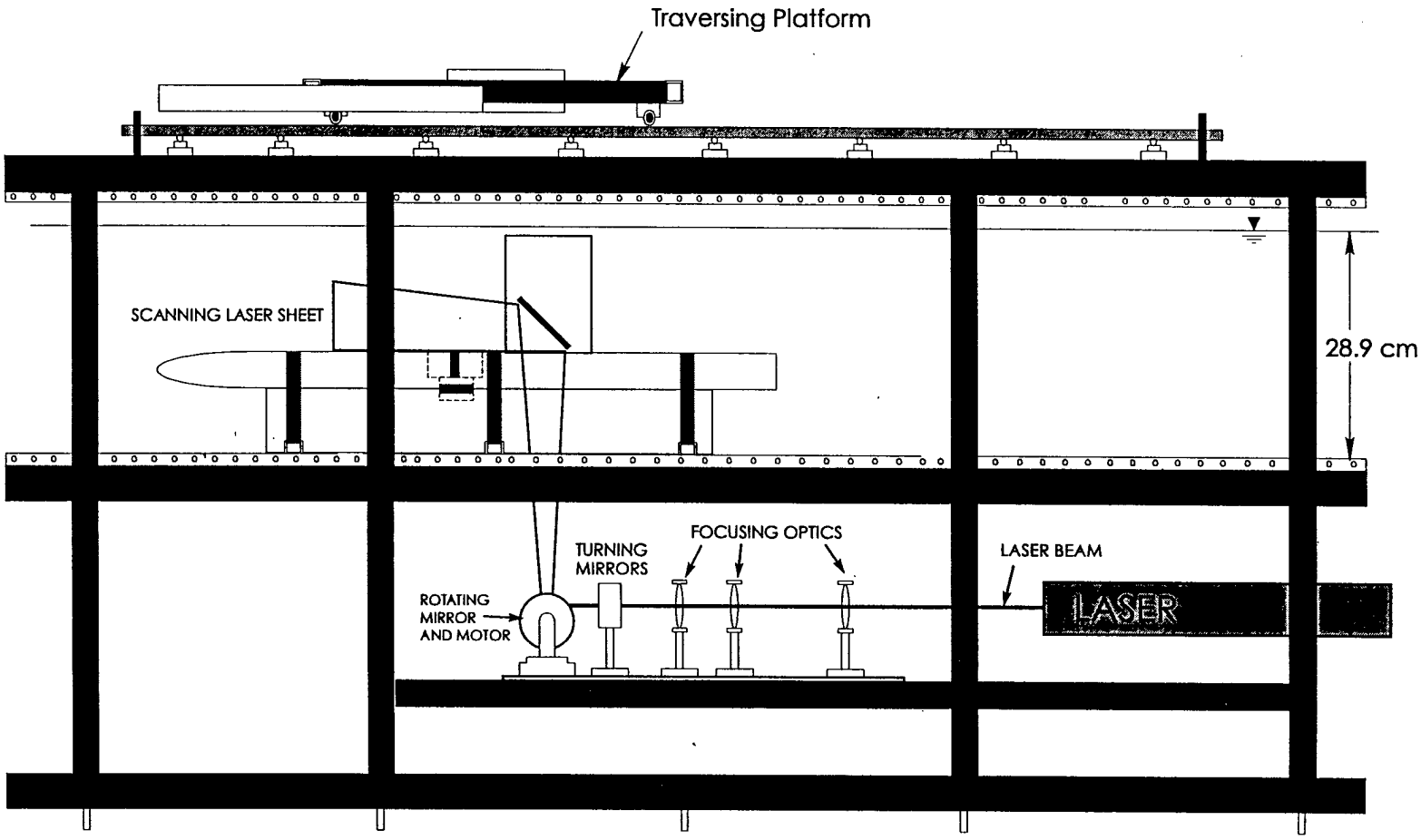

Figure 2.17 Schematic of laser focusing and sheet generating optics.

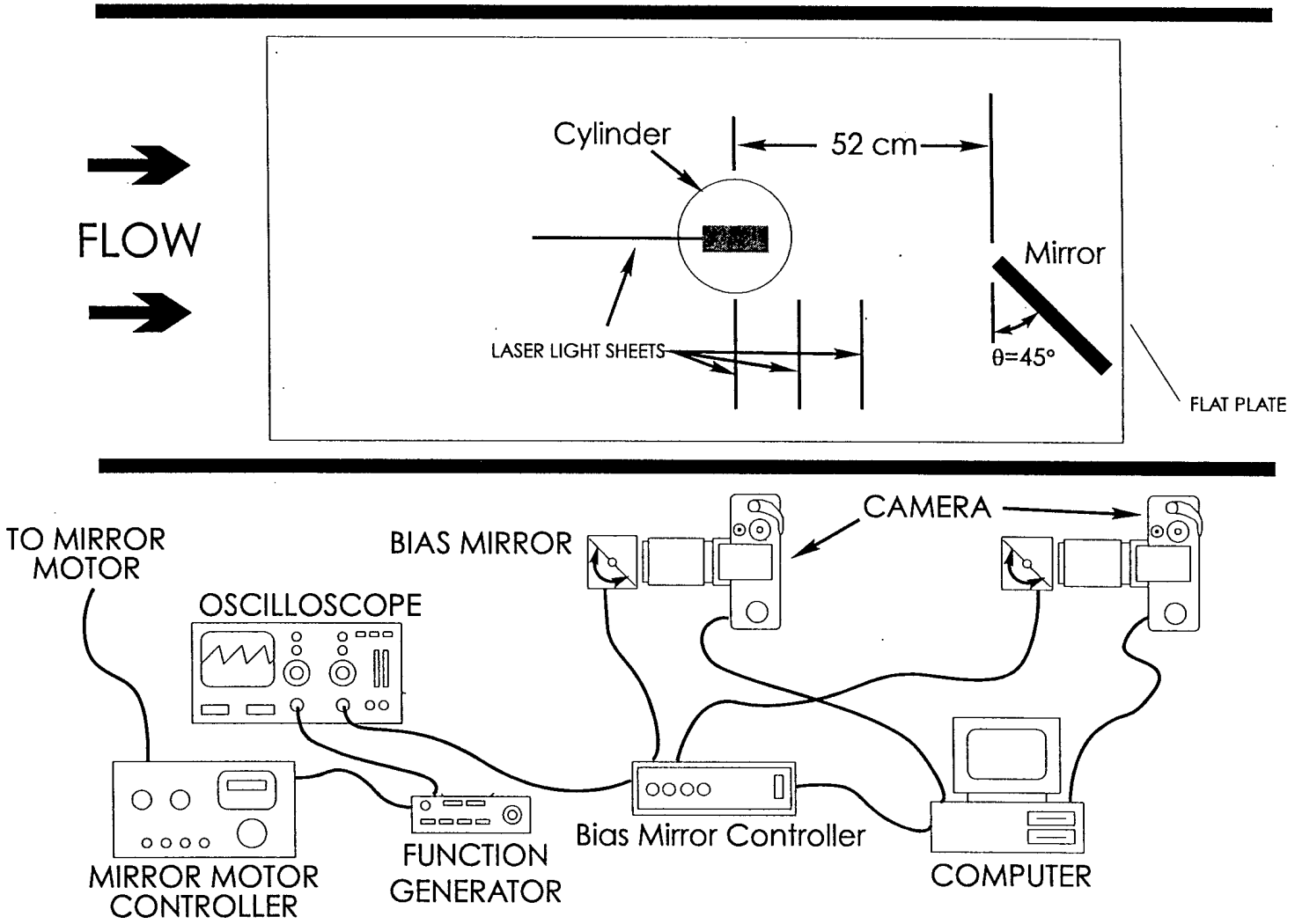

Figure 2.18 Schematic of the PIV configuration.

3.0 LAMINAR JUNCTION FLOW RESULTS and DISCUSSION

3.1 Introduction

This section describes the results of qualitative flow visualization and Particle Image Velocimetry (PIV) for an unsteady laminar necklace vortex system. Experiments were performed on baseline (i.e. without control) and controlled cases. The results of the baseline case study will illustrate, in some detail, the genesis and behavior of the unsteady, laminar necklace vortex system in the breakaway regime. It is important to note that a more comprehensive review of the baseline behavior of junction flows (covering a wide range of Reynolds numbers and behaviors) can be found in Greco (1990) and Seal (1993). The results of the controlled cases will illustrate the effect of control on the topology, periodicity, and strength of the necklace vortex system described above.

3.2 Genesis and behavior of an unsteady laminar necklace vortex system (baseline)

When a laminar boundary layer encounters a wall-mounted bluff body, a necklace vortex system will develop. This system is characterized by the formation of necklace (or horseshoe) vortices (i.e. U-shaped vortex tubes with the two legs extending in the downstream direction, (Figures. 3.1, 1.1, and 3.9), which exhibit a range of behavior depending on Reynolds number (Seal 1993, Greco 1990). Recent studies have shown that the *laminar* boundary layer approaching the bluff body encounters an attachment line

upstream of the body (Visbal, 1991; Coon and Tobak, 1995; Hung *et al.*, 1991; Puhak *et al.*, 1995), where the approaching fluid meets reverse flow created by the pressure gradient generated by the body. Instead of lifting away from the surface (in a classic separation process) the impinging fluid deflects laterally along the surface of the plate and around the sides of the body, forming a shear layer downstream of the attachment line (figure 1.1 (a) and (b)). This is in contrast to the previously accepted belief (and what was reported in the present author's previous Studies (1993, 1995)) that the boundary layer in laminar junction flows undergoes a classical separation. Downstream of this attachment (in the shear layer formed by the reverse flow and impinging fluid, figure 1.1 (b)) the impinging boundary layer vorticity organizes into coherent, necklace or horseshoe, vortices described above in §1.1. The laminar case is characterized by 5 regimes of behavior (Greco, 1990):

(i) Steady - One, two or three steady state vortices develop, with the number of vortices increasing with Re;

(ii) Oscillating - The vortices oscillate periodically with the frequency increasing with Re;

(iii) Amalgamating - The primary vortex (the vortex closest to the body) breaks away from the formation region and advects towards the body, but is subsequently drawn back to and amalgamates with the secondary vortex (the vortex following the primary vortex), forming a new primary vortex.

Amalgamation is a periodic event for which frequency again increases with Re;

(iv) Breakaway - The primary vortex periodically breaks away from the formation region and advects downstream towards the body. The frequency of breakaway increases with increasing Re;

(v) Transitional - The entire vortex system destabilizes into three-dimensional, turbulent-like behavior.

To examine the baseline case for the laminar study, PIV experiments were performed on a laminar, unsteady necklace vortex system in the breakaway regime (regime iv) for a flat plate-rectangular block junction; this regime is characterized by organized and periodic redistribution of impinging vorticity into discrete vortices, as well as the presence of clearly defined vortex-surface interactions. The characteristics just described are exhibited to some extent in all laminar regimes of behavior and also appear sporadically in the turbulent case. The rectangular block was chosen to increase the size and lateral extent of the necklace vortices, thereby allowing the acquisition of detailed PIV results. Because the formation of the necklace vortex system is primarily a *streamwise* pressure gradient induced phenomenon (Greco, 1990; Seal, 1993) and since the *streamwise* pressure gradient created by a rectangular block is qualitatively similar to those created by any number of bluff bodies (e.g. a cylinder or airfoil), general

conclusions about the nature of unsteady laminar junction flows, based on the results of the PIV experiments for a rectangular bluff body should be valid for a bluff body of any shape.

3.2.1 *Vorticity*

Since numerical approximations for derivative computations are subject to high uncertainties, a Stokes' theorem approach was used in lieu of a finite-difference representation of the defining equation

$$\omega_z = \frac{\partial v}{\partial x} - \frac{\partial u}{\partial y}, \tag{1}$$

to reduce the uncertainty of the vorticity calculations. Thus the z-direction vorticity field was established using Stokes' theorem, which can be written generally as:

$$\iint_A \vec{\omega} \cdot d\vec{A} = \oint_c \vec{u} \cdot d\vec{s}\,. \tag{2}$$

Assuming the vorticity to be constant over $\vec{A}$, the z-direction vorticity is given by

$$\omega_z = \frac{1}{4\delta_z \delta_y} \oint_c \vec{u} \cdot d\vec{s}, \tag{3}$$

where δ_x and δ_y are the step sizes between two adjacent velocity vectors in the x- and y-directions, respectively. The vorticity at a point was calculated from equation (3) by numerically integrating around a rectangular path defined by the eight points adjacent to a selected point.

Figure 3.2 is a time sequence of vorticity contours on the symmetry plane (for the 1.0mm resolution cases) covering slightly more than one complete vortex generation-

breakaway cycle. Here data sets from the two fields-of-view (figure 2.16 (a)) were phase matched and combined to yield a complete flow field. In addition, figure 3.2 shows the peak vorticity values associated with the organized vortical structures at each time step* .

As the sequence begins, the impinging boundary layer vorticity (negative; indicated by dashed lines) begins to organize into a primary necklace vortex (at approximately x/W=0.3). As time proceeds, this primary vortex strengthens and advects downstream (at about 16% of the local free-stream velocity), assimilating more impinging boundary layer vorticity. Simultaneously, the vortex begins to interact with the plate surface, generating opposite-sign vorticity via a local, vortex-induced pressure-gradient effect (Doligalski, *et al.*, 1994) which manifests itself as a region both directly beneath the vortex and as a growing "tongue" just trailing the vortex. This eruptive "tongue" of vorticity increases in strength and penetration into the boundary layer as the primary vortex grows. Eventually, the interaction between the vortex and the surface becomes so strong that this eruption of opposite-sign vorticity effectively severs the primary vortex from the impinging boundary layer vorticity (at approximately t=3.0s), allowing the primary vortex to "breakaway" from the formation region; the newly-released vortex accelerates to a velocity of about 30% of the local free-stream, becoming a translating vortex (t=3.0 to 6.0s). At the point of breakaway, the primary vortex is roughly 14-15mm in diameter [based on the extent of the lowest closed vorticity contour ($-1s^{-1}$)], representing approximately 81-87% of the equivalent, unobstructed Blasius boundary layer thickness at the block location (x=0.6m).

---

* The location of the vertical bars correspond to the x-location of the peak vorticity measurement.

The newly-released translating vortex advects downstream into the junction corner region, where it decelerates to about 17% of the local free-stream velocity, and subsequently amalgamates with and reinforces a corner vortex (t=1.0s to 5.0s). Just prior to amalgamation, the vortex diameter has decreased to approximately 11-13mm (64-75% of the equivalent Blasius boundary layer). The reinforced corner vortex then remains in the corner region, awaiting the arrival of a new translating vortex. The repetition frequency of these events for the particular breakaway case examined was 0.2 Hz, yielding a Strouhal number based on block width of 0.605, which is 3.6 times greater than the measured wake vortex shedding Strouhal number of 0.17 for the rectangular block.

Plotted adjacent to the vorticity contours in figure 3.2 are values for the peak vorticity associated with both the developing and fully-formed necklace vortices; generally, these peak vorticity values occur at the center of the vortical structures. The temporal sequence of peak vorticity values indicates a temporal increase in the vorticity of the primary vortex as it accumulates impinging boundary layer vorticity. Following breakaway (at about t=3.0s), the peak vorticity of the primary vortex continually increases, until amalgamation occurs with the corner vortex. This vorticity amplification is presumably due to the stretching of the vortex tube, caused by the three-dimensional deformation of the vortex tube around the sides of the body.

3.2.2 *Magnitude of Circulation*

Figure 3.3 shows the non-dimensional circulation strength and trajectory of the vortices in the translation and amalgamation region (after breakaway) derived from the

data of figure 3.2, as well as for one additional data set at t=-1s. Circulation was calculated from the velocity data using a line integral

$$\Gamma_v = \oint \vec{V} \cdot d\vec{s}, \tag{4}$$

where the integration path was the minimal closed contour of constant negative vorticity (ω=-1s^{-1} was taken to be the bounding curve of the vortices); the circulation is non-dimensionalized on the equivalent cyclic circulation (Γ_e) determined by integrating the vorticity flux passing across the upstream edge of the flow field during one formation-breakaway cycle. The circulation behavior was not established for the formation region because the ω=-1s^{-1} vorticity contour does not clearly define a closed vortex contour within this region.

Notice that although the peak vorticity values *increase* following breakaway, the circulation strength of the vortices *decreases* up to the point of amalgamation. At the point of amalgamation (t=4.0s), the strength of the corner vortex increases sharply due to the vorticity contributed by the primary vortex. Note that the data points corresponding to the amalgamating vortices at t=4.0s in figure 3.3 are indicated by different positions, but reflect the same strength for each vortex; this is because the ω=-1s^{-1} contour (used to define the boundary of a vortex) *engirdles both vortices*, such that the strength is merged, although at this point the vortices still have distinct centers. Immediately following amalgamation, the new corner vortex rapidly decreases in strength, due to the apparent cross-diffusion of vorticity between the necklace vortex and the ejected opposite-sign vorticity generated by the vortex-surface interaction.

This cross-diffusion hypothesis is supported by an examination of the physical processes taking place in the corner region. Note that as the necklace vortices approach the block, they undergo stretching. It is known that during stretching the circulation of an isolated vortex will be conserved in the absence of flux or diffusion of vorticity across a material boundary which initially encompasses all the vortex vorticity. Since the present measurements indicate a substantial decrease in circulation strength, this suggests that viscous effects are responsible for the decrease. There are two ways that viscous effects can come into play. First, vorticity can diffuse across the ω=-1s^{-1} boundary; secondly, the vorticity comprising the vortex could cross-diffuse with the corresponding opposite-sign vorticity that is generated at the surface and circulates around the vortex (e.g. see the corner vortex in figure 3.2 for t=3.0s). The relative importance of these two mechanisms was examined by modeling the necklace vortex as a decaying Oseen vortex matched to the equivalent size and strength of the present vortices; the temporal decay in the strength was then examined [see Seal *et al.* (1995) for details]. The model suggests that pure diffusion processes could only account for a possible 8% decrease in circulation strength of the vortex when considered for the period t=-1.0s to 3.0s, whereas a decrease of approximately 50% was noted for the present study. This suggests that pure diffusion will play only a small part in the noted vortex decay process, and that a significant cross-diffusion of vorticity must be taking place, leading to a consequent reduction in vortex strength.

3.2.3 *Streamlines*

Instantaneous streamlines for the data corresponding to figure 3.2 were determined (figure 3.4) and topologically assessed using the criteria of Perry and Steiner (1987). The streamline patterns of figure 3.4 illustrate stable foci (the spiraling of streamlines into a central point), which are a known feature of a vortex undergoing stretching (e.g. the sectional streamlines of a Burger's vortex). Also, the streamline patterns of figure 3.4 exhibit several examples of stable limit cycle behavior (Perry and Steiner, 1987). For example, in the translation and amalgamation region at t=1.0s, the translating vortex (labeled T.V.) at the right side of the field of view exhibits a stable limit cycle (i.e. both a (1) spiraling inward of external streamlines to a limiting, closed streamline, and (2) an outward spiraling of streamlines from the vortex center to that same closed streamline); simultaneously, the corner vortex (labeled C.V.) displays closed streamlines inside a limiting streamline, suggesting two-dimensional flow. The number of occurrences of closed streamlines is, however, much less than the number of appearances of foci and limit cycles. Limit cycles are also observed occasionally in the formation region, as evidenced for t=3.0s, where the new primary vortex (denoted N.P.V.) also exhibits a stable limit cycle. Expanded illustrations of these limit cycle patterns for the particular vortices are plotted at the right side of figure 3.4.

Figure 3.5 shows a streamline plot for one of the more highly-magnified (increased spatial resolution) data fields, roughly corresponding to the formation region of t=1.0s in figure 3.4; this figure again illustrates the clear presence of limit cycle behavior. The reason for the appearance of limit cycles in the necklace vortices is not immediately

clear, but several possibilities exist. First, the necklace vortices may have a two-celled vortex structure like those described by Sullivan (1959), which would display a limit cycle pattern (Perry and Steiner, 1987). However, the velocity profiles plotted in figure 3.6, which are representative of the necklace vortices throughout the temporal cycle, display the characteristic shape of only a single-celled structure (Sullivan, 1959). In addition, the limit cycles appear intermittently, which suggests some kind of transient phenomenon as the cause of the limit cycle patterns; hence, this two-cell hypothesis seems to be precluded. A more viable possibility may be that the limit cycle patterns are a result of a local deceleration of the axial core flow caused by local, transient, pressure fluctuations along the vortex axis, which could cause a change in the sign of the local gradient, $\partial w/\partial z$, from positive (stretching) to negative (compression). This would be similar to behavior of a leading edge vortex on a delta wing, as described by Visbal and Gordnier (1994), who show that the crossflow topology of the vortex can vary, depending on the axial velocity gradient ($\partial w/\partial z$), as well as the ratio of axial-to-circumferential velocity components. Thus, the appearance of limit cycles in the present results could possibly be explained by continuity considerations (e.g. if the necklace vortex core undergoes stretching, its diameter must decrease, resulting in the observed inward spiraling of streamlines; conversely, compression along the vortex axis will cause expansion of the vortex core, resulting in outward spiraling of streamlines). Clearly, this observed limit cycle behavior requires further investigation to establish its cause.

Further examination of figure 3.4 indicates an interesting modification in the topology of the formation region between t=0.0s to 2.0s. Beginning at t=0.0s, the

streamlines that feed into the induced, counter-rotating vortex (labeled I.V.) in the formation region first pass over the top of the primary vortex (downstream of the I.V.) and then turn upstream to feed the induced vortex. However, by t=1.0s the streamlines feeding the induced vortex no longer pass around the primary vortex, but rather pass over the developing primary vortex (upstream of the I.V.) and then dive down, upstream of a saddle point, to feed the induced vortex (also clearly seen in figure 3.5). This temporal change in feeding topology was also observed in Visbal's (1991) computations of an unsteady laminar juncture flow. This change in topology appears to be associated with the process of primary vortex breakaway. Referring back to figure 3.2, the tongue of opposite-sign vorticity extending away from the wall, begins to project upward at t=1.0s, initiating a severing of the primary vortex from the formation region; this process of severing becomes essentially complete by approximately t=3.0s. It is speculated that this change of topology reflects initiation of the vortex severing process that leads to release of the primary vortex.

3.2.4 *Velocity Profiles*

Figure 3.6 shows selected u-velocity profiles for t=5.0s, which are very similar to profiles obtained computationally by Visbal (private communication) for a cylinder-flat plate junction in the laminar breakaway regime. The indication of a reverse wall flow for the most upstream velocity profile suggests that the necklace vortices form well within the region of influence of the adverse pressure gradient produced by the block. Indeed, an examination of the inviscid solution for this type of stagnation flow indicates that the

upstream edge of the present field of view is still well within the region of relatively high adverse pressure gradient; the non-dimensional pressure gradient is roughly 0.4 at the upstream edge (x/W=0), compared to a peak gradient of 0.9 at approximately x/W=0.61.

Figure 3.6 shows several *u*-velocity distributions for t=5.0s. Note that velocity profiles of the right sides of t= 0.0 and 4.0s can be found in Seal *et al.* (1995). From figure 3.6, velocity distributions of the primary and corner vortices appear similar to those of a decaying potential or Lamb-Oseen vortex, with a central core similar to solid body rotation. This observation is supported by figure 3.7, which illustrates favorable comparisons of the wall-normal vorticity distributions of the necklace vortex, at three different states of development, to fitted vorticity distributions for a Lamb-Oseen type vortex (a Gaussian distribution). Also note the decrease in Γ (the strength of the vortex) from (B) to (C), which matches the behavior of figure 3.3. In addition, the region between the vortices displays Blasius-like behavior, taking on inflectional shapes adjacent to the vortex. Peridier *et al.* (1991) showed (in a computational study of a vortex above an infinite plate in the limit $Re \rightarrow \infty$) that pronounced inflectional profiles are a characteristic of vortex-induced boundary layer separation. The inflectional-shaped profiles observed in the present study, are similar (albeit less pronounced due to the relative strength of the vortices) to the profiles computed by Peridier (1991), suggesting the presence of similar local separation processes.

3.3 Flow Control

3.3.1 *Constant rate suction*

The influence of spatially-limited surface suction on an unsteady laminar necklace vortex system in the breakaway regime was examined using the suction slot described in chapter 2. The experimental procedure consisted of: (1) Locating the slot in one of four upstream locations relative to the cylinder (formation+, formation, translation, and corner; chapter 2); (2) Systematically varying the rate at which fluid was removed by the slot (table A.3 in the Appendix gives an inclusive list of all the suction rates employed in the present study); (3) Recording the effects on the system via hydrogen bubble and particle visualizations. Upon review of the experimental results it was observed that, *based on the effect of suction on the system*, the suction rates can be grouped into three general levels; low ($V_{suction}/U_\infty$=0 to 0.15), moderate ($V_{suction}/U_\infty$=0.18 to 0.43), and high/max ($V_{suction}/U_\infty$=0.64 to 1.01).

Figure 3.8 summarizes the results of these experiments in chart form. The horizontal axis of the chart indicates the location of the slot and the vertical denotes the general suction level, forming a 4x3 grid. At each grid location a *brief* topological description of the behavior of the junction flow is given; a full description of the effects of suction is presented below. In general, suction on the system can have four possible effects: 1) cause a segmentation of the necklace vortex system where the initial system breaks into two or more separate vortex systems; 2) stimulate the formation of a "braid" system, wherein a complicated interaction between two adjacent necklace vortices arises adjacent to the sides of the cylinder; 3) modify the strength and periodicity of the original

vortex system; 4) eliminate the advecting necklace vortex when it reaches the suction slot.

3.3.1.1 Baseline Case (No Suction)

Figure 3.9 is a sequence of hydrogen bubble visualizations illustrating the temporal behavior of the baseline unsteady laminar necklace vortex system (also described in §3.2). It is important to note the similarity of the bubble patterns of these visualizations to those of the necklace vortex system formed at a rectangular block-flat plate junction (figure 3.1). The similarity of these two figures supports the conjecture, made earlier in this manuscript, that general conclusions about the nature of unsteady laminar junction flows based on the PIV results obtained with the rectangular block-flat plate juncture should be valid for any body shape.

3.3.1.2 Corner Region Suction

When the slot is located in the corner region (10mm upstream of the cylinder) the effect of suction is rather limited. The only topological change to take place is the removal of the weakened necklace vortex when it reaches the slot (figure 3.10), which was observed at all suction rates, but no substantive effect on the upstream topology was observed. However, experiments showed that suction in the corner could have a slight effect on both the vortex formation/breakaway frequency of the system and the location of vortex formation.

For the baseline case, the vortices were observed to form 74mm upstream of the cylinder. Note that the determination of vortex formation location was done by observing the location at which the first indication of rotational motion is exhibited using particle visualizations of the flow on the symmetry plane. When suction was applied, this formation location gradually decreases to 68mm from the cylinder for the maximum suction case.

For the baseline (no suction) case, the frequency of vortex formation/breakaway was 0.45 Hz; this frequency gradually decreased to 0.43 Hz at the maximum suction rate ($V_{suction}/U_{\infty}=1.01$). The reason for this decrease is unclear. If a stability mechanism for periodicity is accepted (see below), this would suggest that the suction is somehow causing an increase in momentum thickness upstream of the cylinder in the region of vortex formation. Examining equations (5) and (6), it is evident that this thickening could happen if the magnitude of the reverse flow along the wall were increased, which could be a result of the suction in the corner region acting to bring more energetic fluid from the free stream into the reverse flow layer next to the wall, thus causing a slight thickening of the layer. But this would imply that the vortices should form further upstream, which they do not. The vortices form closer to the cylinder as suction is increased, suggesting a reduction in the magnitude of the reverse flow due to suction. So, something more subtle and more complicated must be taking place, such as a change in the shape of the impinging boundary layer profiles, such that θ might increase although reverse flow is reduced (which would normally entail a reduction in θ). Clearly, this

question requires further investigation since the present data can provide only a framework for speculation and cannot be used to draw clear conclusions.

3.3.1.3 Translation Region Suction

Locating the slot in the translation region creates a more complicated flow process as illustrated in the various pictures of figure 3.11 and is generally characterized by the segmenting of the unsteady necklace vortex system into two distinct necklace vortex systems; one upstream of the slot and one downstream.

At the two initial suction rates (within the low range of suction rates), the advecting primary vortex is weakened as it passes over the slot, such that a weakened vortex enters the corner region and amalgamates with a sustained corner vortex (figure 3.11 (a)), completing the standard breakaway regime behavior. Prior to passage over the slot, the diameter of the advecting necklace vortex is 7 and 6mm for nondimensional suction rates $V_{suction}/U_{\infty}$=0.08 and 0.1 respectively, but after passage over the slot the size of the vortex is respectively reduced to 5 and 3mm. At higher suction velocities (still within the low suction rates) the advecting primary vortex is removed by the suction when the vortex reaches the slot location (figure 3.11 (b)). Downstream of the suction slot a small-scale unsteady 2-vortex system develops (figure 3.11 (b)). The diameter of the larger unsteady vortex is 3-4mm, compared to the 8-9mm diameter of the uncontrolled necklace vortices, and forms at a distance of 14mm from the cylinder. This small unsteady system displays oscillating behavior (i.e. the vortices oscillate in space with some relatively small amplitude, §3.2). In addition to the behavior described above,

the formation point of the vortices moves downstream with increasing suction rates, from 69mm upstream of the cylinder in the baseline case to 60mm at the upper limit of the low suction rates ($V_{suction}/U_\infty=0.15$).

When moderate suction rates ($0.18\leq V_{suction}/U_\infty\leq 0.43$) are applied, the vortex system developing upstream of the slot compresses spatially and transitions to an unsteady 3-vortex system located exclusively upstream of the slot (figure 3.11 (c)). That is, the primary vortex no longer reaches the slot and is not removed by suction. For the initial moderate suction rates ($V_{suction}/U_\infty=0.18$), this upstream system displays amalgamating behavior, transforming toward oscillating behavior at the slightly higher suction rate $V_{suction}/U_\infty=0.22$ while the formation point of this unsteady system remains 60mm from the cylinder. Also at moderate suction rates, the 2-vortex system, which previously developed downstream of the slot stabilizes (figure 3.11 (c)). The larger of the two steady vortices is located 14mm upstream of the cylinder and remains the same size (3-4mm in diameter) as for the previous, low suction rate, cases. As suction rates are increased (within the moderate range), the vortices upstream of the slot first stabilize (figure 3.11 (c)), and then vanish, such that at $V_{suction}/U_\infty=0.43$ no vortices appear upstream of the cylinder in the symmetry plane region; however, there is a reformation of the necklace vortex legs around the side of the cylinder (see below). Downstream of the slot the steady vortex system remains essentially unchanged (located 13mm upstream of the cylinder with a diameter of 4mm) at the highest moderate suction rates.

For the high/max suction rates the upstream vortex system develops as indicated in figure 3.11 (e). The upstream vortex system is steady, but is no longer contiguous.

That is, the upstream vortex no longer forms an unbroken U-shape, but the base of the "U" shape has been entirely eliminated in a region approximately spanning the width of the slot (as illustrated by the lack of hydrogen bubble concentration in the figure 3.11 (d) near the slot). Outboard and upstream of the slot the legs of the necklace vortices form, extend downstream in the usual fashion, and are steady (i.e. they do not oscillate). The small steady vortex system immediately adjacent to the cylinder is gradually weakened as suction increases, becoming a steady 1-vortex system located 9mm from the cylinder with a diameter of 3mm at the highest suction rate.

3.3.1.4 Formation Region Suction

The third slot location examined was in the formation region, where the necklace vortices form (slot located 88.5mm upstream of the cylinder). In this case, the prominent feature of the controlled cases is the development of a "braid" structure (shown in figures 3.12 through 3.18).

As suction is applied (in the low range), the formation point of the vortices and the formation/breakaway frequency change from 70mm and 0.45 Hz for the baseline case to 50mm and 0.52 Hz for the $V_{suction}/U_{\infty}$=0.15 case; the corresponding diameter of the advecting vortex decreases from 8-9mm in the baseline case to 7mm. In this low suction rate regime the flow topology is characterized by the *initiation* of a "braid" formation as revealed in figure 3.12 (a) and the time sequence of figure 3.13. Figure 3.13 (a) shows a newly formed necklace vortex breaking away from the formation region; however, note that the action of the suction has affected the shape of the advecting vortex such that an

inflection point (termed a "kink") develops in the conventional "U"-shape of the vortex, at a point adjacent to the cylinder and approximately 45° from the symmetry plane. Moving forward in time, figure 3.13 (b) and (c) show that as the vortex advects downstream, the kink in the vortex amplifies. Note that through this entire process the deformed vortex remains a distinct structure, separate from any other necklace vortex. This vortex kink formation is very repeatable, occurring periodically in conjunction with the vortex system formation/breakaway behavior.

At moderate suction rates, the formation point of the vortices gradually moves further downstream (e.g. to 40mm from the slot for the $V_{suction}/U_{\infty}$=0.43 case), but the formation/breakaway frequency remains relatively constant (at 0.52 to 0.53 Hz throughout the moderate suction range). The diameter of the advecting vortex also decreases to 6mm at $V_{suction}/U_{\infty}$=0.43. At this moderate suction rate, the flow topology changes to that of the fully-developed "braid" system, shown schematically in figure 3.12 (b), which is characterized by an advecting vortex intertwined (or "braided") with a steady vortex. Downstream of the slot, on the symmetry plane, an unsteady necklace vortex system in the breakaway regime develops. Around the sides of the cylinder these unsteady vortices fully intertwine with a steady vortex (which is part of a steady 2, possibly 3-vortex system) which originates from the outboard edges of the suction slot; this braiding is clearly shown in figure 3.14 by the hydrogen bubble-marked vortex lines.

In the high suction rate regime, the intertwining of the vortices ceases and the junction flow becomes characterized by a steady, 3-vortex system originating at the outboard edges of the suction slot, and an unsteady vortex system between the slot and

the cylinder (illustrated in figure 3.12 (c)). The behavior of the unsteady system near the cylinder is initially that of a breakaway system, which begins to demonstrate amalgamating behavior at the highest suction rates. At the maximum suction rate, the frequency of the unsteady system drops slightly to 0.51 Hz and the diameter of the unsteady vortices is reduced to 5mm.

The braiding phenomenon described above is especially interesting, particularly because it displays discrete vortex-vortex interactions as well as surface interactions reminiscent of "bursts" observed in a turbulent boundary, and therefore is described in more detail below.

Figures 3.15 and 3.16 show more detailed time sequences of the temporal details and periodicity of the flow during this braiding process. Figure 3.15 is a magnified view of the initial intertwining of the vortices and figure 3.16 is a more general view illustrating the downstream flow behavior. As time progresses, the unsteady vortex develops in the usual breakaway manner, moving towards the cylinder and into the corner region. During this process, the point where the unsteady and steady vortices meet (termed the "interaction point", see figure 3.14) moves downstream and undergoes a rather complicated development and interaction with the surface (described below). The events described above are periodic, occurring in conjunction with the periodic vortex formation process.

As the interaction point moves downstream, the two vortices interact with each other as illustrated in figure 3.16, ultimately resulting in a breakdown of the vortices as illustrated in figure 3.16 and figure 3.17. The initial stage of the breakdown is shown in

figure 3.16 at t=3.0s as a Z-shaped hydrogen bubble pattern. Figure 3.17 is a temporal sequence showing the initiation of the breakdown (t=1.0s) and following the breakdown behavior further downstream than is illustrated in figure 3.16. Note, the term "breakdown" refers to the point at which the necklace vortex core, as marked by the hydrogen bubbles, starts to display a complicated turbulent-like pattern.

In addition to the interactions between vortices, there exists a complicated interaction of the two vortices with the surface, culminating with a pair of sharp localized eruptions of wall fluid reminiscent of a turbulent boundary layer "burst". Figure 3.18 is a hydrogen bubble visualization of this process using two separate hydrogen bubble wires. One wire was located upstream of the cylinder (out of the field of view), marking the vortex cores, and a second wire was located on the flat plate surface (at the cylinder center line) to mark the surface fluid behavior. From t=0.0 to 0.5s the surface flow is characterized by a ridge of erupting fluid caused by an interaction of the downstream extensions of the intertwining vortices with the surface (see Greco, 1990 for a more detailed description of this phenomenon). As the interaction point moves and develops downstream (t=1.0 and 1.33s), a pair of localized eruptions of surface fluid develop. Figure 3.19 illustrates the eruption process described above using dual view hydrogen bubble visualizations. The top halves of the pictures are oblique views of the surface flow, visualized using only the surface wire. The bottom halves of the pictures are more magnified shallow angle oblique views (essentially side views) of the flow. An erupting ridge of fluid is clearly seen at t=0.0 and 0.5s. The developing eruption is illustrated from

t=0.83 to 1.49s, with the eruption essentially complete by t=1.49s. The lower side views illustrate the rapid development of these violent eruptions from the initial ridge of fluid.

The repeatability of the events described above makes this phenomenon a possible test-bed for the study of discrete vortex-vortex interactions and their associated wall interactions, which can be of use in understanding fundamental processes at work in a turbulent boundary layer. In addition, the fact that these events are embedded in an otherwise laminar flow allow the examination of these events in a relatively "clean" setting, free of extraneous influences present in a fully turbulent boundary layer.

3.3.1.5 Formation+ Region Suction

When the slot was located in the formation+ region (150mm upstream of the cylinder) no **drastic** topological change, like those described above, was observed when suction was implemented. At both the low and moderate suction rates, the only effect of suction was to alter the periodicity and physical scale of the baseline unsteady, breakaway necklace vortex system. The effect took the form of an increase in formation/breakaway frequency from the baseline case with increased suction, with the frequency increasing in direct proportion to suction velocity from 0.47 Hz for the baseline case to 0.57 Hz at $V_{suction}/U_{\infty}=0.43$. The physical scale of the system decreased with increasing suction rates, with the formation point moving from 68mm upstream of the cylinder for the baseline to 46mm at $V_{suction}/U_{\infty}=0.43$. The diameter of the vortices also decreased from 8-9mm for the baseline to 6-7mm at $V_{suction}/U_{\infty}=0.43$.

When suction was increased to the high/max rates ($V_{suction}/U_\infty$=0.64-1.01,) the frequency of the unsteady, breakaway system increased marginally to 0.58 Hz for the maximum suction rate, with the formation point decreasing to 38mm and the diameter of the vortices decreasing to 5-6mm. However, a single, *steady* vortex system forms, emanating from the outboard edges of the slot (figure 3.20).

3.3.1.6 Suction in Unobstructed Boundary Layer

It was mentioned several times above that the outboard edges of the suction slot were sources of vorticity, particularly at the higher suction rates. To examine this vorticity generation behavior, a limited study of the edge effects of the suction slot was performed with an unobstructed boundary layer. Figure 3.21 (a) is a combined oblique and end-view hydrogen bubble visualization of the induced flow downstream of the suction slot, with U_∞=8.26 cm/s and $V_{suction}/U_\infty$=1.01; the induced streamwise vorticity is indicated by the concentration of bubbles in the end-view. Since the hydrogen bubble wire was pulsed at a fixed frequency, the addition of streamwise momentum to the boundary layer by the suction is evidenced by the deformation of the bubble time-lines downstream of the slot. An end-view schematic showing the hypothesized mechanism for streamwise vorticity generation is shown in figure 3.21 (b), which indicates that a transverse shear layer created by the suction is the source of streamwise vorticity.

3.3.1.7 Curved Suction Slot

As mentioned in the previous sections, the outboard edges of the suction slot appeared to facilitate the generation of necklace vortices at higher suction rates. In an attempt to eliminate this generation process and to examine a broader suction slot, a curved suction slot was constructed, with the curvature of the slot generally matched to the curvature of the necklace vortices in the formation region (figure 3.22). Due to time constraints, only a preliminary examination of the effectiveness of the curved slot on an unsteady laminar necklace vortex system was possible, with the apex of the slot located 33mm from the 8.8cm diameter cylinder (in the translation region); for this study, the cylinder was located 81.28cm from the leading edge of the plate and the suction rate set to $V_{suction}/U_{\infty}=0.65$. It was determined that the curved slot had an effect of the flow even at zero suction velocity, acting to some extent as a passive control device. It was observed that for the baseline case, an unsteady, laminar necklace vortex system develops which is segmented into (1) a 2-vortex unsteady/steady system (simultaneously exhibiting behavior of both an oscillating and steady system) upstream of the slot, and (2) a single steady vortex downstream of the slot. Figure 3.22 shows the schematics of this phenomenon. Detailed visualizations of the flow in the vicinity of the curved slot showed that there was a down-flow of fluid into the slot near the symmetry plane, with a corresponding up-flow of fluid out of the slot outboard of the symmetry plane. This fluid transport through the slot is presumably in response to the streamwise and lateral pressure gradients imposed by the cylinder. Near the symmetry plane, the increasing streamwise pressure forces boundary layer fluid into the slot. The lateral pressure gradient then

induces this fluid to flow around the sides of the cylinder (inside of the slot), until the free stream pressure decreases sufficiently to allow the fluid to leave the slot and re-join the boundary layer flow. So in essence, without the application of suction the curved slot creates a region of wall-region fluid transport into the slot near the symmetry plane and a region of reintroduction of fluid around the sides of the cylinder.

When suction was applied ($V_{suction}/U_{\infty}=0.65$) the steady/unsteady system upstream of the slot and the associated vortex legs appear to be removed (figure 3.22), but the single steady vortex system near the cylinder remains.

3.3.2 *Surface Pulsations*

As mentioned previously, the junction flows under study consist of a boundary layer impinging a wall-mounted bluff body. Since boundary layers can be susceptible to perturbations (i.e. under proper conditions boundary layers amplify applied perturbations), experiments were performed to assess the efficacy of externally applied perturbations as a method of laminar flow control.

3.3.2.1 Stability Considerations

Employing the velocity profile results described in §3.2.4 for a rectangular block, the stability characteristics of the impinging shear layer were examined to assess a possible relationship to the periodic breakaway frequency of the necklace vortices. Figure 3.6 suggests the most upstream velocity profile can be approximated as an inflectional mixing-layer profile described by a hyperbolic tangent function. For this

shape profile, linear stability theory suggests that the greatest amplification of disturbances occurs for a non-dimensional frequency $\omega_s \approx 0.21$ (Monkewitz and Huerre, 1982), where

$$\omega_s = \frac{4\pi f\theta}{\overline{U}}, \tag{5}$$

and θ is momentum thickness, f is frequency, and $\overline{U}$ is the average velocity of the upper and lower free stream velocities (U_{max} and U_{min} respectively) in the shear mixing layer. For the present case, θ was determined as $\theta \approx 1.9$mm by integration of a typical velocity profile at x/W=0.01 using the standard definition,

$$\theta = \int_0^{\delta} \frac{|u|}{U}\left(1 - \frac{u}{U}\right)dy \tag{6}$$

(note, the |u| term accounts for the effects of reverse flow). $\overline{U}$ was approximated by assuming U_{max} to be equal to the local free-stream velocity U (in this case $U \approx 49$ mm s^{-1} at x/W=0.01) and $U_{min}=0$. These values indicate a frequency of maximum amplification of $f_{stability}=0.22$ Hz, which is very close to the measured frequency of vortex formation and breakaway of $f_{experimental}=0.2$ Hz.

Preliminary comparison of the measured frequencies for other breakaway cases (at different Reynolds numbers) suggests a similar consistency with predicted stability frequencies as illustrated in figure 3.23 (open symbols). Since PIV data was not available to determine θ and U_{max} (at x/W=0.01) for the other cases, θ was approximated using the *Blasius* formula for a laminar boundary layer and U_{max} was determined using an analytical solution for the 2-D stagnation flow (in the free-stream) around a rectangular

body (Panton, 1984). While calculating θ via the Blasius equation (and hence for a Blasius boundary layer profile) is an approximation of the true momentum thickness (of a hyperbolic tangent shaped profile), it would appear acceptable since comparison of a Blasius value with the θ measured from the PIV results indicates a variance of only 5%.

3.3.2.2 Application of Control

To further examine the possibility of the impinging shear layer instability as the mechanism of the necklace formation/breakaway frequency and examine this mechanism as a possible means to control the flow, the response of the laminar unsteady necklace vortex system to applied perturbations was examined for the circular cylinder-flat plate junction. An 8.8cm diameter (D) cylinder was placed at L/D=12.7 downstream of the plate leading edge with U_∞=8.26 cm/s, yielding $Re_L=9.2x10^4$, and Re_{δ^*}=521.6 (calculated as described in chapter 2). External perturbations were applied by sinusoidally varying the injection/suction through the transverse surface slot in the flat plate (63.5mm transverse by 2mm in the streamwise direction) over a range of $|V_{p,max}|$ from 0.0 to 2.5 cm/s, where $|V_{p,max}|$ is the peak injection/suction velocity over an injection/suction cycle. It was established that within a narrow frequency range (bracketing the natural, unperturbed frequency of 0.48 Hz) the application of local sinusoidal forcing *upstream of the attachment line* can cause the vortex formation/breakaway frequency to follow the forcing frequency (i.e. "lock on" to the forcing frequency). However, application of this same type of forcing *downstream of the formation region* (within the translation region,

approximately 0.5 diameters upstream of the cylinder) had no effect on vortex formation/breakaway frequency.

Figure 3.24 shows a map of "lock-on" response with the slot located 2.47 diameters upstream of the cylinder, which was upstream of the boundary layer attachment point. Varying both the frequency and amplitude of the applied perturbations, the map of the region exhibiting a "lock-on" response was established. The data plotted is non-dimensional amplitude ($|V_{p,max}|/U_\infty$) vs. non-dimensional frequency (f_p/f_N), where U_∞ is free-stream velocity, f_p is the frequency of the applied perturbations, and f_N is the natural (unperturbed) formation/breakaway frequency. Open symbols denote points where "lock-on" behavior was observed and closed symbols represent the bracketing case where "lock-on" behavior ceases. Note that modification of the vortex formation frequency can be influenced by as much as 30%-50% for selected injection/suction magnitudes.

In addition, the slot was used to reduce θ in the symmetry plane region by the application of local, constant rate, surface suction upstream of the formation region. Quantification of the reduction in θ was not performed, but hydrogen bubble visualization did reveal an *increase* in the formation/breakaway frequency as the suction was increased (which presumably reduced θ) as equation (5) suggests (see §3.3.1.5).

The possibility that the formation/breakaway frequency of the vortex system is influenced by downstream conditions of the flow was also examined by comparing the frequency of the vortex formation/breakaway process for the unaltered block with the block retrofitted with a Thwaites-type flap at the trailing edge. To create a Thwaites flap, a 3mm thick flat plate 3.5 block widths long was placed behind the block on the

symmetry plane, which essentially negated the Kármán shedding behavior of the block. With the flap in place no change in the necklace formation frequency was observed, suggesting no connection between the necklace vortex formation frequency and downstream conditions. This was also observed in the experiments of Baker (1979).

Taken collectively, these results suggest that the instability of the impinging shear layer is the physical mechanism which determines the frequency of the unsteady necklace vortex system, which can be exploited as a means to control the formation/breakaway frequency over a narrow range of frequencies bracketing the natural (unperturbed) frequency. Also, these results indicate that downstream influences appear to play no role in the periodicity of unsteady necklace vortex behavior.

During the course of the "lock-on" study described above, another interesting control possibility was observed (if intentionally transitioning the laminar flow can be considered control). It was determined that particular combinations of perturbation frequency and amplitude would artificially cause transition of the flow to a turbulent-like behavior as illustrated in figure 3.25. For perturbation frequencies and amplitudes above and below these values the necklace vortex system was unresponsive and continued to develop and behave normally.

3.3.3 *Passive Control*

3.3.3.1 Fillet

The fillet of Devenport *et al.* (1992) was the first passive control method looked at, to examine the effect a fillet has on the laminar junction flow structure. The

visualizations of Kubendran *et al.* (1988) showed no **clear** indication of the presence of necklace vortices in the wake region of a laminar junction flow with a fillet, but the nature of the visualization technique and its implementation leaves the question less than resolved (smoke flow visualization was performed with a single smoke wire located upstream of the body). Figure 3.26 shows the hydrogen bubble visualizations for the cylinder-fillet body located with the tip of the fillet 116.25cm from the leading edge of the flat plate and a free-stream velocity of 8.26 cm/s. In the top-left picture the bubble wire is located near the tip of the fillet, very close to the plate surface. The bubble pattern shows the formation of a steady necklace vortex, originating at the approximate mid-point of the fillet. In the bottom-right picture, the bubble wire, which has been moved to the side of the fillet to more clearly mark the presence of the steady necklace vortex described above, shows a possible second steady vortex outboard of the first vortex. So, although the fillet does effectively counter unsteady laminar necklace vortex formation in the symmetry plane region, steady necklace vortices still form around the sides of the fillet; although no quantification was performed, the bubble patterns presented in figure 3.26 suggest that the diameter of the modified steady vortices are roughly the same as for the baseline (unsteady) case. However, recall that the fillet tested for this study was modeled after the fillet used by Devenport *et al.* (1992), which was designed for modification of a *turbulent* junction flow, not *laminar*. Since the baseline (no suction) laminar vortices observed in this study were found to form 20-30mm upstream of the location the turbulent vortices form (see chapter 4), it is reasonable to conjecture that for *optimal* laminar flow control a fillet must extend further upstream than for turbulent flow control;

this is not to say, however, that extending the fillet upstream would eliminate all vortex formation.

3.3.3.2 Control Rings

A novel control method was devised for this study in the form of control rings (§2.2.3). Due to time constraints only one ring size (W=4cm) at one height (h=12mm) was examined in detail, with the 8.8cm diameter cylinder located 92.9cm downstream of the plate leading edge and the free-stream velocity set to U_∞=8.26 cm/s. The results shown in figures 3.27 and 3.28 are symmetry plane hydrogen bubble visualizations and schematic characterizations respectively, and illustrate the effect of the control ring on an unsteady laminar necklace vortex system. Figure 3.27 (a) is a time sequence of the flow upstream of the control ring and shows the existence of an unsteady necklace vortex system (shown schematically in figure 3.28) in the amalgamating regime (see §3.2), with the diameter of these vortices, just after formation, equal to the comparable vortex diameter of 8-9mm for the uncontrolled case. Figures 3.27 (b)-(e) are a series of visualizations of the flow in the vicinity of the ring obtained by varying the height of the bubble wire. Figure 3.27 (b) reveals the existence of a small-scale steady 2-vortex system on the top surface of the ring, with the diameter of the larger vortex equal to 3.9mm. Figures (c) and (d) show a region of recirculation on the bottom tip of the ring and a single small-scale steady vortex (diameter equal to 4.9mm) in the bottom corner of the ring cylinder junction. Figure 3.27 (e) shows a small-scale steady 2-vortex system in the

corner of the cylinder-plate junction, with the diameter of the larger of the two vortices equal to 5.2mm.

These results indicate that control rings can be used as a passive alternative to spatially-limited suction, since they were found to effectively modify the topology and behavior of an unsteady laminar necklace vortex system; the effects are similar to the behavior observed with spatially limited suction (i.e. the separation of the original unsteady vortex system into several smaller-scale unsteady and steady systems). A possible disadvantage of the control ring approach is the introduction of a second necklace vortex system (albeit of a smaller scale) on the top surface of the control ring. However, the geometric simplicity of this control method may make it more attractive for retrofit applications than a fillet.

3.3.3.3 Flat Plate Geometric Modifications

Another passive method of laminar junction flow control examined was a type of "dillet", namely a symmetric depression in the approach surface of the flat plate, just adjacent to the cylinder. This was accomplished by using the clay inserts described in §2.2.3, which were inserted into the circular cut-out at the 90cm location on the flat plate (figure 2.3). It is important to note the difference between the curved depression examined here and a "dillet" of the type described by Bushnell (1990), which is a mirror image of a fillet. A 5.8cm diameter cylinder was then located 23mm downstream of the curved depression molded into the clay. The schematic of figure 3.29 shows how a normally unsteady necklace vortex system in the breakaway regime is modified. The

curved depression forms a kind of "nest" where a single steady necklace vortex forms and resides, while upstream of the depression a steady 2-vortex system is formed. Downstream of the depression a single, small-scale, steady necklace vortex forms immediately next to the cylinder.

The results described above suggest that relatively simple geometric modifications of the approach surface to a junction can effectively modify the laminar flow behavior in a manner similar to that observed for several suction cases (i.e. the stabilization of the unsteady system), without resorting to the more drastic modifications of a fillet or "dillet".

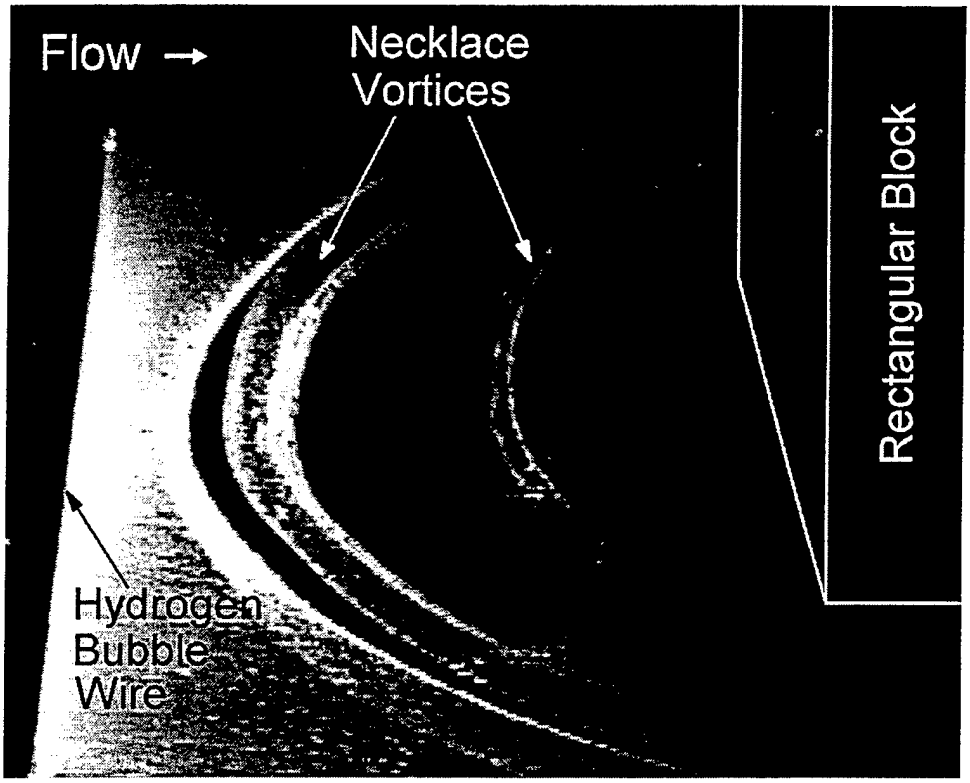

Figure 3.1 Hydrogen bubble visualization of an unsteady, laminar necklace vortex system.

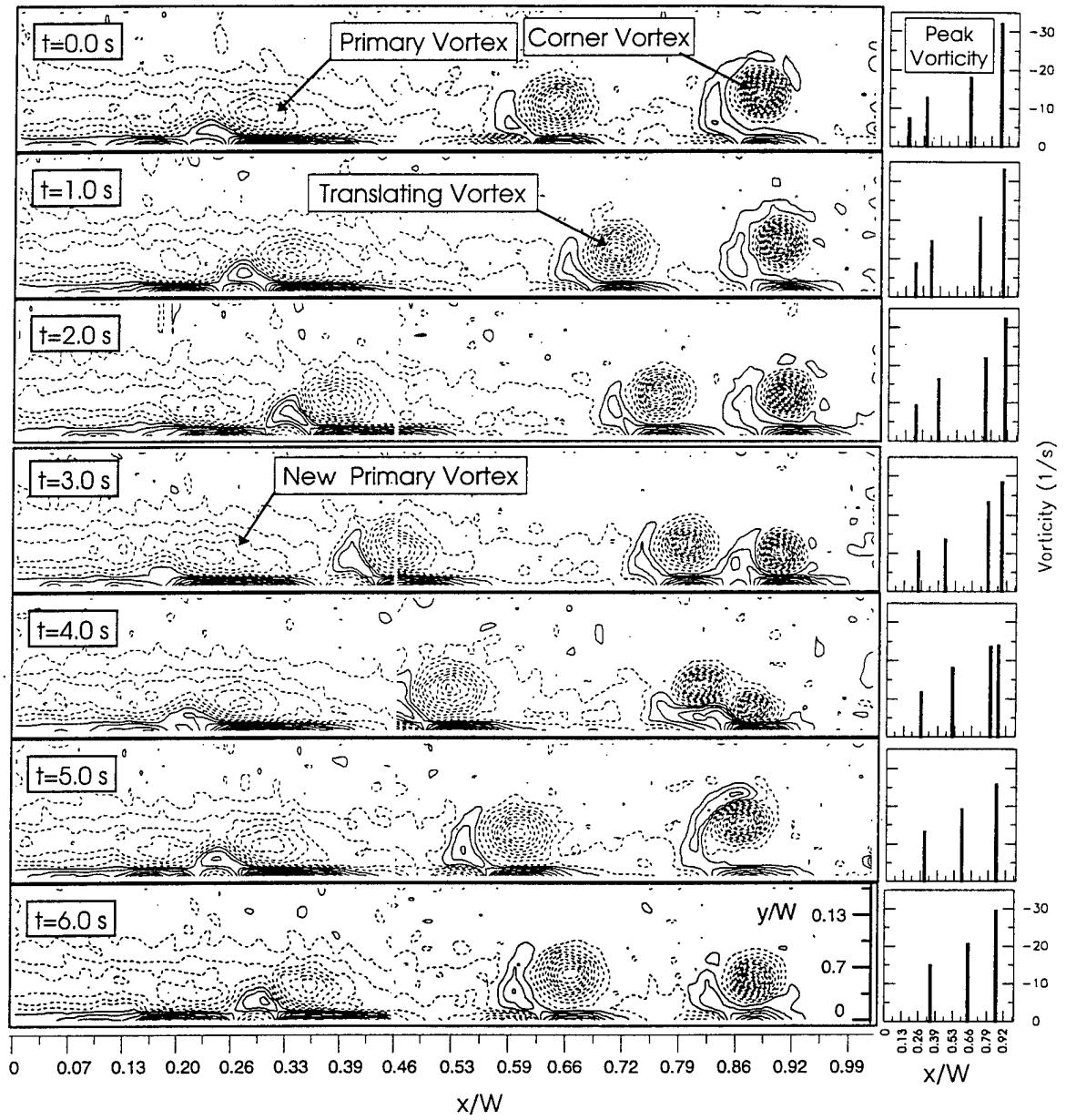

Figure 3.2 Vorticity contour and peak vorticity time sequence. Dashed lines indicate negative vorticity, solid lines indicate positive vorticity. Contour levels range from $\pm 1\ s^{-1}$ to $\pm 33\ s^{-1}$ in intervals of 2. U_∞=50.4 mm/s, $Re_L=3x10^4$, and $Re_{\delta^*}=298$, where Re_L and Re_{δ^*} are calculated for an equivalent, unobstructed, laminar boundary layer at the block location L.

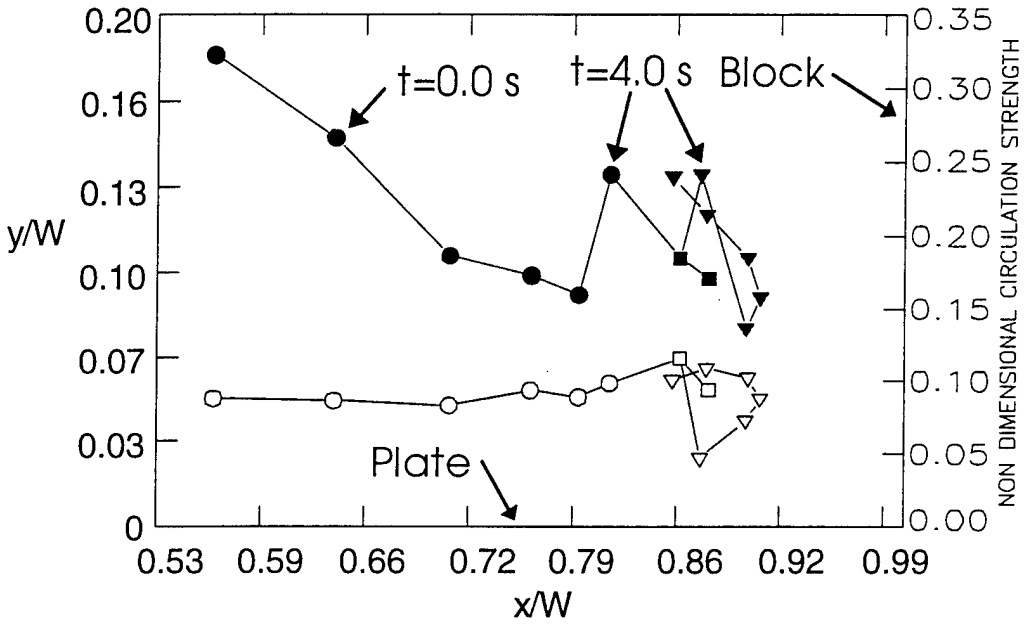

Figure 3.3 Vortex trajectory (open symbols) and non-dimensional strength (Γ_v/Γ_e, closed symbols), where Γ_e is the time integral of vorticity flux passing across the left edge of the field of view over one cycle. Plotted data corresponds to figure 3.2. Circles represent the impinging translating vortex, triangles represent the corner vortex, and squares are the new corner vortex after amalgamation. U_∞=50.4 mm/s, $Re_L=3x10^4$, and $Re_{\delta*}$=298, where Re_L and $Re_{\delta*}$ are calculated for an equivalent, unobstructed, laminar boundary layer at the block location L.

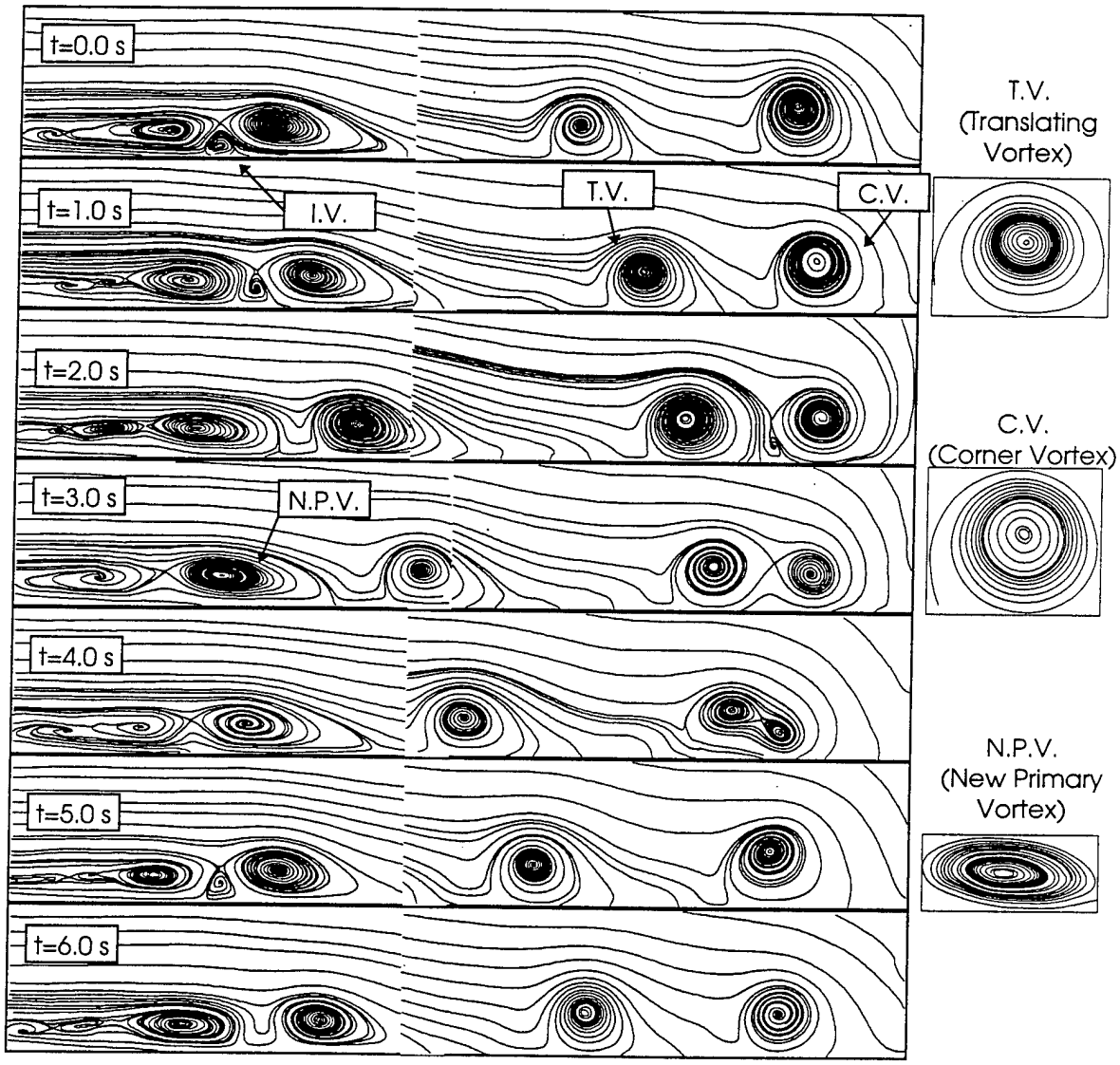

Figure 3.4 Instantaneous streamline plots corresponding to figure 3.2. The isolated patterns on the right are expanded views of the labeled vortices in the overall temporal sequence.

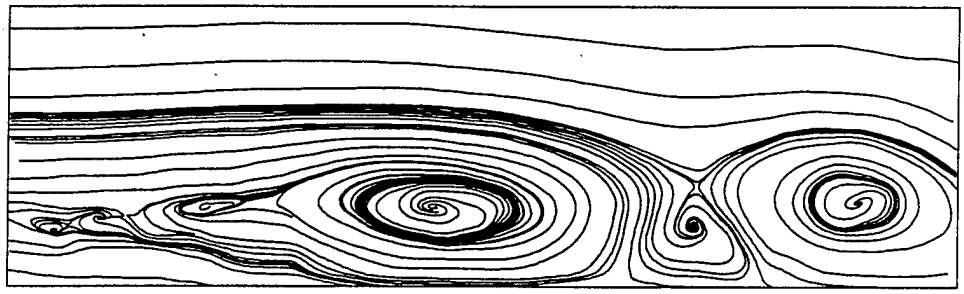

Figure 3.5 Streamline plot of magnified case illustrating limit cycles and the modified feeding topology of the induced counter-rotating vortex.

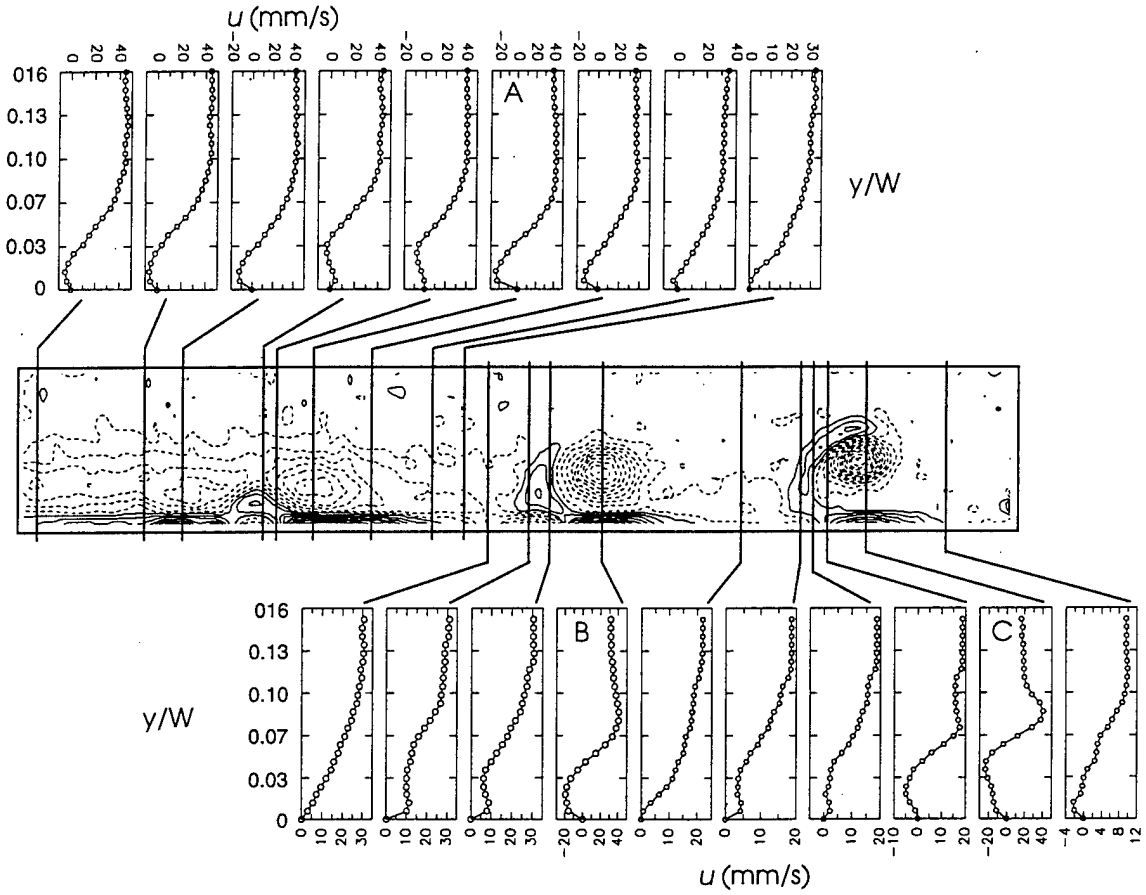

Figure 3.6 Selected *u*-velocity profiles for t=5.0 s in figure 3.2.

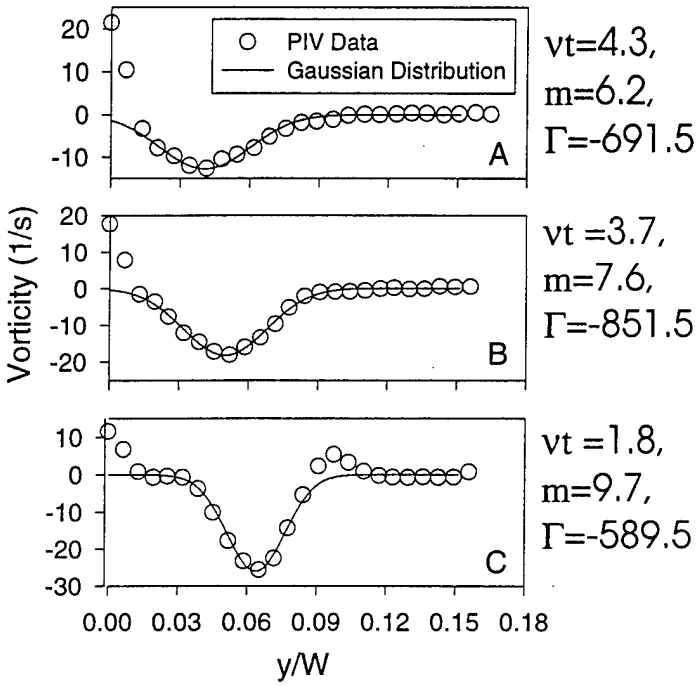

$$Vorticity = \frac{\Gamma}{4\pi(\nu t)} e^{\frac{\left(y/W - m\right)^2}{4\nu t}}$$ Gaussian Distribution

Figure 3.7 Wall-normal vorticity distributions (A, B, and C) corresponding to the *u*-velocity profiles labeled A, B, and C respectively of figure 3.6.

	Corner Region	Translation Region	Formation region	Formation Region +
Low $0.0 \le V_{suction}/U_\infty \le 0.15$	• Corner vortex removed in the vicinity of the slot.	• Advecting primary vortex either weakened or removed by passage over the suction slot. • Unsteady 2-vortex system develops between the suction slot and the cylinder for the higher suction rates.	• Unsteady "braid" system begins to develop, with the advecting necklace vortices developing an inflectional shape.	• Increase of breakaway frequency from the natural.
Moderate $0.18 \le V_{suction}/U_\infty \le 0.43$	• Corner vortex removed in the vicinity of the slot.	• Unsteady or steady, contiguous 3 (possibly 4) vortex system present upstream of the slot. • Steady 2 vortex system (possibly 3)present downstream of the slot.	• Unsteady "braid" system, with adjacent necklace vortices fully intertwined, fully developed.	• Further increase of breakaway frequency from the low suction rates.
High/Max $0.64 \le V_{suction}/U_\infty \le 1.01$	• Corner vortex removed in the vicinity of the slot. • Further slight decrease of breakaway frequency from the moderate suction rates.	• Vortex system directly upstream of the slot eliminated. • Steady 2 (possibly 3) vortex system develops outboard and upstream of the slot. • Steady 2 vortex system present downstream of the slot.	• Steady 3 vortex system originating from the outboard edges of the slot. • Unsteady vortex system develops downstream of the slot.	• Single steady vortex originating from the outboard edges of the slot. • Frequency of breakaway increased further from the moderate suction rates. • Unsteady breakaway system present downstream of the slot.

Figure 3.8 Chart summarizing the effect of constant rate suction on an unsteady laminar necklace vortex system.

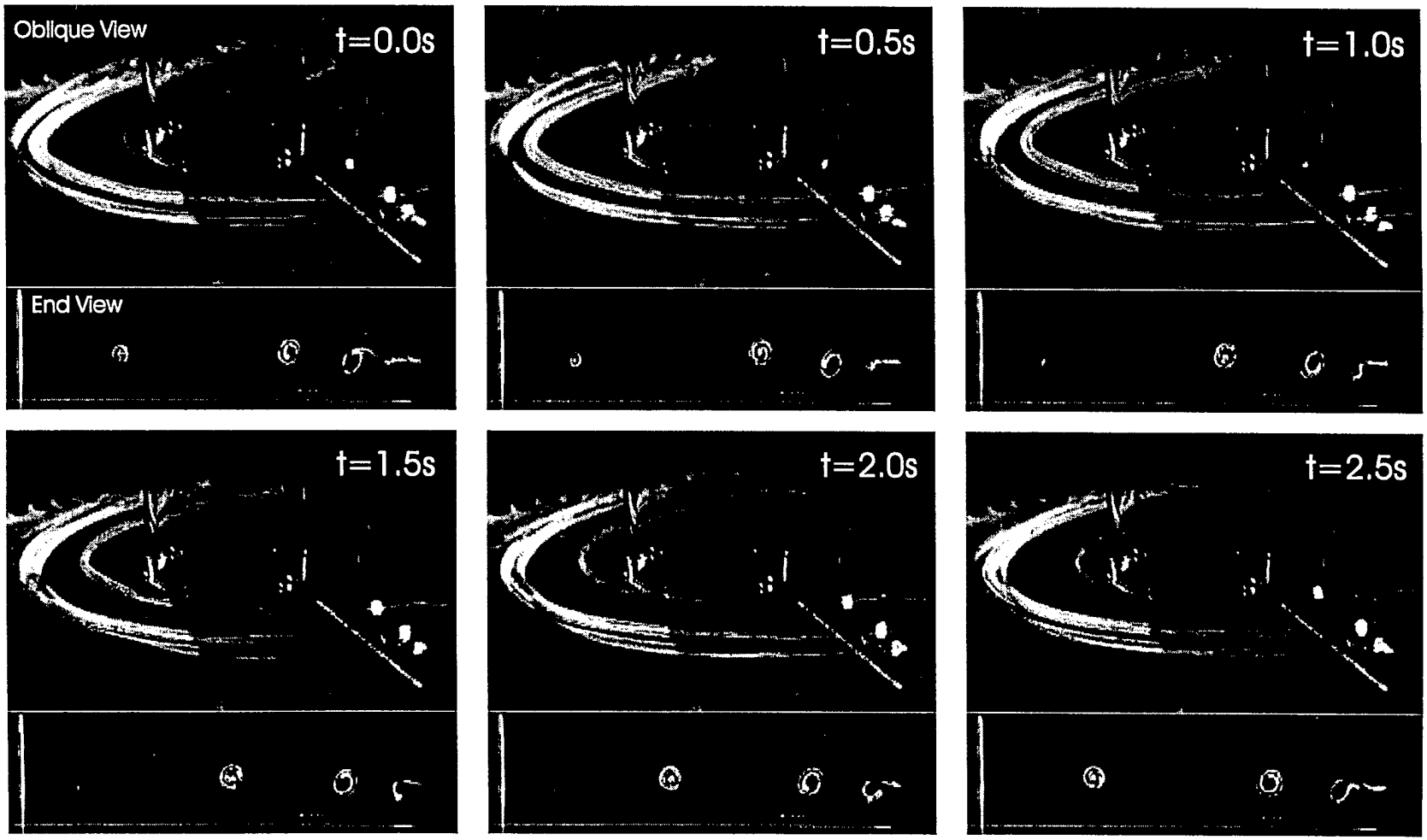

Figure 3.9 Temporal hydrogen bubble visualization sequence illustrating the baseline (no suction) case used for the laminar junction flow control experiments. U_∞=.8.26 cm/s, Re_L=8.6x10^4, and Re_{δ^*}=506, where Re_L and Re_{δ^*} are calculated for an equivalent, unobstructed, laminar boundary layer at the cylinder location L.

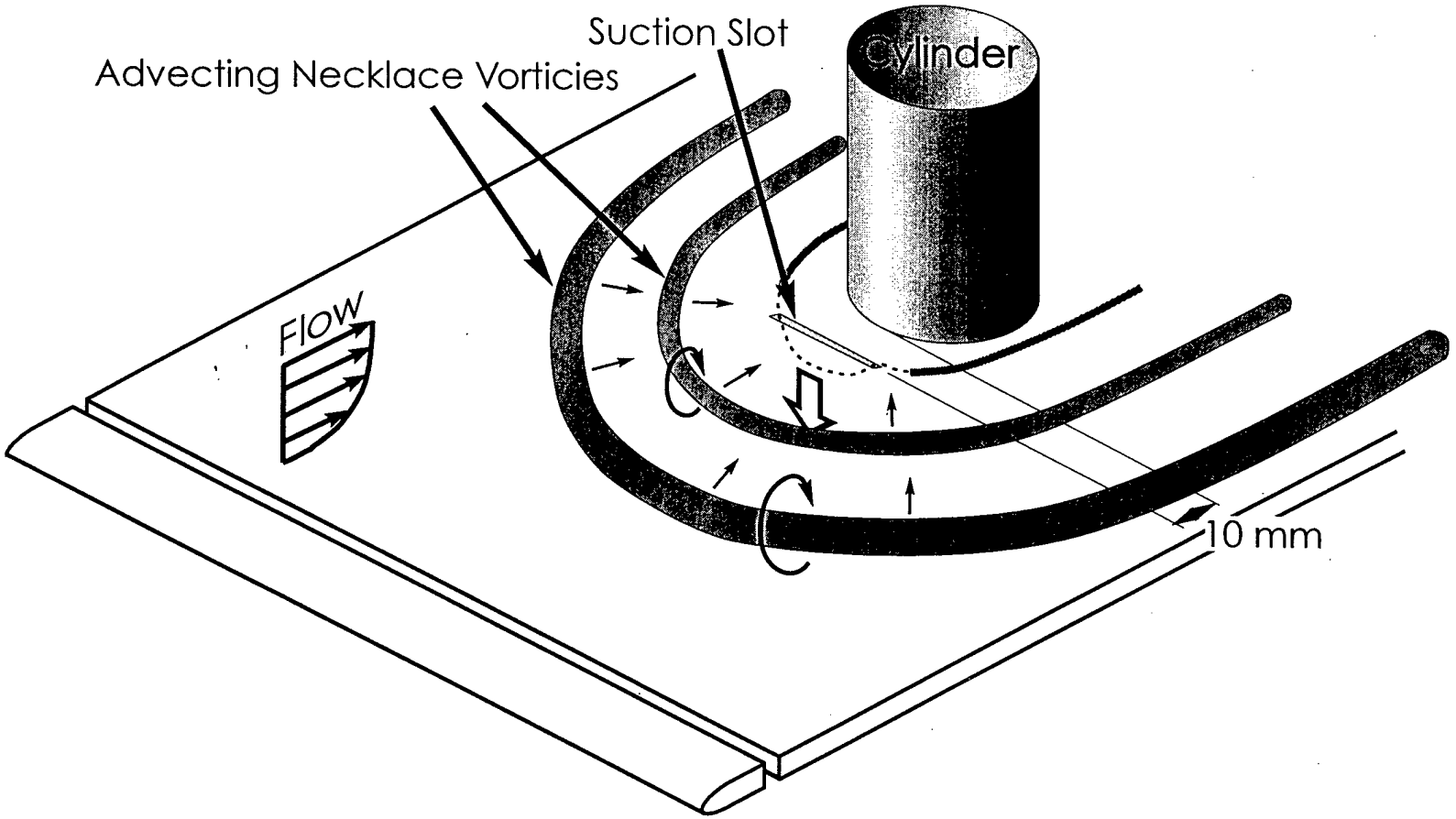

Figure 3.10 Schematic of the effect of constant rate suction for a slot located in the corner region at all suction rates $V_{suction} = (8 \rightarrow 101\% \ U_{\infty})$.

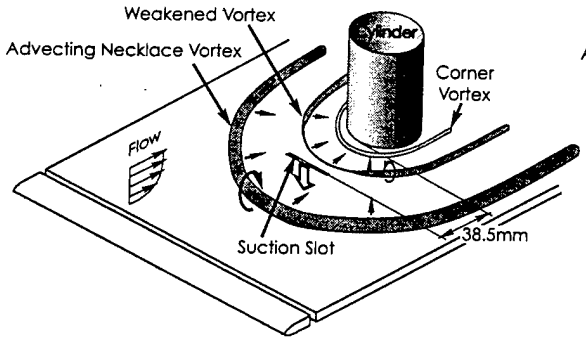

a) Low Suction (8→10% U_∞).

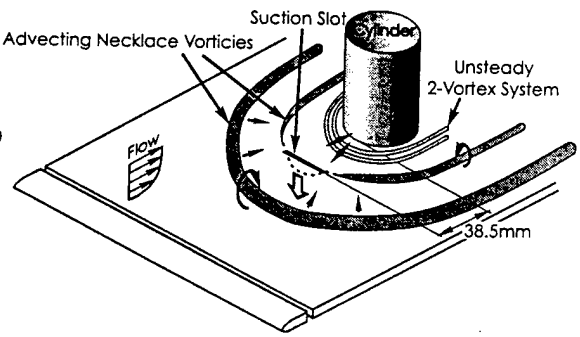

b) Low Suction (13→15% U_∞).

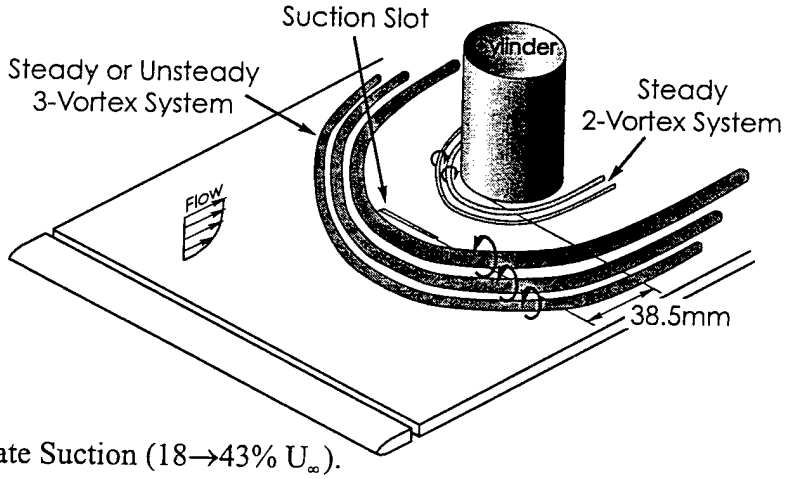

c) Moderate Suction (18→43% U_∞).

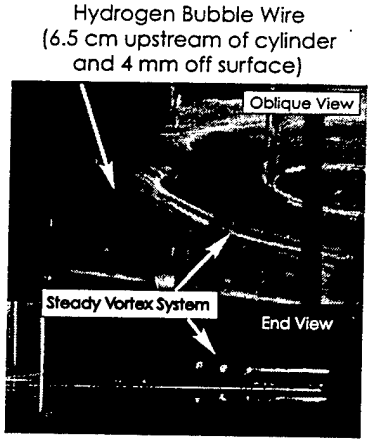

d) Hydrogen bubble visualization of the steady necklace vortices formed at the outboard edges of the slot at high/max suction.

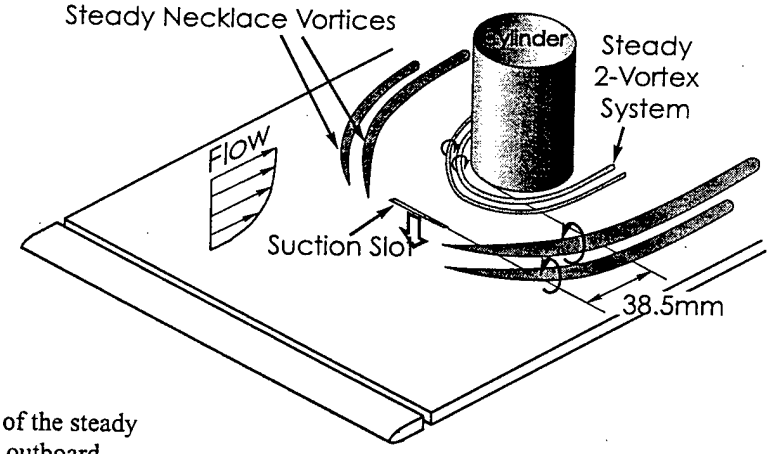

e) High/Max Suction (64→101% U_∞).

Figure 3.11 Schematics and visualizations illustrating the effect of suction on an unsteady laminar necklace vortex system; slot located in the *translation* region.

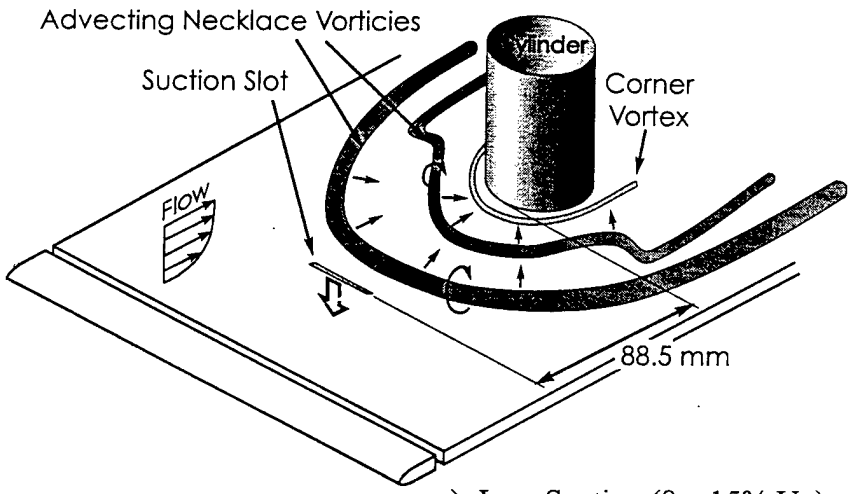

a) Low Suction (8→15% U_∞).

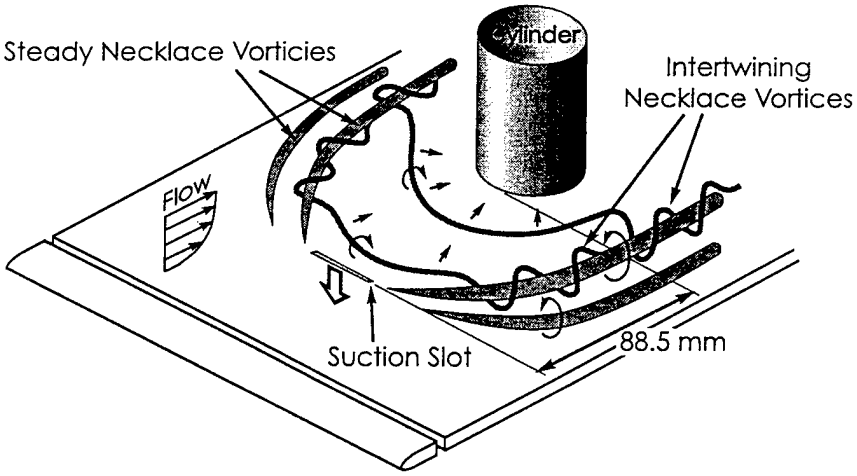

b) Moderate Suction (18→43% U_∞).

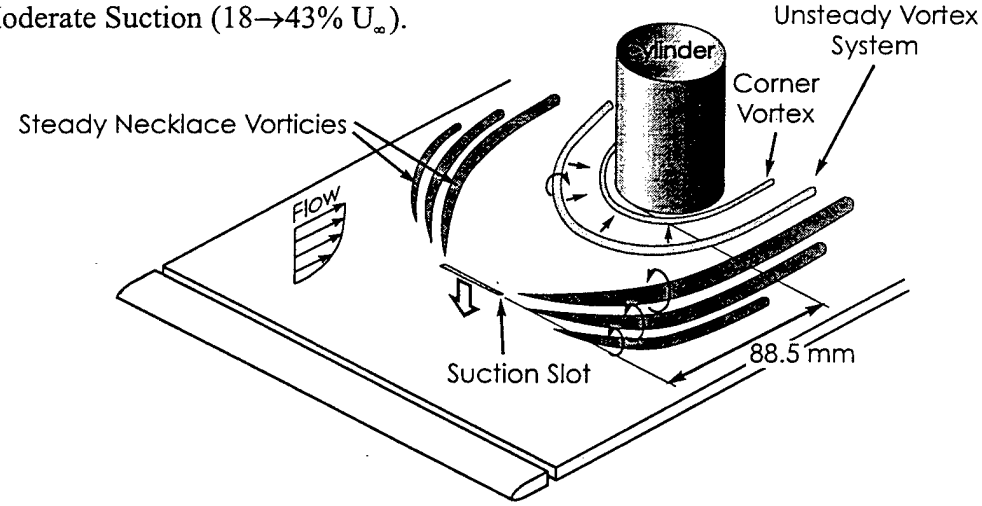

c) High/Max Suction (64→101% U_∞).

Figure 3.12 Schematics and visualizations illustrating the effect of suction on an unsteady laminar necklace vortex system; slot located in the *formation* region.

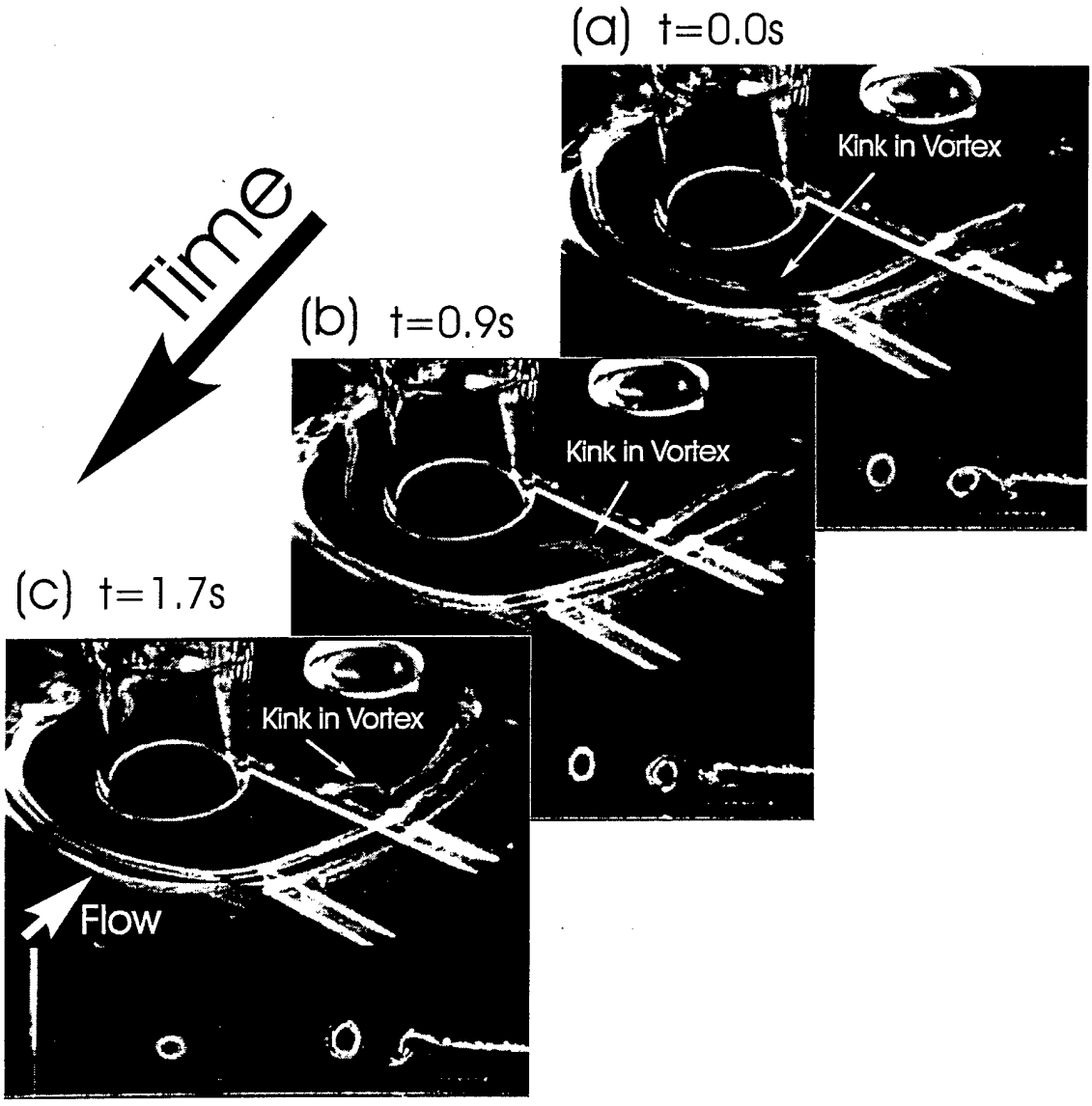

Figure 3.13 Hydrogen bubble visualizations illustrating the effect of a low constant suction rate for a slot location in the *formation* region on an unsteady laminar necklace vortex system. Hydrogen bubble wire located 80mm upstream of the cylinder and ~7mm off the plate surface. U_∞= 8.26 cm/s, Re_L=7.8x10^4, and Re_{δ^*}=481, where Re_L and Re_{δ^*} are calculated for an equivalent, unobstructed, laminar boundary layer at the cylinder location L.

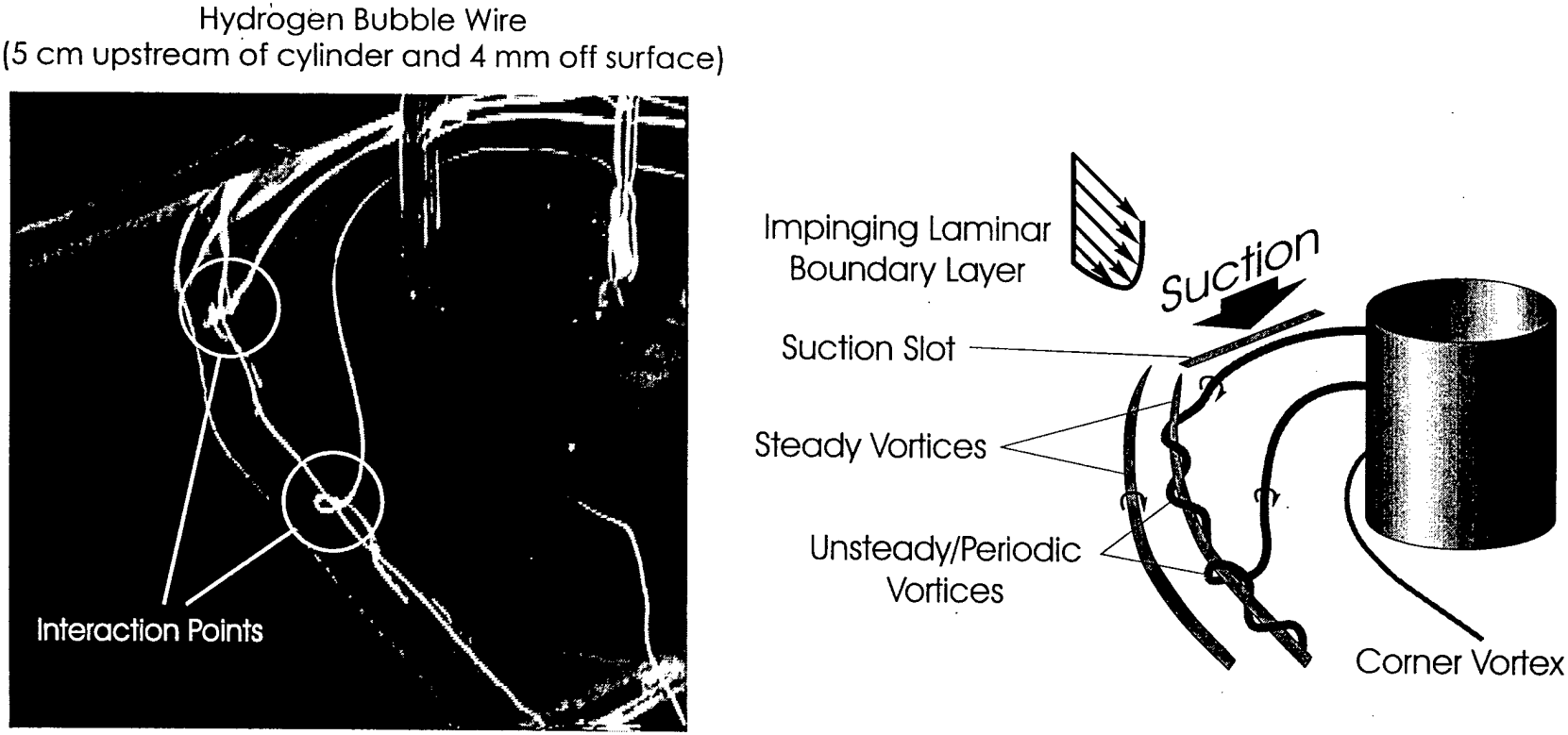

Figure 3.14 Hydrogen bubble visualization and associated schematic illustrating the effect of *moderate* suction, applied through a slot located in the *formation* region, on an unsteady laminar necklace vortex system. Same conditions as figure 3.13.

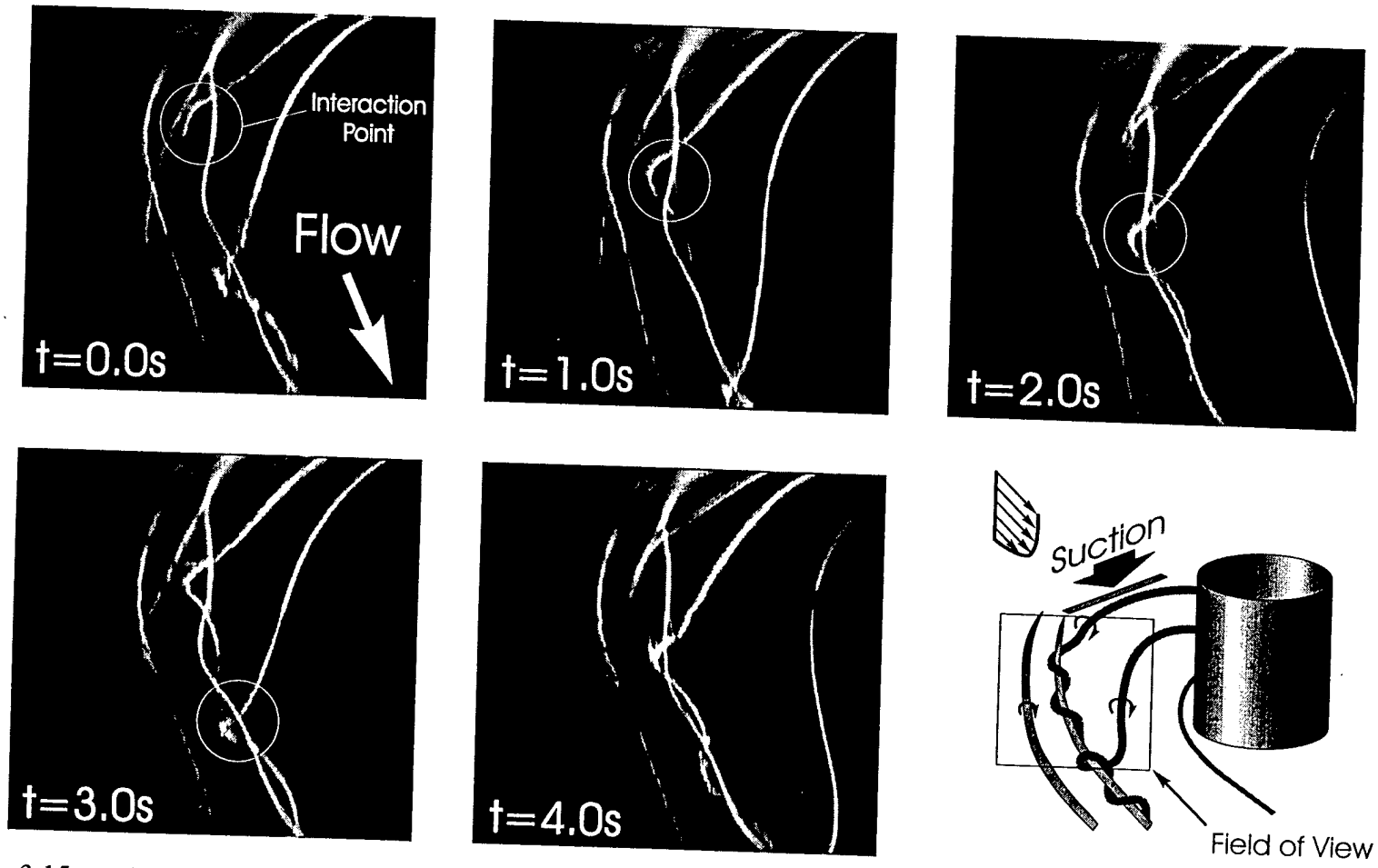

Figure 3.15 Magnified hydrogen bubble time sequence illustrating the periodic, three-dimensional intertwining of the necklace vortices resulting from *moderate* suction applied in the *formation* region of an unsteady, laminar necklace vortex system. Hydrogen bubble wire located 50mm upstream of the cylinder and 4mm off the surface. Same conditions as figure 3.13.

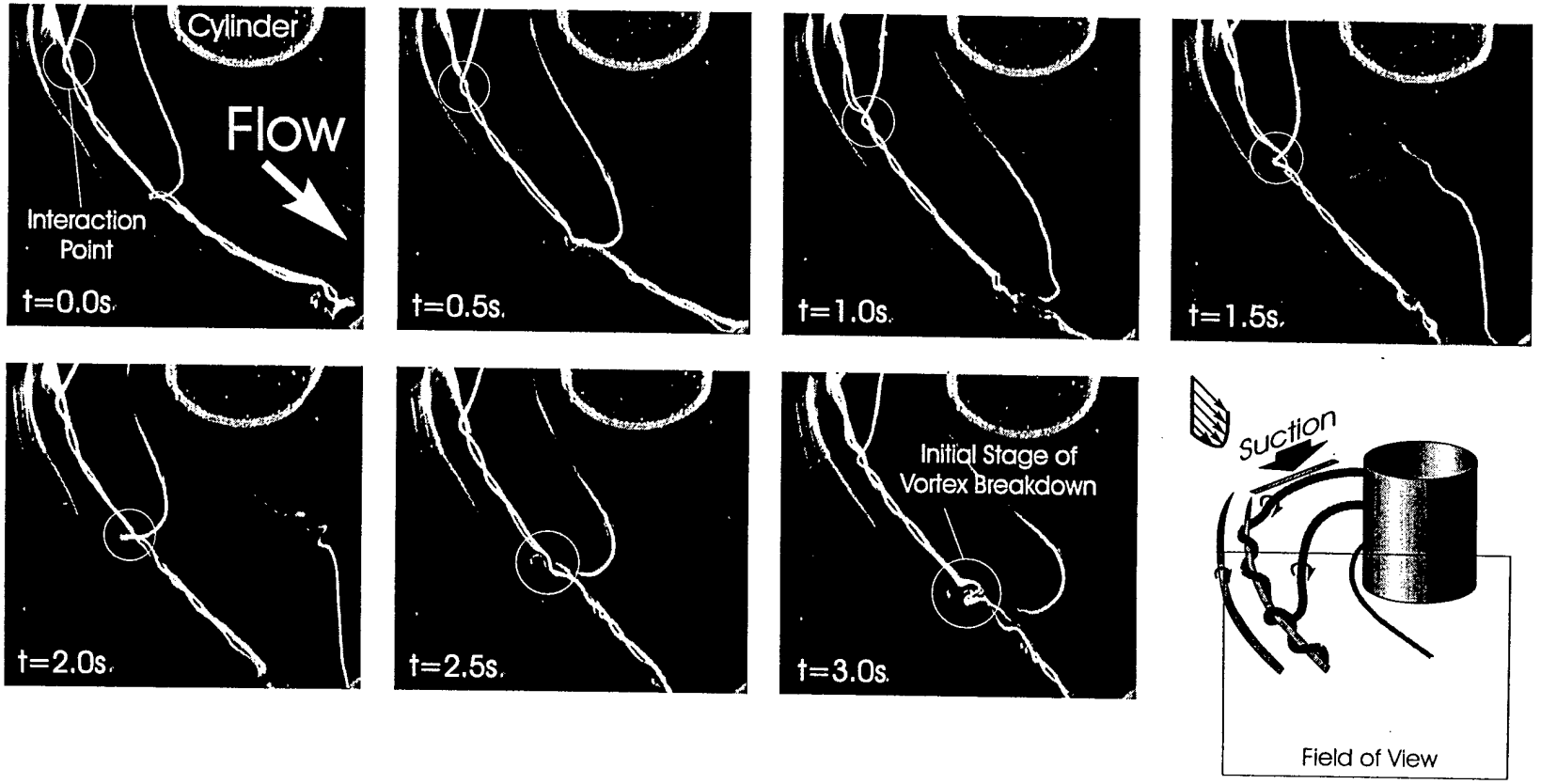

Figure 3.16 Oblique hydrogen bubble time sequence illustrating the temporal details of the downstream flow behavior of the intertwining necklace vortices. Hydrogen bubble wire located 50mm upstream of the cylinder and 4mm off the surface. Same conditions as figure 3.13.

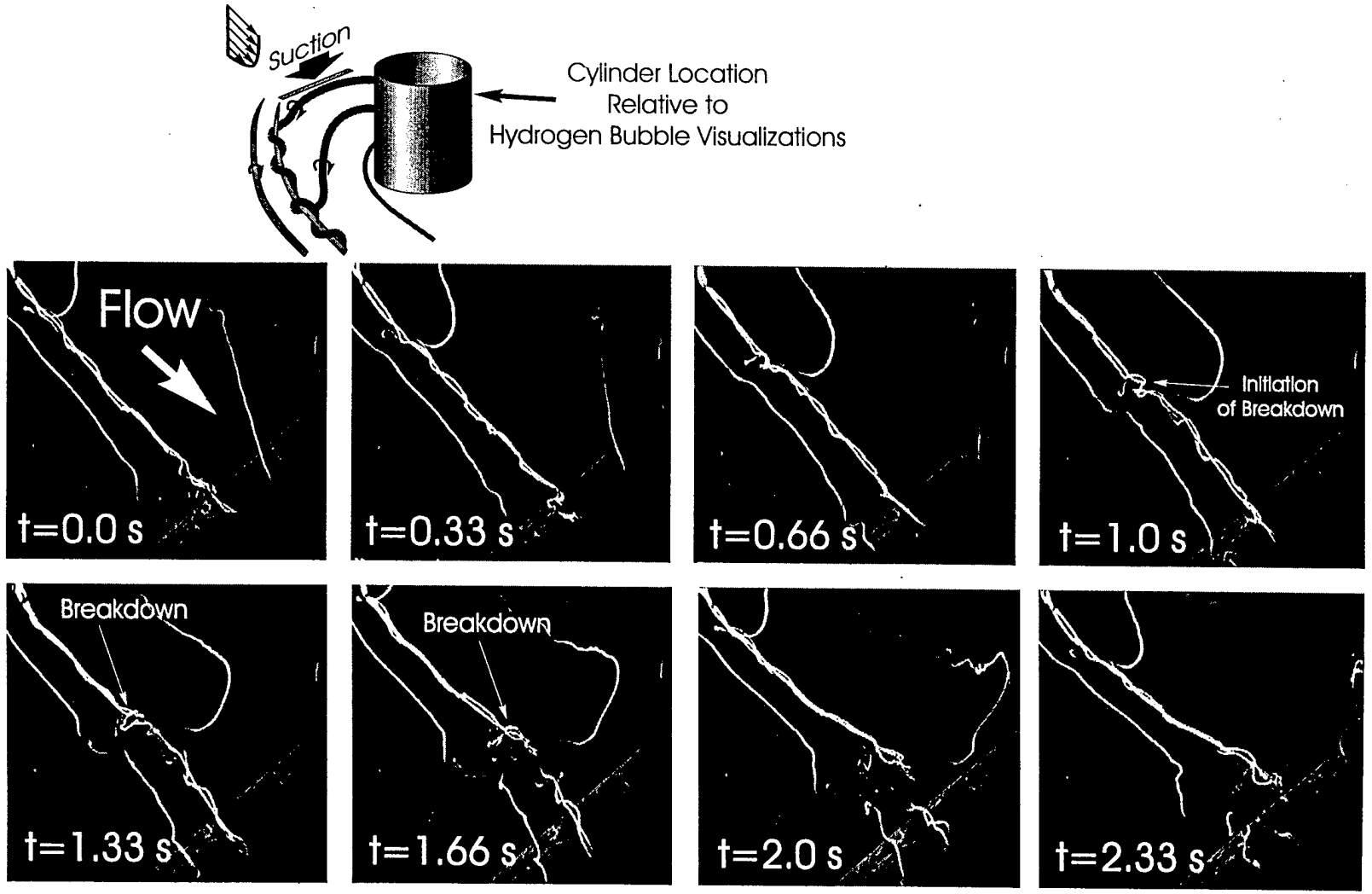

Figure 3.17 Oblique view hydrogen bubble time sequence illustrating the temporal details of the necklace vortex breakdown initiated by the interaction of the two intertwining vortices. Hydrogen bubble wire located 50mm upstream of the cylinder and 4mm off the surface. Same conditions as figure 3.13.

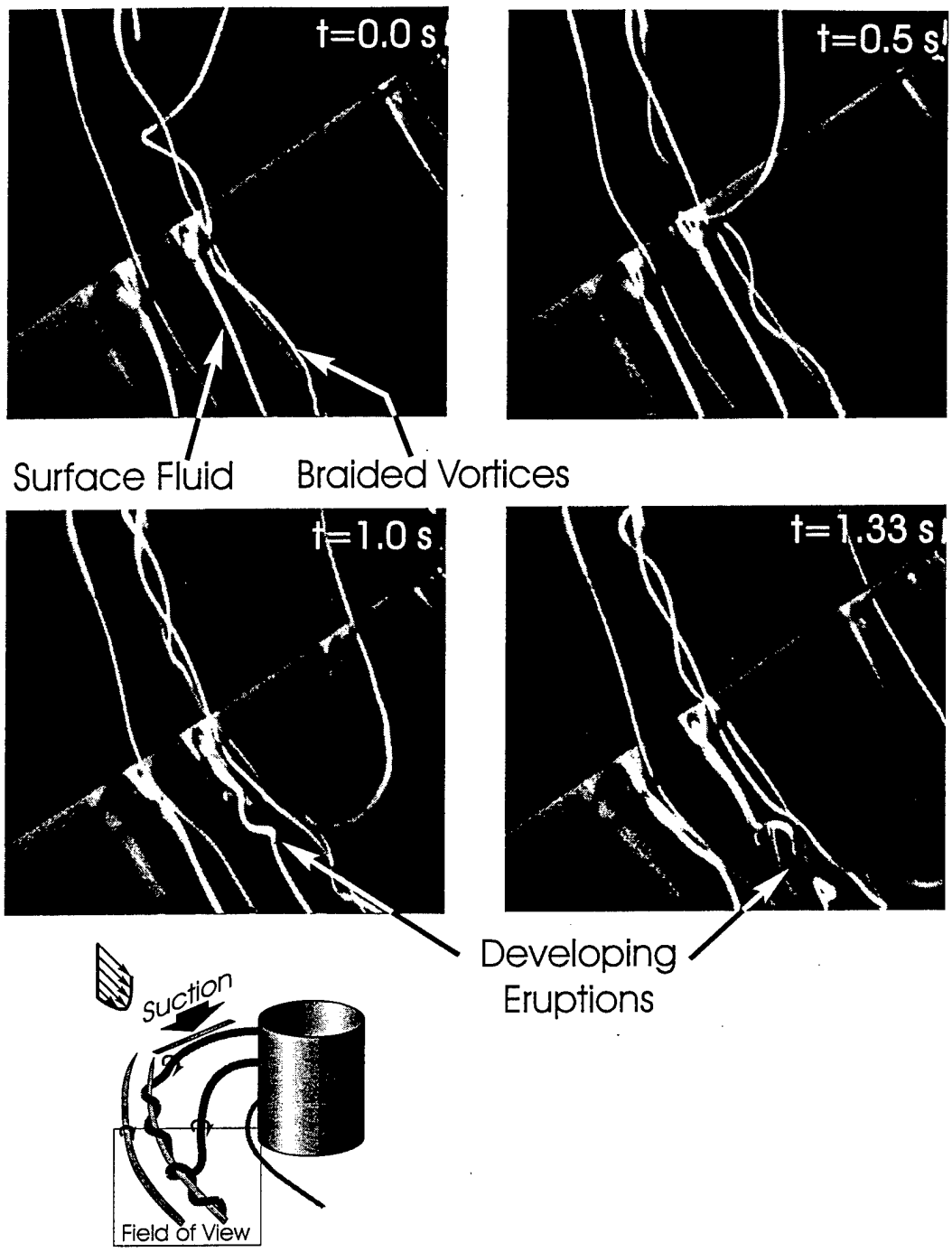

Figure 3.18 Magnified, oblique view hydrogen bubble time sequence illustrating the periodic, three-dimensional intertwining of the necklace vortices and the resultant surface interactions. Visualization was performed with two bubble wires; one upstream, marking the vortex cores (50mm upstream of the cylinder and 4mm off the surface), and a second located on the surface at the cylinder center-line, marking the surface fluid (on the surface at the cylinder centerline). Same conditions as figure 3.13.

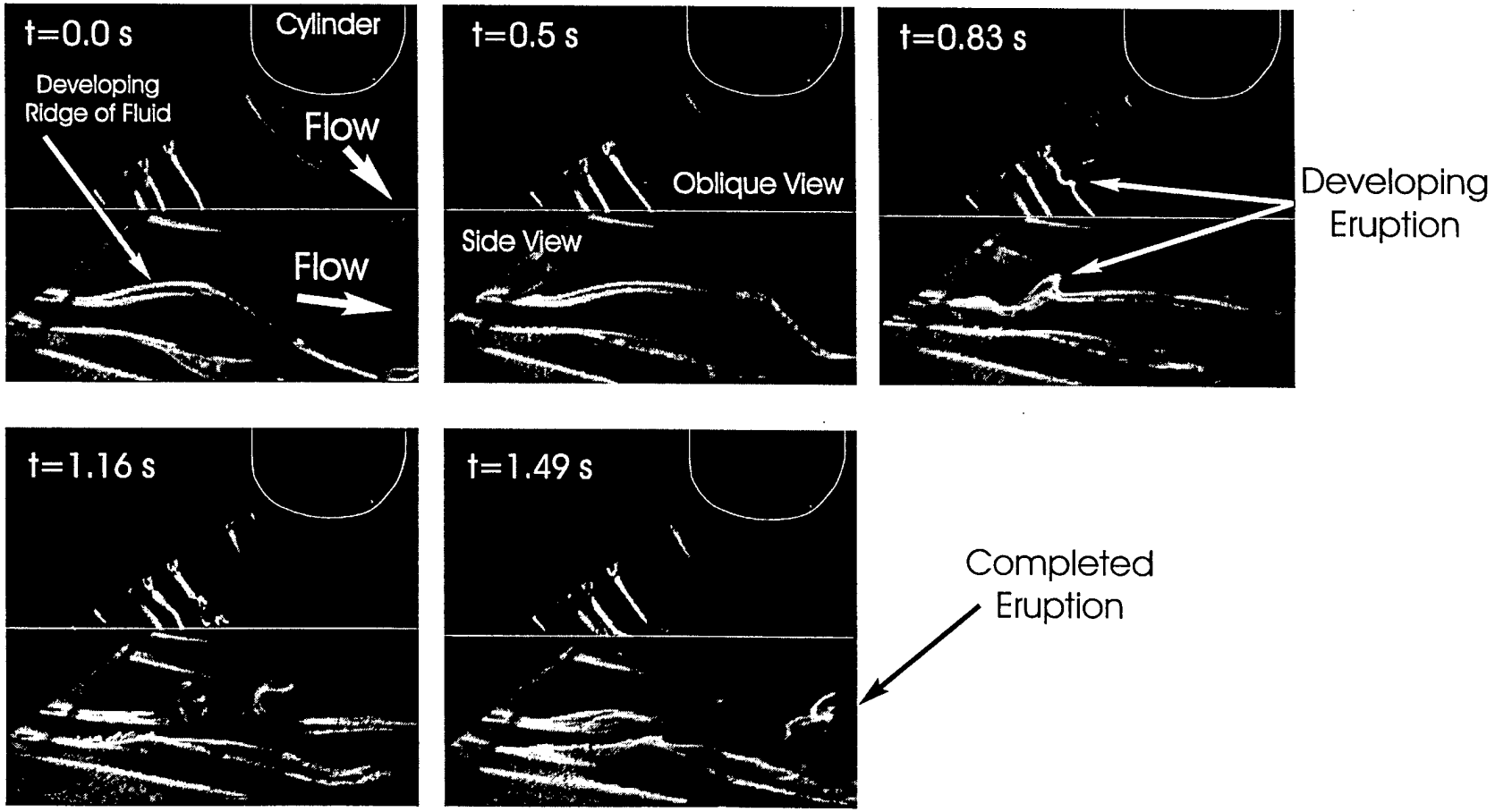

Figure 3.19 Simultaneous oblique and side view hydrogen bubble time sequence illustrating the surface eruptions induced by the intertwining vortices. Hydrogen bubble wire located on the surface at the cylinder centerline. Same conditions as figure 3.13.

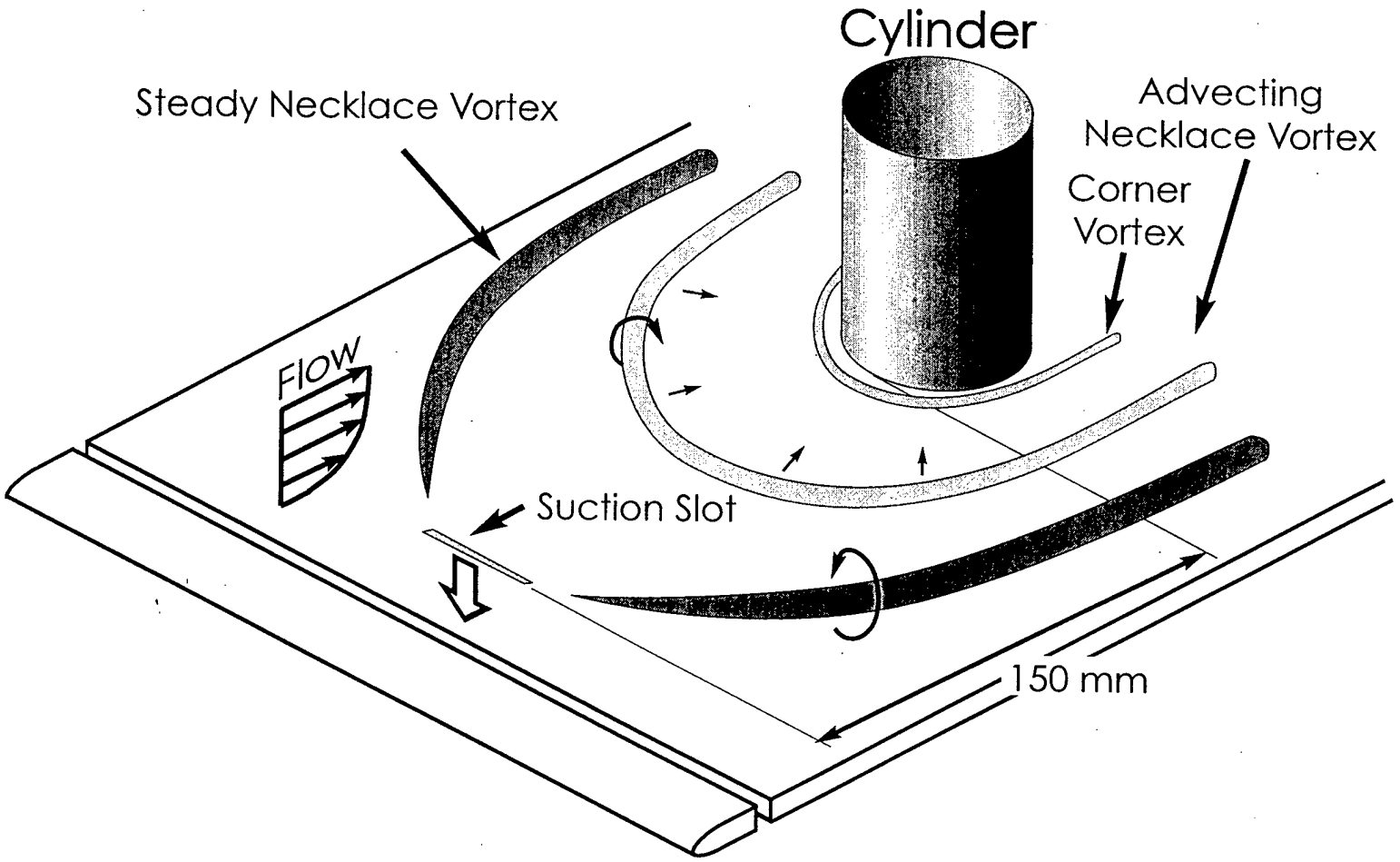

Figure 3.20 Schematic illustrating the effect of constant rate suction for a slot location in the *formation+* region at high/max suction (64→101% U_∞) on an unsteady laminar necklace vortex system.

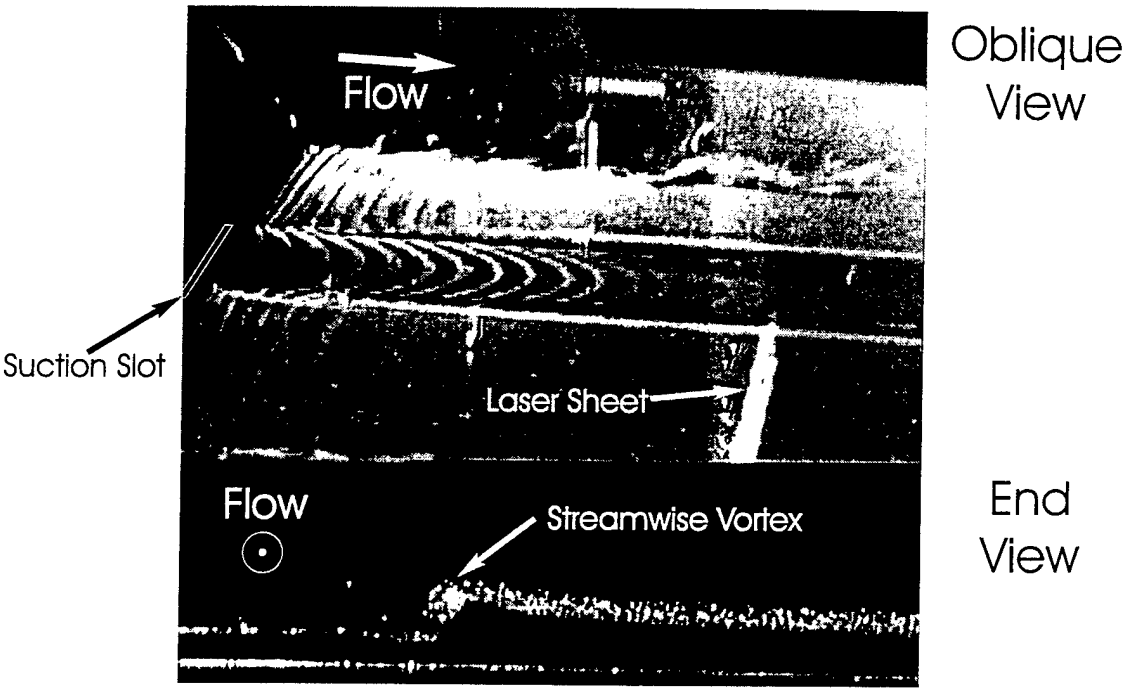

Figure 3.21 (a) Dual-view hydrogen bubble visualization and (b) end-view schematic of the streamwise vorticity introduced at the outboard edges of the suction slot. U_∞=8.26 cm/s, $V_{suction}/U_\infty$=1.01, bubble wire located 1mm off surface and 10mm downstream of slot; laser sheet located 180mm from slot.

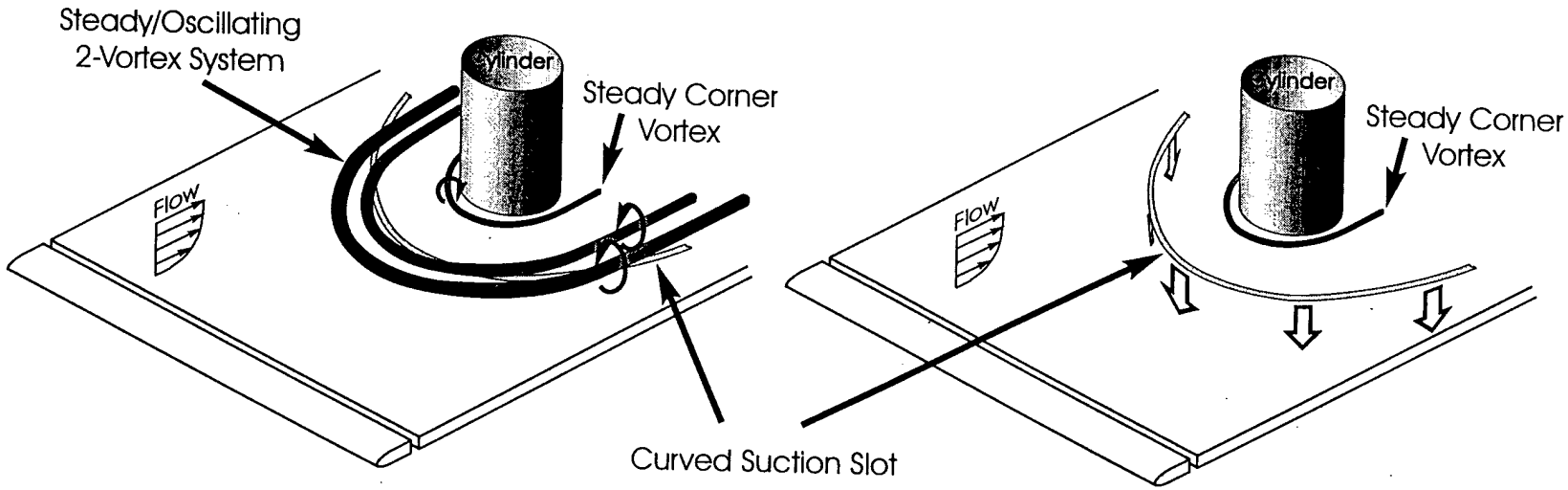

a) No Suction.

b) Suction (65% U_∞).

Figure 3.22 Schematic illustrating the effect of a curved suction slot, with and without suction applied, on an unsteady laminar necklace vortex system. U_∞= 8.26 cm/s, Re_L=6.8x10^4, and Re_{δ^*}=448, where Re_L and Re_{δ^*} are calculated for an equivalent, unobstructed, laminar boundary layer at the cylinder location L.

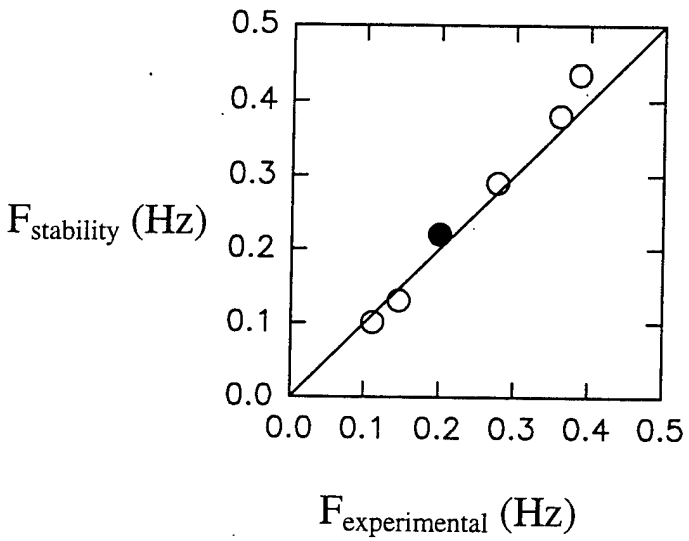

Figure 3.23 Comparison of experimentally-determined necklace vortex breakaway frequencies to frequencies predicted using stability concepts. ○ - θ calculated assuming Blasius formula. ● - θ determined from PIV data.

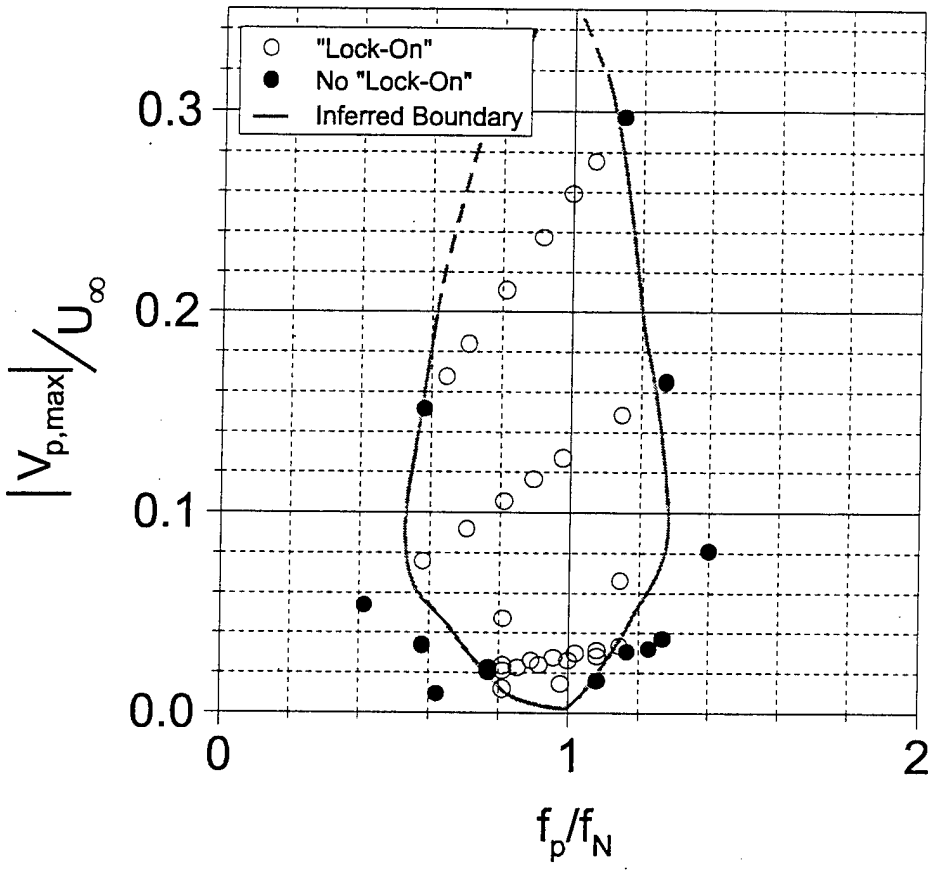

Figure 3.24 Experimentally determined map of the "lock-on" response of an unsteady laminar necklace vortex system in the breakaway regime (formed at the junction of a cylinder and flat plate) subject to sinusoidal forcing via a transverse surface slot (63.5 x 2 mm). Slot located 2.47 diameters upstream of the cylinder (12.7 diameters downstream of the leading edge), U_∞=8.26 cm/s, and f_N=0.48 Hz.

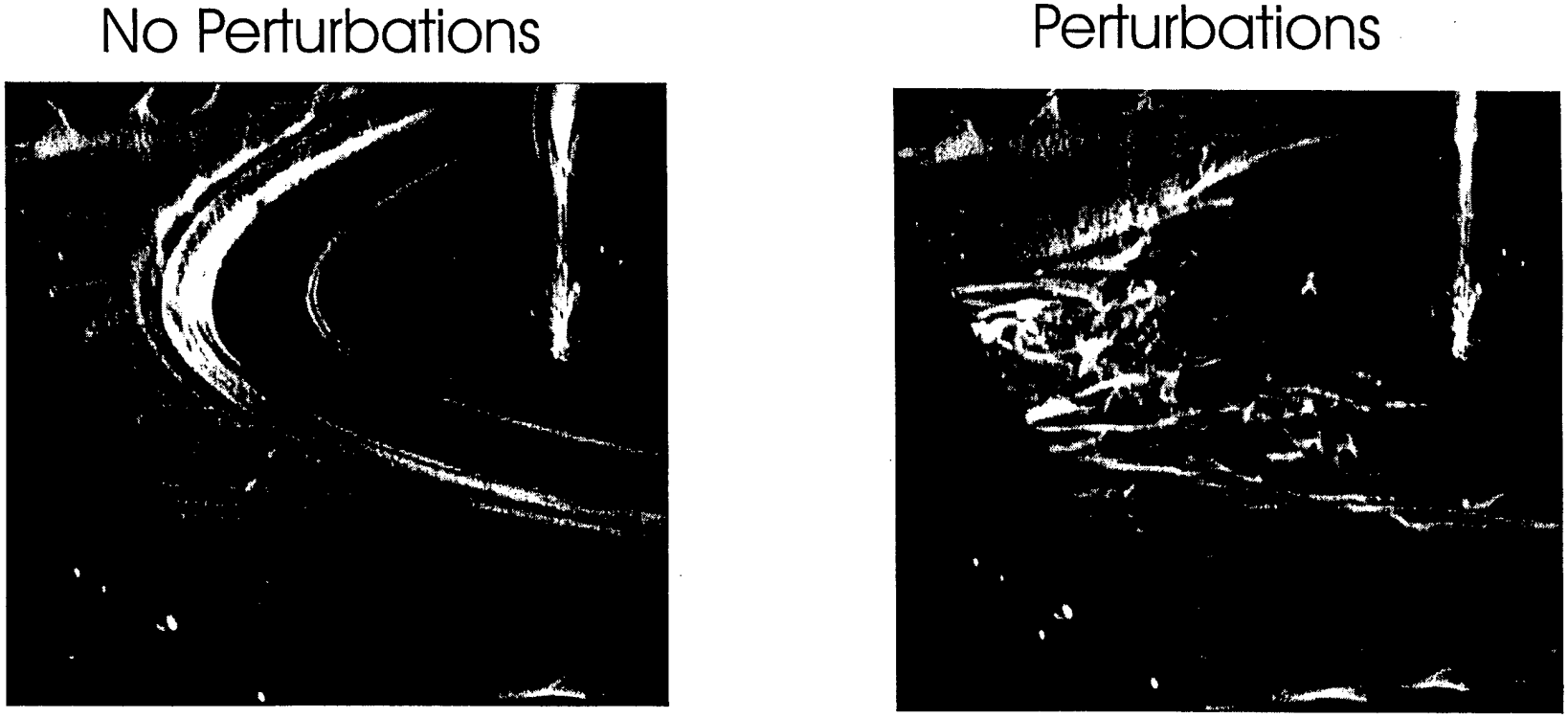

Figure 3.25 Hydrogen bubble visualizations showing the artificial transition of a laminar necklace vortex system caused by appropriate applied perturbations. U_∞=8.26 cm/s, Re_L=9.2x10^4, and Re_{δ^*}=521, where Re_L and Re_{δ^*} are calculated for an equivalent, unobstructed, laminar boundary layer at the cylinder location L. (a) Illustrates the baseline, no perturbation bubble pattern, where the natural breakaway frequency of the necklace vortices is f_b=0.49 Hz. (b) Shows the resultant bubble pattern for a transitioned flow, where perturbations of the form f_p=1.21 Hz and $V_{p,ave}$=0.76 cm/s have been applied (f_p) is the perturbation frequency and $|V_{p,ave}|$ is the average velocity at the slot over one cycle.

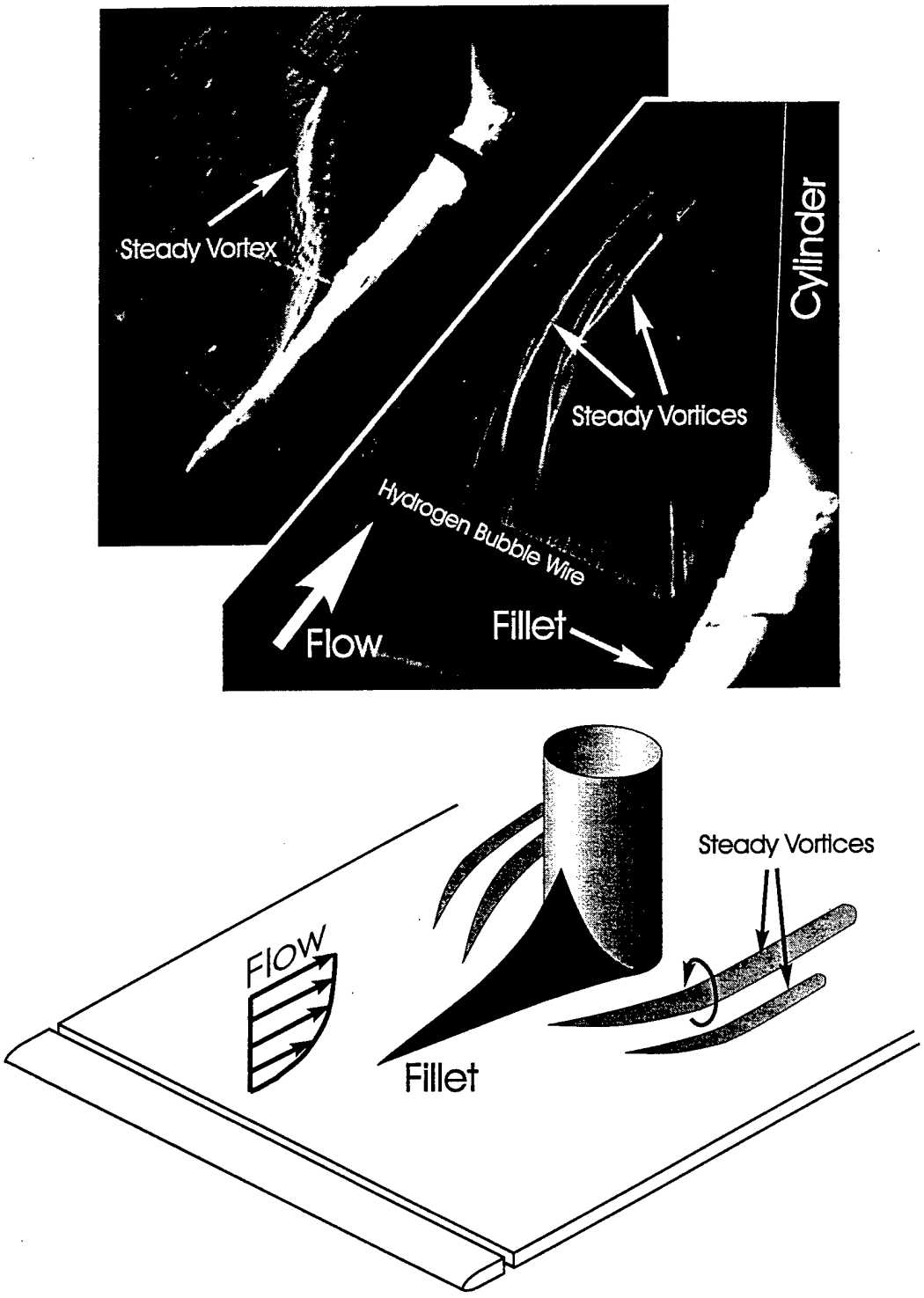

Figure 3.26 Hydrogen bubble visualizations illustrating the effect of a fillet on an unsteady laminar necklace vortex system. U_∞= 8.26 cm/s, Re_L=1.1x10^5, and Re_{δ^*}=570, where Re_L and Re_{δ^*} are calculated for an equivalent, unobstructed, laminar boundary layer at the cylinder location L.

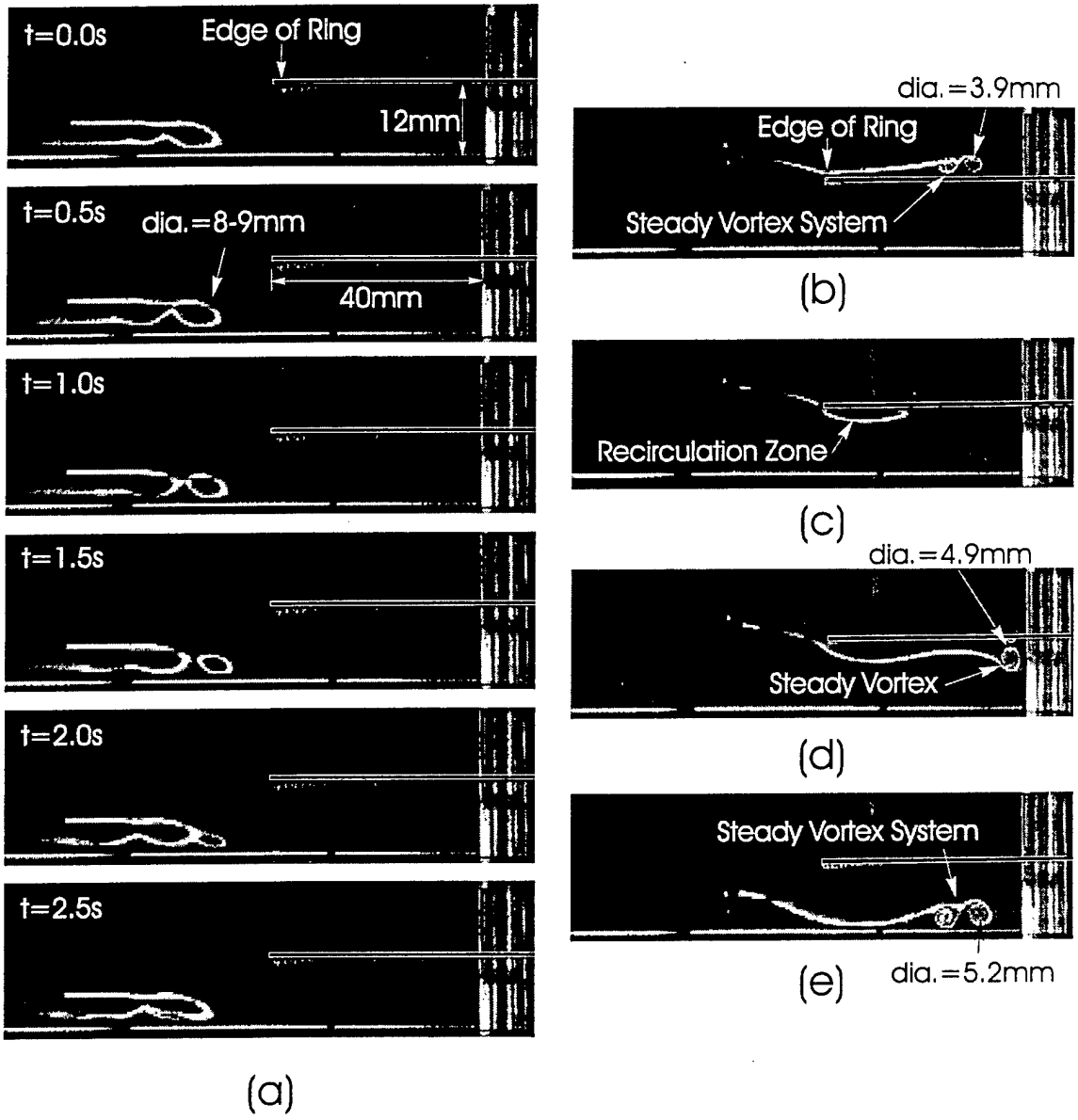

Figure 3.27 Symmetry plane hydrogen bubble visualizations illustrating the effect of a control ring on an unsteady laminar necklace vortex system. (a) Time sequence illustrating the unsteady necklace vortex behavior upstream of the ring. (b)-(e) Selected visualizations illustrating the steady necklace vortex systems formed above and below the ring. U_∞= 8.26 cm/s, Re_L=7.6x10^4, and Re_{δ^*}=475, where Re_L and Re_{δ^*} are calculated for an equivalent, unobstructed, laminar boundary layer at the cylinder location L.

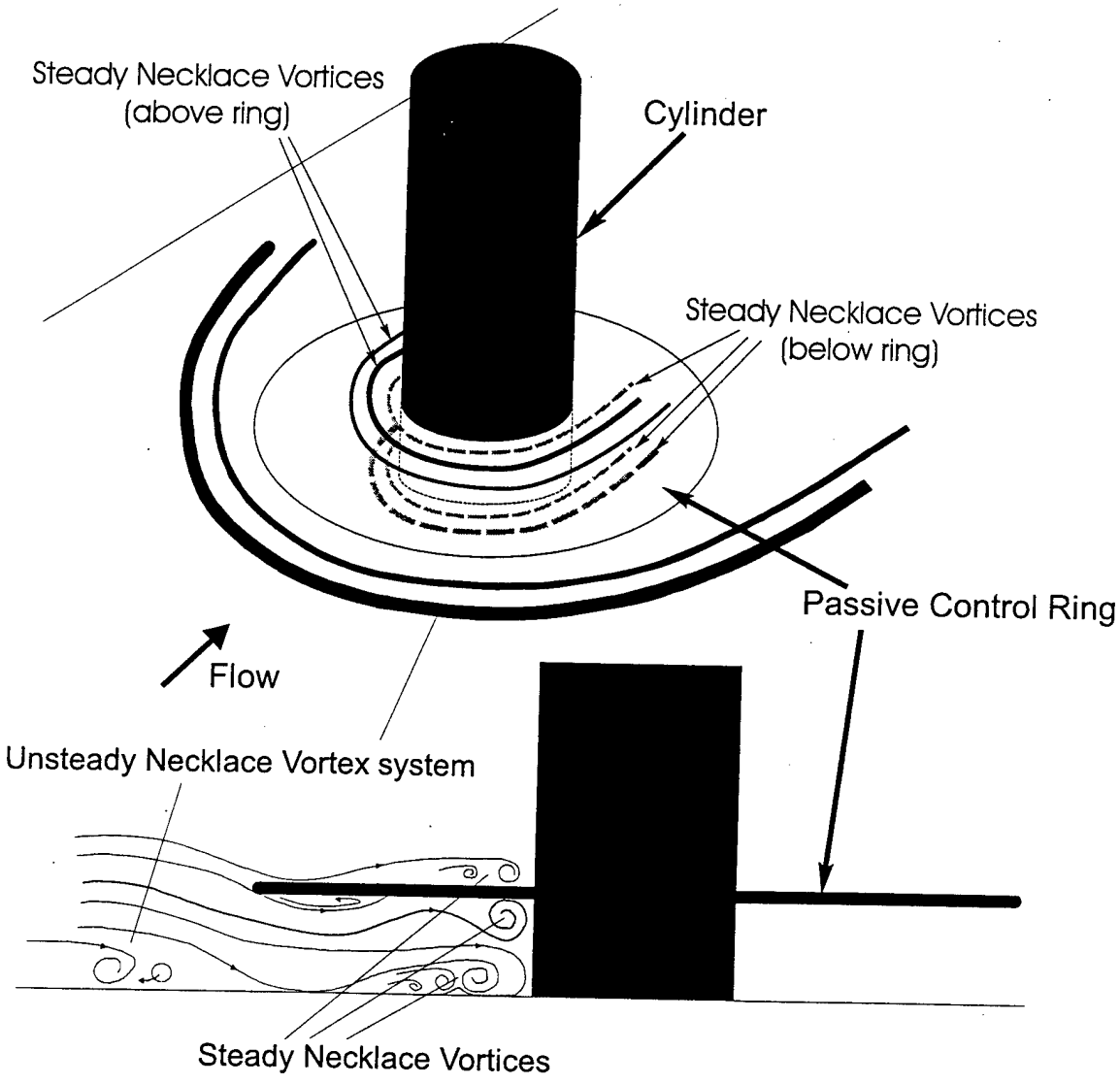

Figure 3.28 Oblique and side view schematic interpretations of the effect of a control ring on an unsteady laminar necklace vortex system.

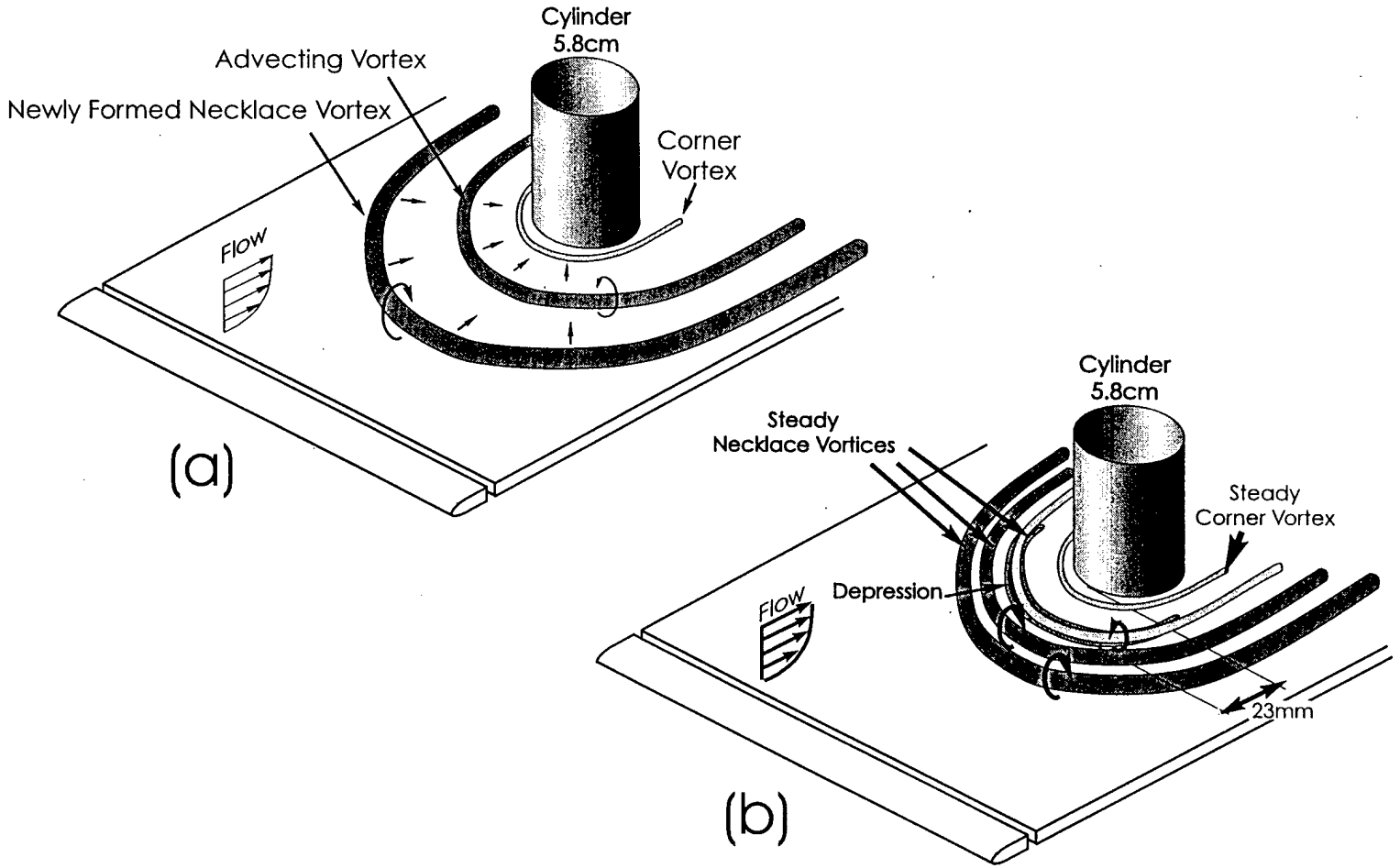

Figure 3.29 Oblique schematic illustrating (a) the baseline unsteady laminar necklace vortex system and (b) the modification of the unsteady laminar necklace vortex system by a curved depression in the approach region of the flat plate. U_∞= 13 cm/s, Re_L=1.2x10^5, and Re_{δ^*}=587, where Re_L and Re_{δ^*} are calculated for an equivalent, unobstructed, laminar boundary layer at the cylinder location L.

4.0 TURBULENT JUNCTION FLOW CONTROL RESULTS and DISCUSSION

4.1 Introduction

This section describes the results of qualitative flow visualization and Particle Image Velocimetry (PIV) for a turbulent necklace vortex system. Experiments were performed on baseline (i.e. without control) and controlled cases. The results of the baseline case study will illustrate, in some detail, the genesis and behavior of a turbulent necklace vortex system. The results of the controlled cases will illustrate the effect of control on the topology, temporal behavior, and strength of the turbulent necklace vortex system.

The turbulent case is characterized by the formation of a large-scale, unsteady turbulent vortex upstream of the body, with the position, size and strength of the vortex varying randomly (Devenport and Simpson, 1989). This vortex forms downstream of a line of separation (which was previously a line of attachment for the laminar case) (Hung *et al.*, 1991). Figure 4.1 shows selected instantaneous hydrogen bubble visualizations of turbulent junction flow, illustrating the three-dimensional complexity and variations of the turbulent necklace vortex (T.V.).

4.2 Flow Control

4.2.1 *Constant Rate Suction*

PIV experiments were performed to assess the effect of constant rate surface suction on a turbulent necklace vortex system. An 8.8cm diameter cylinder was placed 92.2cm downstream of the plate leading edge, with the suction slot located 22mm upstream of the cylinder (see §2.2.1). Recall that the slot is 2mm x 63.5mm in a cross-stream orientation. The free-stream velocity was set to U_∞=12.5 cm/s and the boundary layer tripped using a 4.8mm diameter threaded rod located at the plate leading edge, which gives $Re_L=1.1x10^5$, $Re_D=1.1x10^4$, and $Re_{\delta*}=422$, where Re_L is the Reynolds number based on the distance to the cylinder (L), Re_D is based on the cylinder diameter (D), and $Re_{\delta*}$ is based on the displacement thickness for an unobstructed turbulent boundary layer at the cylinder location. Two nondimensional suction velocities were examined: $V_{suction}/U_\infty=0.29$ and $V_{suction}/U_\infty=0.68$, where $V_{suction}$ was the average velocity of fluid at the slot, computed by measuring the volumetric flow rate through the slot and dividing by the slot area.

Data was acquired on the symmetry plane and at three downstream cross-stream locations, as described in chapter 2 (figure 2.16). Two sampling rates were employed. On the symmetry plane, data was acquired at both 2 and 5 Hz. For the end-views, data was acquired at 5 Hz only. The total number of samples acquired at a given time was limited by the recording method (35mm film camera) to 33-36 frames. The instantaneous data was used to examine both the temporal behavior of the flow and the averaged flow behavior.

4.2.1.1 Instantaneous behavior

Figure 4.2 presents selected instantaneous vorticity plots, from figures A.1 and A.2 in the Appendix, acquired in the symmetry plane for (a) the baseline (no suction) and (b) maximum suction ($V_{suction}/U_\infty$=0.68) cases. The data presented in these figures was acquired at 5 Hz, which allowed a detailed analysis of the temporal flow behavior. Figure 4.2 illustrates the strongest vortex-surface interaction and largest vortex diameter observed for the (a) baseline data, and (b) the suction data. For the baseline case, the vortex-surface interaction manifests as an eruptive tongue of positive vorticity (solid lines), which extends to a maximum of approximately 12mm from the surface at t=1.2s. For the applied suction case, this eruptive behavior is still observed, but the extension of the eruptive tongue has been reduced to a maximum of 8mm at t=1.0s. In addition, comparison of figure 4.2 (a) to 4.2 (b) shows that suction reduces the maximum diameter of the turbulent necklace vortex from ~10mm for the baseline case to approximately 5mm (50% of the base case) with applied suction.

A further comparison of the collective instantaneous symmetry plane vorticity plots for an entire experimental run (figures A.1 and A.2), acquired at 5Hz for the baseline and maximum suction case respectively shows a distinct loss of coherency with applied suction. Notice that in figure A.1 virtually all frames have **distinct** regions of generally circular vorticity contours associated with the turbulent necklace vortex. However, in figure A.2, only ~22 of the 36 frames appear to have similar circular vorticity patterns, with approximately half of these patterns reflecting a coherence and

strength markedly less than for the typical baseline case. This comparison suggests that suction generally weakens the turbulent necklace vortex. (Note: the averaged PIV data presented below, illustrates that *on average*, the turbulent vortex is essentially removed by the surface suction).

4.2.1.2 Average Streamlines and Vorticity

Symmetry Plane

Figure 4.3 shows the effect of constant-rate suction (at x=30mm) on the average vorticity and streamlines on the symmetry plane. For this figure, data was recorded at 2 Hz for 16½-18 seconds; the instantaneous velocity and vorticity fields were then averaged. The vorticity contour levels in this figure range from -40 to -10 and 10 to 80 in intervals of $5s^{-1}$, with the dashed and solid lines indicating negative and positive vorticity respectively.

Figure 4.3 (a) illustrates the no suction baseline case ($V_{suction}/U_{\infty}=0.0$). The streamline plot shows the existence of a relatively large-scale primary turbulent necklace vortex close to the cylinder (centered at x=30mm), as well as a smaller secondary vortex upstream (at x=13.5mm). The vorticity plot also reveals these structures, providing an indication of their strength. The vorticity plot displays a relatively large region of strong negative vorticity close to the cylinder (hereafter referred to solely as the primary vortex), which appears to be composed of two vorticity concentrations. The first concentration (labeled "A" in the figure) is associated with the necklace vortex seen in the streamline plots and has a peak value of $-25.6s^{-1}$. The second concentration (labeled "B") would

seem to be associated with the turning of the impinging flow upstream by the cylinder and has a peak value of $-23.2s^{-1}$. The secondary vortex appears as a weak smaller-scale concentration upstream of the slot (centered at x=14mm), with a peak vorticity value of $-15.5s^{-1}$.

The circulation strength of the primary vortex was established using equation (4) of chapter 3. An iso-vorticity contour of $\omega=-10s^{-1}$ (indicated on the figure) was chosen as the integration path, such that both vorticity concentrations ("A" and "B" on the figure) were encompassed; this was assumed to reflect the net effect of the vorticity concentrations on the *total* vorticity distribution. Using this approach, the resultant strength of the primary vortex was $\Gamma=1150\ mm^2/s$

Figure 4.3 (b) and (c) illustrate the effect of suction on the *total* vorticity distribution on the symmetry plane. For $V_{suction}/U_\infty=0.29$ the streamline plot indicates that (1) the primary vortex has been eliminated, and (2) the secondary vortex has been reduced in size and drawn upstream towards the slot. However, the vorticity plot still reveals a concentration of negative vorticity downstream of the slot, which is primarily a reflection of the local boundary layer caused by the reverse flow moving upstream from the cylinder. The size and magnitude of this vorticity region (the remnants of "A" and "B") has been reduced to a peak vorticity of $-22.6s^{-1}$. The circulation strength of this vorticity region (determined using the same vorticity integration contour as the baseline case) is $726\ mm^2/s$: a 37% decrease in strength from the baseline. Although this vorticity region does not appear to be associated with a vortex per se, end-view results (presented below) show that this modified vorticity redevelops into a coherent vortex along the side

of the cylinder. Note that immediately upstream of the slot a region of negative vorticity appears, which is comprised of the vorticity associated with the modified secondary vortex as well as negative vorticity apparently introduced by the action of the suction slot (i.e. the rapid turning of streamlines towards the plate and into the slot). Note that the peak vorticity ($-16.4s^{-1}$) at the location of the secondary vortex is roughly the same as for the no suction case.

For the maximum suction case, $V_{suction}/U_\infty=0.68$, the streamline plot again indicates the elimination of both the primary necklace vortex, as well as the secondary vortex. The vorticity plot reveals that the region of negative vorticity closest to the cylinder is further reduced in size, but the peak magnitude of the vorticity in this region remains essentially the same ($-21.4s^{-1}$) as for the moderate suction case. However, the strength of the region of vorticity (as measured about the $\omega=-10s^{-1}$ contour) is further reduced to $\Gamma=503\ mm^2/s$: a 56% decrease from the baseline value. The vorticity plot also illustrates the total elimination of the vorticity concentration associated with a secondary vortex. The only prominent feature upstream of the slot is a layer of negative vorticity adjacent to the wall which is increased in strength and coherence (from the previous cases) because the approaching fluid, closest to the wall, has been accelerated by the slot suction.

End-Views

Figures 4.4-4.6 illustrate the effect of suction on the downstream extensions of the turbulent necklace vortex. For the end-views, PIV data was taken in cross-stream planes

at streamwise locations of 0, 1, and 2 radii downstream of the cylinder centerline (figure 2.12) for both baseline (no suction) and $V_{suction}/U_\infty$=0.68 cases (shown as the top and bottom of the figures respectively). For all three figures, data were sampled at a rate of 5 Hz for 6.6-7.2 seconds, averaged, and the subsequent streamline and vorticity fields computed as described in §2.5.

Figure 4.4 illustrates the effect of suction on the turbulent necklace vortex in the medial cross-stream plane (1 radii from the leading edge). It is interesting to note the lack of any apparent vortical structure in both average streamline plots. In fact, both streamline patterns indicate only a general right-to-left flow due to the lateral diversion of the flow around the cylinder. However, examination of the vorticity plots suggests that a coherent turbulent vortex may be present. The vorticity plot of figure 4.4 (a) (the baseline case) shows a concentration of negative vorticity centered at ~50mm (with a peak vorticity of -12.1s^{-1}). Using the same methods described above, and employing ω=-4s^{-1} as the integration path (indicated on the figure), the circulation strength was determined as 602 mm^2/s. When strong suction is applied (figure 4.4 (b)) two concentrations of vorticity, bounded by the ω=-4s^{-1} contour, are present. The first, closest to the cylinder (centered at ~60mm, with a peak vorticity of -8.0s^{-1}), is indicative of the modified turbulent junction vortex and has a circulation strength of 250 mm^2/s, a reduction of 58.6% from the baseline case. The other concentration (centered at ~43mm, with a peak vorticity of -6.9s^{-1}) is postulated to originate from an additional vortex generated at the outboard edge of the slot due to the interaction of the suction with the approaching flow (figure 3.22) and has a strength of 291 mm^2/s. If the strengths of the two vorticity

concentrations are combined, the result (541 mm^2/s) is approximately 10% less than the baseline case.

Figure 4.5 illustrates the behavior in the cross-stream plane at a streamwise location even with the trailing edge of the cylinder. The baseline streamline plot now clearly shows the presence of the necklace vortex as an unstable (i.e. outward spiraling) focus. The companion vorticity plot shows the associated vorticity concentration (peak vorticity of $-8.8s^{-1}$). The vortex strength at this location was determined as Γ=492 mm^2/s, using ω=$-6s^{-1}$ as the integration path. Application of strong suction modified, but did not eliminate, the trailing vortex as evidenced by the streamline pattern; both the peak vorticity ($-6.5s^{-1}$) and the apparent strength (Γ=223 mm^2/s, a 54.7% decrease from the baseline), were reduced. Note that the size of the vorticity concentration was also reduced.

Figure 4.6 illustrates the effect of suction in the cross-stream plane, 1 radius downstream of the trailing edge of the cylinder, illustrating behavior similar to that for the two previous cases. The baseline case (figure 4.6 (a)) illustrates the presence of the necklace vortex in both the streamline and vorticity plots. The strength of the vortex, using ω=$-2s^{-1}$ as the integration path, was determined as Γ=369 mm^2/s, with a peak vorticity value of ω=$-4.5s^{-1}$. Under strong suction, both the spatial extent of the vorticity concentration is reduced and the vortex strength decreases to Γ=260 mm^2/s (a 30% decrease). The peak vorticity value, however remains relatively constant at ω=$-4.9s^{-1}$.

4.2.1.3 Reynolds-Stress

Symmetry Plane

Figure 4.7 shows the effect of constant rate suction on the averaged Reynolds-stress on the symmetry plane determined from the PIV data. The Reynolds-stress was computed via the equation

$$\overline{u'v'} = \frac{1}{T}\int_0^T u'v'dt, \tag{7}$$

where T is the total sample time of the data (i.e. 16½-18 seconds). The quantities u' and v' were established by subtracting the averaged velocity from the instantaneous velocity at every point in the flow field for all datasets. Iso-contours are plotted over a range of -450 to -50 and 50 to 250 in intervals of 50 mm^2/s^2, with dashed and solid lines denoting respectively negative and positive values.

Figure 4.7 (a) shows the baseline (no suction) case, which indicates a large region of negative Reynolds-stress, labeled "1", which is coincident with the location of the turbulent necklace vortex, illustrated in the average streamlines and vorticity concentration "A" in figure 4.3 (a). Additionally, downstream of this region is a region of elevated positive **and** negative vorticity, labeled "2", which has the structure of a relatively symmetric quadrapole, with the strongest two concentrations residing in the lower two quadrants. The location of this region coincides with vorticity concentration "B" indicated in figure 4.3 (a). It is important to note that this same Reynolds-stress pattern (i.e. a region of negative stress and a quadrapole region) is similar to patterns observed in other sets of baseline experimental data (not presented here).

As the nondimensional suction rate ($V_{suction}/U_\infty$) is increased from 0 to 0.29 and 0.68, a drastic reduction in Reynolds-stress levels occurs. For the baseline case, the peak negative and positive Reynolds-stress values are -474 and 282 respectively (note that the positive value cited refers to the positive concentration in the region "2"). Under moderate suction of $V_{suction}/U_\infty$=0.29, the Reynolds-stress peaks decrease to -224 and 81 and the quadrapole structure has been removed; application of maximum suction ($V_{suction}/U_\infty$=0.68) results in a further reduction in peak Reynolds-stresses to -100 and 70 (again note the removal of the quadrapole structure). Because negative values of Reynolds-stress on the symmetry plane, u'v', contribute to the drag force on the flat plate, suction acts to reduce drag by decreasing the stress levels.

End-Views

Figure 4.8 illustrates the change in Reynolds-stress in the three downstream cross-stream planes due to suction; the results are derived from the data used for vorticity contours in figures 4.4-4.6. Figure 4.8 (a) shows the results for the medial cross-stream plane. For the baseline case, a region of relatively high Reynolds-stress exists with peak values of -199 and 192. The location of this region generally coincides with the location of the vorticity concentration present in figure 4.4 (a), and hence with the location of the necklace vortex itself. It also has a structure similar to that noted for the symmetry plane baseline case, with a negative concentration (labeled "1") and a region of positive and negative stress (labeled "2"), which has a structure *reminiscent* of the quadrapole observed on the symmetry plane. Note that it is the quadrapole structure that most

precisely matches the location of the vortex, as determined from the vorticity contours of figure 4.4 (a). The other stress concentration, "1", is centered at x=37mm and would seem to be associated with an eruption of wall vorticity, which appears as the slight bulging of the positive vorticity contours near the wall in figure 4.4 (a). With suction applied, the peak Reynolds-stresses decrease to -68 and 50, and the spatial extent of the stress concentrations is reduced. However, the general shape of the contours remains similar to the baseline case; this is in contrast to the symmetry plane case, where it was observed that suction modified both the structure of the stress contours (i.e. eliminated the quadrapole) as well as their magnitude. This would suggest that the influence of suction on the Reynolds-stress decreases with downstream position.

At the trailing edge cross-stream plane (figure 4.8 (b)), the unmodified data again shows a region of high Reynolds-stress with peak values of -181 and 194. Again, a quadrapole-type structure is present, centered at x=50mm and labeled "2"; this structure again closely matches the location of the vortex as defined by the vorticity contours of figure 4.5 (a). Similar to the medial plane results, a concentration of negative stress (labeled "1"), centered at x=38mm, appears to be associated with an eruption of positive wall vorticity. Application of suction (68% of the free-stream) reduces the peak stress levels to -96 and 34 and reduces the spatial extent of the stress concentrations. In addition, the quadrapole-type stress contours are replaced with a single concentration of negative stress at x=50mm, which is coincident with the location of the weakened vortex (figure 4.5 (b)). Also evident in figure 4.8 (b) (suction case) is a weakened region of

negative stress at x=40mm associated with the wall vorticity eruption induced by the weakened vortex.

Finally, in the cross-stream plane one radius downstream of the trailing edge (figure 4.8 (c)), the baseline Reynolds-stress concentrations reach peak values of -81 and 50, with a region of positive and negative stress (labeled "2") generally coincident with the location of the vortex, but without a quadrapole form. Outboard of region "2" is a relatively large area of negative stress (labeled "1"), which based on the upstream data, should be associated with an eruption of surface fluid, although a clear indication of such an eruption is not present in figure 4.6 (a). At this streamwise plane, application of suction has minimal impact on the Reynolds-stress levels, with peak values altered minimally (to -70 and 56), but the spatial extent of the stress contours was reduced. This reduced influence of suction at the most downstream location again suggests (as stated above) that the impact of suction of the vortex legs diminishes with downstream location.

In the end-view planes the Reynolds-stress, $u'v'$, does not contribute to the drag force, but rather is an indication of how "violent" the flow is (i.e. it gives an indication of added momentum due to the fluctuating velocity components), which is important when considering the effects of the legs of the vortex impinging on control surfaces and/or sensors. So, by reducing the Reynolds-stress levels, the unsteady forces imparted to downstream structures and/or sensors is also reduced. For the one radius downstream case, where suction did not effect stress levels, the spatial extent of the stress concentrations was reduced, which in turn implies that any force imparted to a downstream structure will be applied over a reduced area.

4.2.1.4 Vorticity Dynamics

To assess the influence of spatially-limited suction on the dynamics of the legs of the turbulent necklace vortices, a novel visualization technique illustrated in figure 4.9 was developed. Using this approach, the instantaneous (2-D) vorticity data obtained at a given location and suction rate was stacked into a 3-D volume, with the axes representing x, y, and time (t), as shown in figure 4.9 (a). Using this 3-D dataset, a *translucent* iso-vorticity surface is generated and rendered in 3-D space, as shown in figure 4.9 (b). The volume is then rotated and viewed along the time axis (figure 4.9 (c)), such that the iso-surface is viewed end-on. This final 2-D plot now provides a *qualitative* indication of the temporal position and frequency of occurrence of the selected vorticity level by showing "blobs" of gray wherever and whenever a selected vorticity level appears. Since the iso-surface is rendered translucent, visualization of the frequency with which a selected vorticity level appears is possible since the vorticity "blobs" do not obscure each other. Also, locations where the surfaces overlap appear darker, indicating that the vortex (at the reflected vorticity level or greater) was present at that location more frequently than elsewhere.

Figure 4.10 (a), constructed using the technique described above with ω=-25s^{-1} as the iso-vorticity level, shows the influence of suction on the dynamics of the turbulent necklace vortex at the medial cross-stream plane. The baseline case indicates a focused concentration of a relatively high number of "blobs" of gray, which suggest that the vortex exhibited relatively little spatial movement during the experiment. Several changes are noted with the application of strong suction. One, the "blobs" of gray are

distributed over a larger area than in the baseline case, indicating that the vortex exhibited larger spatial movement. Secondly, the size of the "blobs" has decreased, reflecting a weakening in the strength of the vortex. Thirdly, the total number of "blobs" decrease (i.e. a reduced frequency of appearance of vorticity contours of at least $-25s^{-1}$).

Figure 4.10 (b) and (c) illustrate the effect of suction on the turbulent junction vortex dynamics in the cross-stream plane at both the trailing edge and one radius removed from the trailing edge, again using $\omega=-25s^{-1}$ as the selected level. At the trailing edge, the baseline case indicates a relatively focused region of gray which corresponds well with the location of the average vortex (seen in figure 4.3). With suction applied, the frequency of the "blobs" is considerably decreased, but the area over which they occur remains about as large as the baseline case. In addition, the sizes of the "blobs" now remain relatively constant for both the baseline and suction case.

At one radius from the trailing edge, the baseline case suggests that the lateral area covered by the vortex increases, and the frequency (with a vorticity level of $-25s^{-1}$ or more) decreases from that of the trailing edge baseline case. With applied suction, little to no qualitative difference is observed in the behavior of the "blobs", which suggests (as found for Reynolds-stresses) that the influence of suction of the vortex leg dynamics diminishes with streamwise distance.

In conclusion, figures 4.10 (a) and (b) imply that suction will reduce buffeting experienced by any structures in the junction wake flow (up to the trailing edge) by diminishing the unsteady motion of the vortex legs. Figure 4.10 (c), however suggests that this reduction of buffeting would not apply much beyond the one radius downstream location.

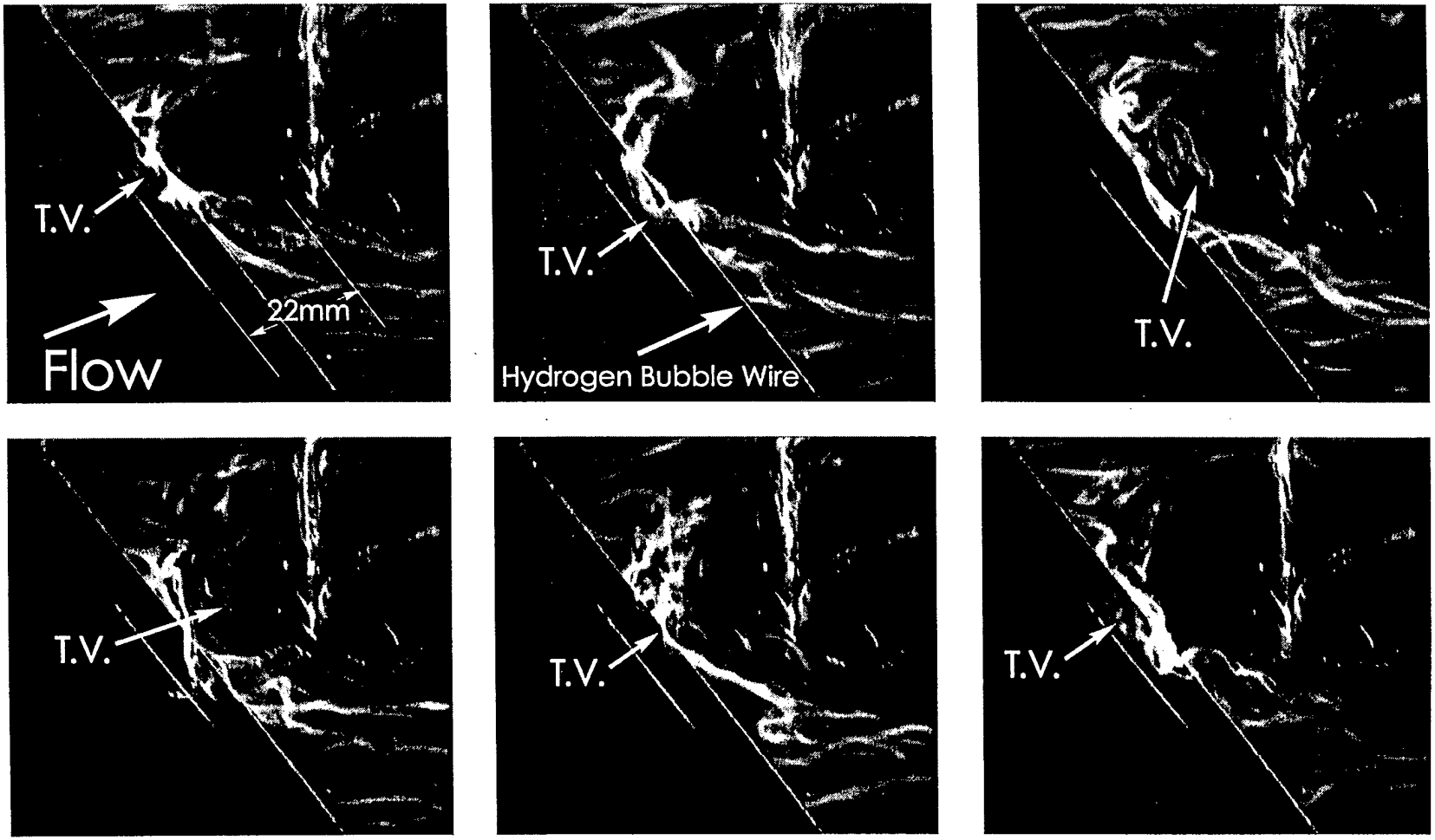

Figure 4.1 Selected hydrogen bubble visualizations of a turbulent necklace vortex (T.V.). Cylinder located 92.2cm from the leading edge, wire located 20mm from the cylinder and 6mm off surface. U_∞=12.5 cm/s, Re_L=1.1x10^5, and Re_{δ^*}=434.6.

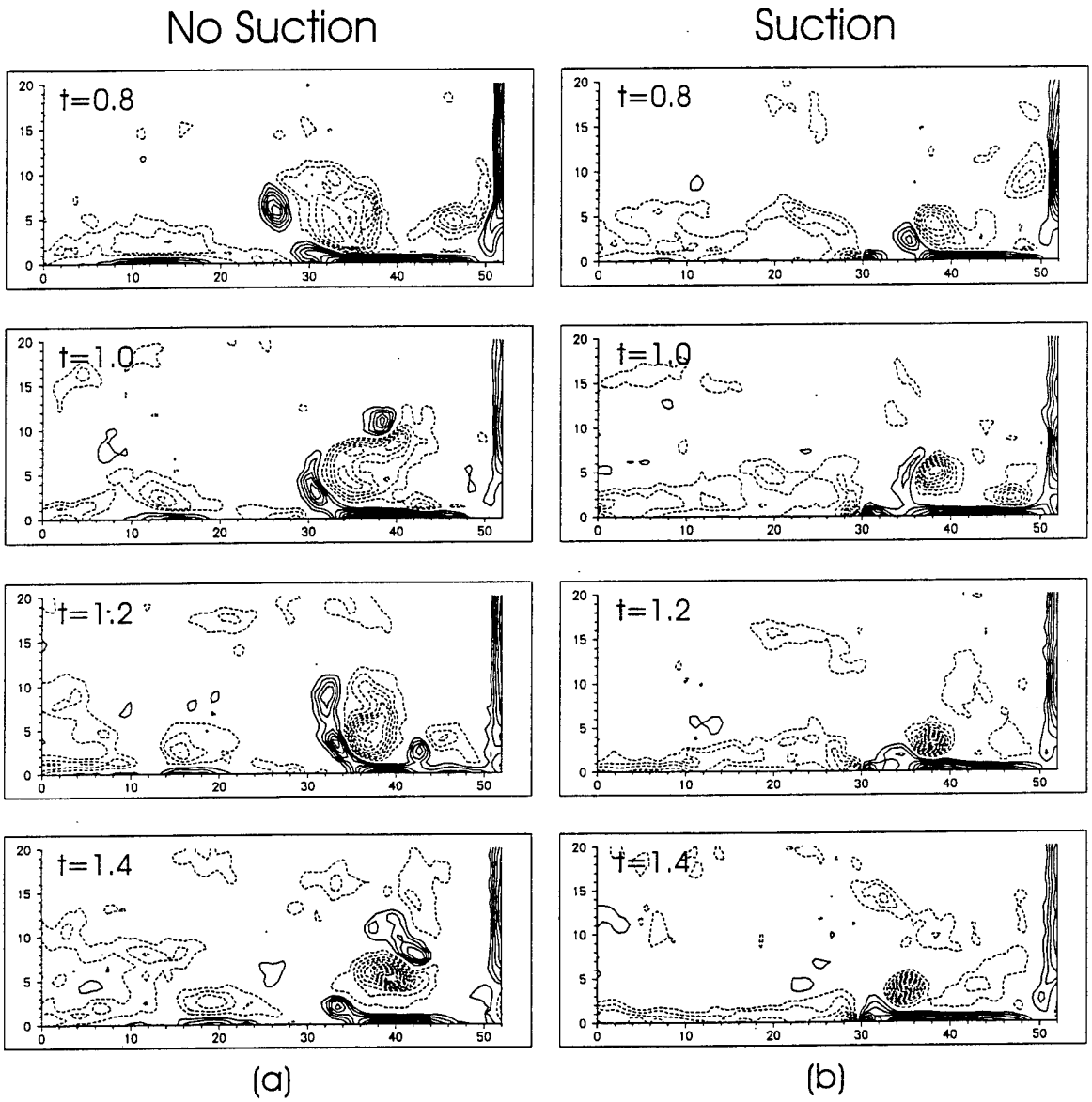

Figure 4.2 Selected sequences of instantaneous vorticity plots (from figures A.1 and A.2) of the flow on the symmetry plane of a cylinder-flat plate junction (a) without suction and (b) with suction ($V_{suction}/U_{\infty}$=0.68). Contours are -150 to 150 in intervals of 10 s^{-1}; dashed lines indicate negative values and solid lines positive values (the 0 s^{-1} contour has been excluded for clarity). Conditions the same as figure 4.1. Dimensions in millimeters.

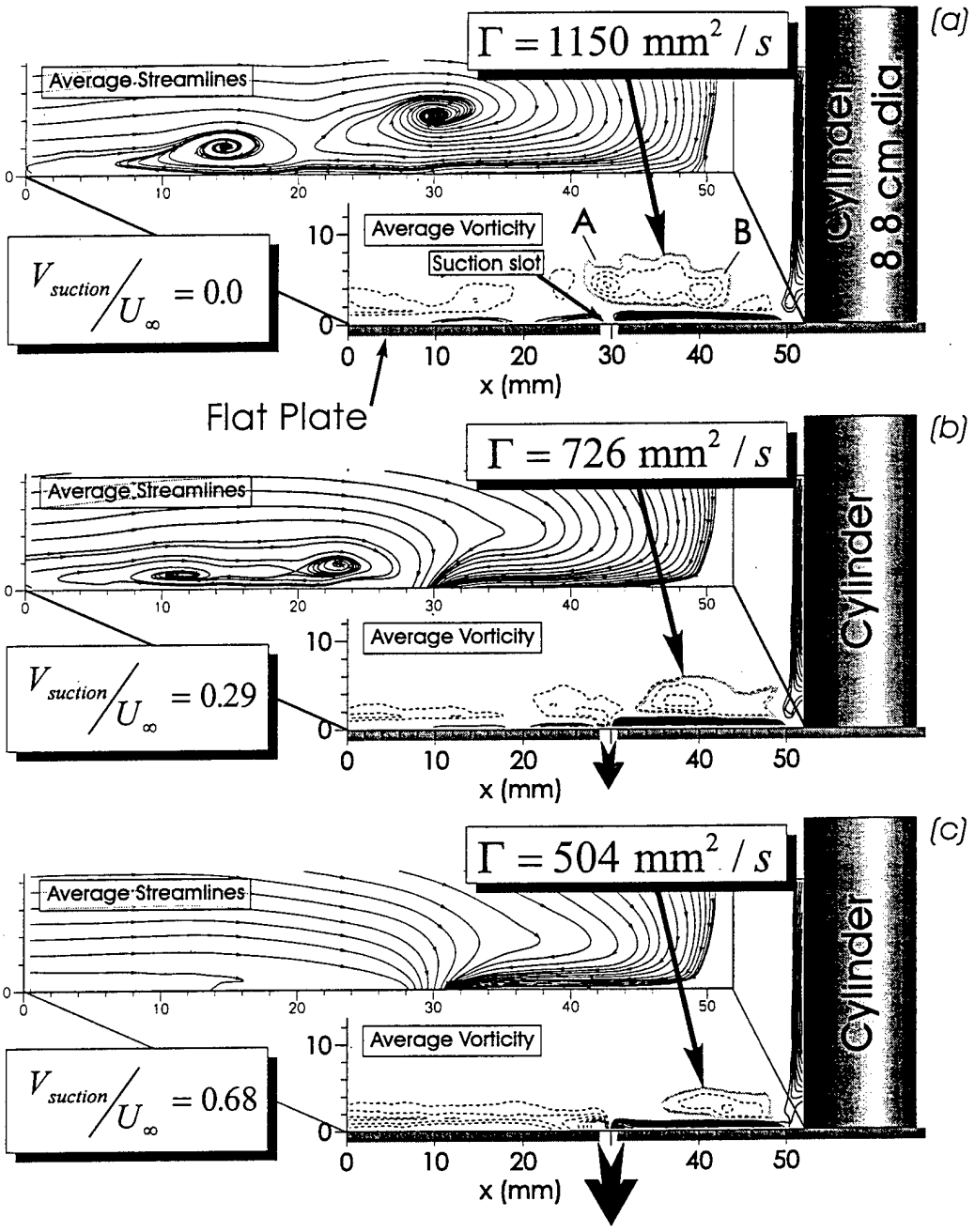

Figure 4.3 Average symmetry plane streamline and vorticity contour plots (of 33-36 instantaneous datasets acquired at 2 Hz) illustrating the effect of constant-rate suction on a turbulent necklace vortex system. Contour intervals are -40 to -10 and 10 to 80 in increments of 5 s^{-1}, dashed lines indicate negative vorticity and solid lines positive vorticity. ω=-10s^{-1} was the contour level used for calculation of the circulation strength Γ. (a) No suction, (b) moderate suction, (c) max suction. Conditions the same as figure 4.1.

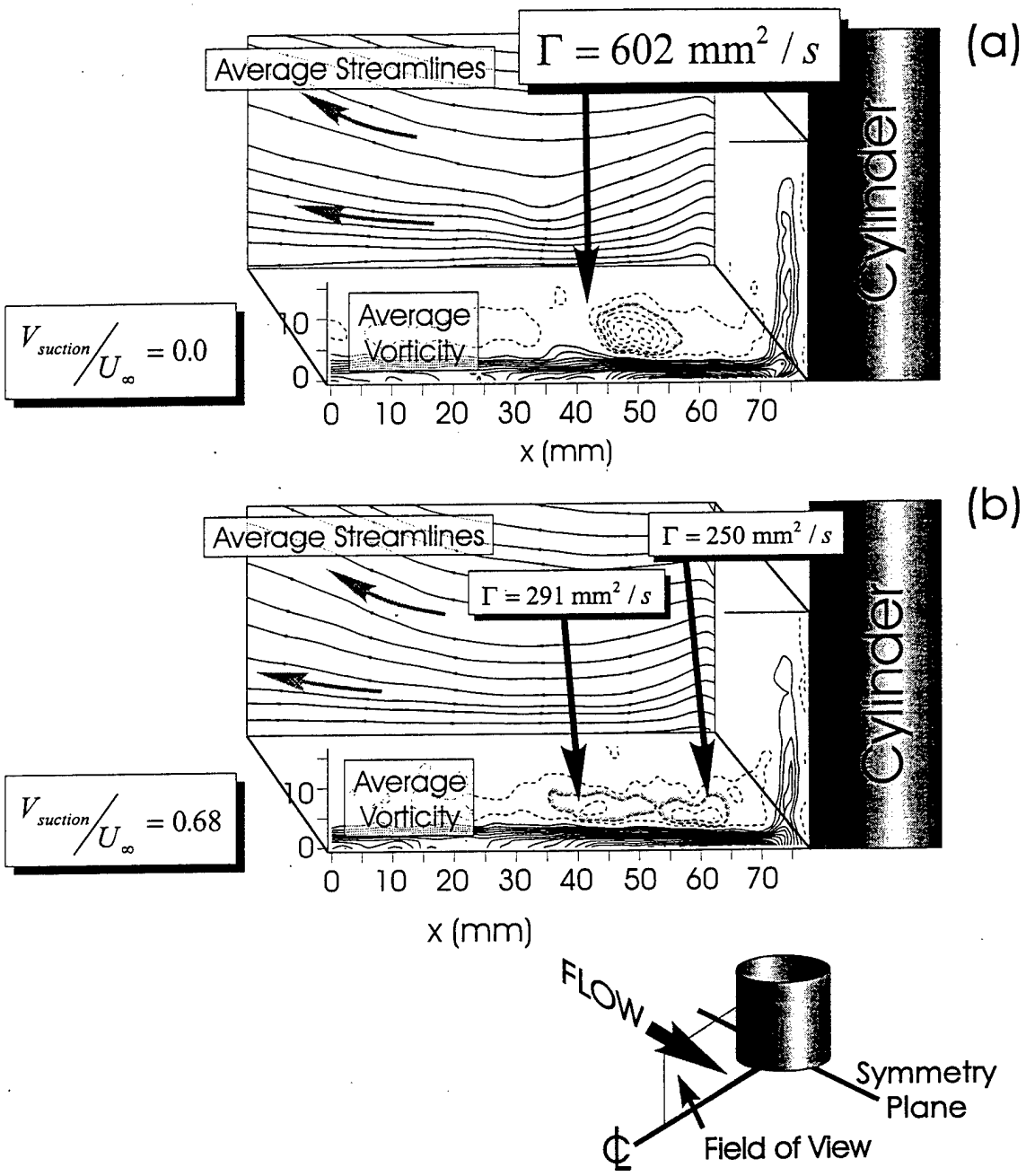

Figure 4.4 Average end-view streamline and vorticity contour plots (of 33-36 instantaneous datasets acquired at 5 Hz) illustrating the effect of constant-rate suction on a turbulent necklace vortex system. Contour intervals are -46 to -2 and 2 to 46 in increments of 2 s^{-1}; dashed lines indicate negative vorticity and solid lines positive vorticity. ω=-4s^{-1} is the contour level used for the calculation of the circulation strength Γ. Conditions the same as figure 4.1.

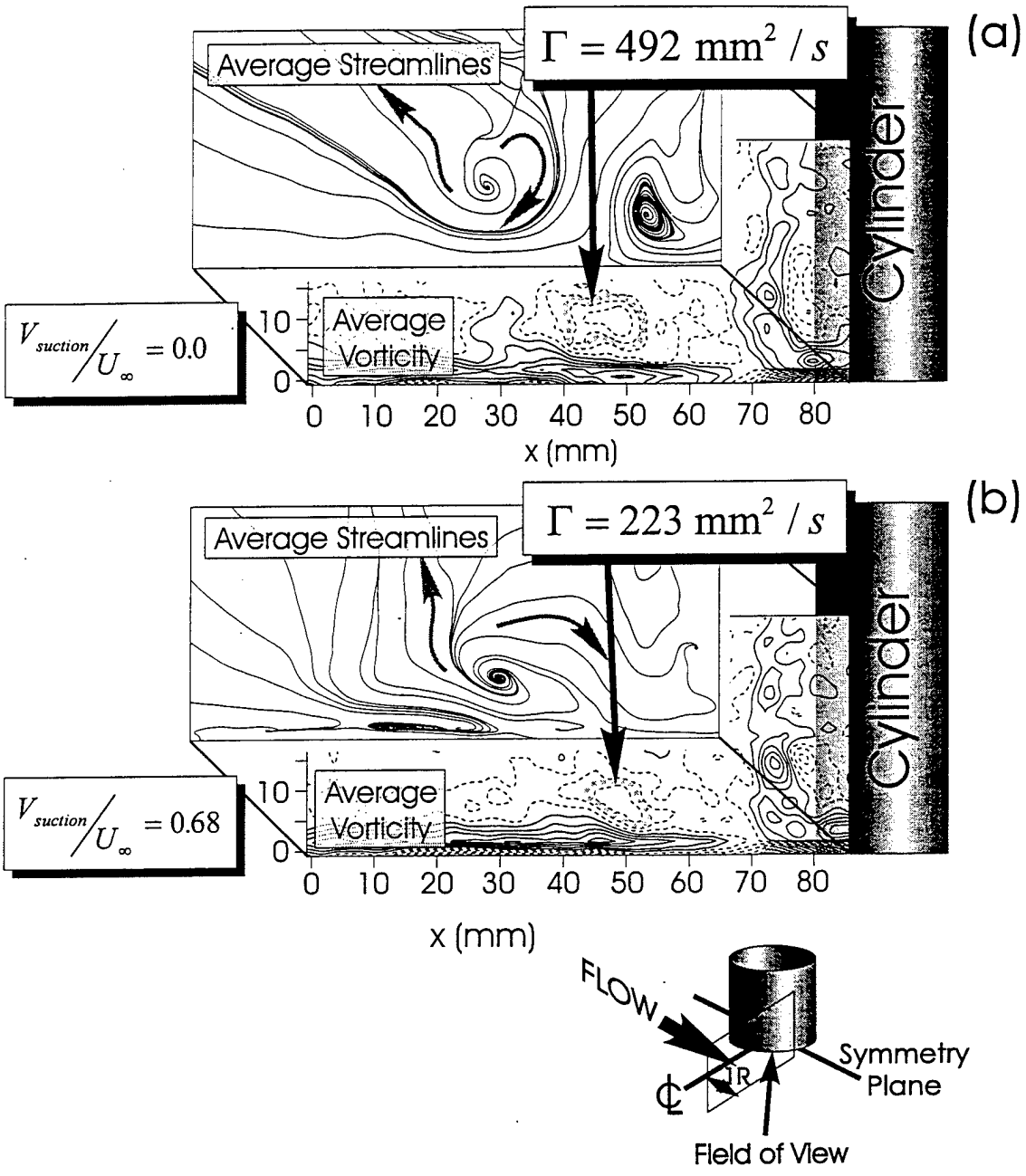

Figure 4.5 Average end-view streamline and vorticity contour plots (of 33-36 instantaneous datasets acquired at 5 Hz) illustrating the effect of constant-rate suction on a turbulent necklace vortex system. Contour intervals are -45 to -1 and 1 to 45 in increments of 2 s^{-1}; dashed lines indicate negative vorticity and solid lines positive vorticity. ω=-6s^{-1} is the contour level used for the calculation of the circulation strength Γ. Conditions the same as figure 4.1.

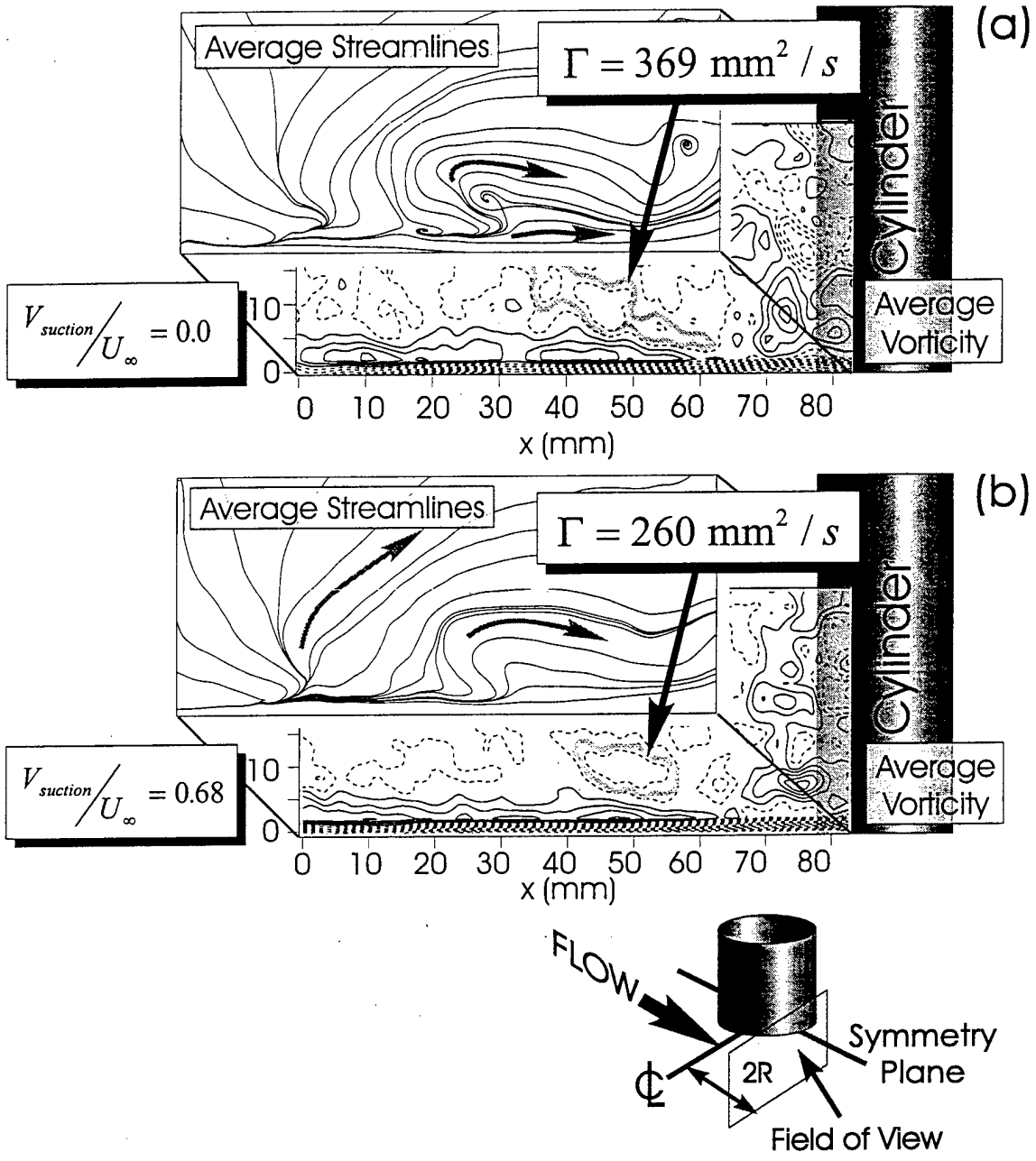

Figure 4.6 Average end-view streamline and vorticity contour plots (of 33-35 instantaneous datasets acquired at 5 Hz) illustrating the effect of constant-rate suction on a turbulent necklace vortex system. Contour intervals are -45 to -1 and 1 to 45 in increments of 2 s^{-1}; dashed lines indicate negative vorticity and solid lines positive vorticity. ω=-2s^{-1} is the contour level used for the calculation of the circulation strength Γ. Conditions the same as figure 4.1.

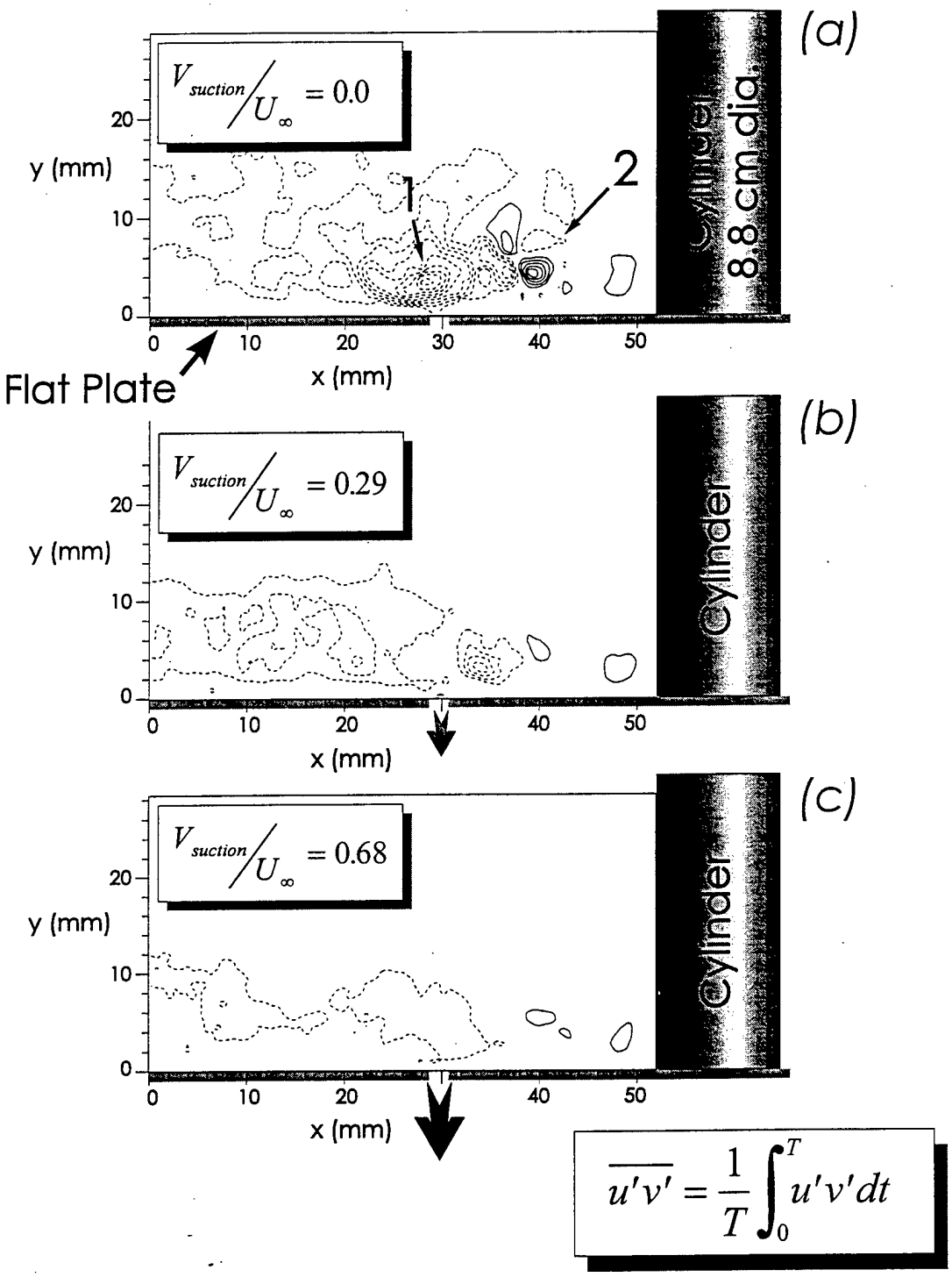

Figure 4.7 Symmetry plane Reynolds-stress plots calculated using 33-36 instantaneous datasets acquired at 2 Hz. Contour intervals are -450 to -50 and 50 to 250 in increments of 50 mm^2/s^2; dashed lines indicate negative values and solid lines positive values. Conditions the same as figure 4.1.

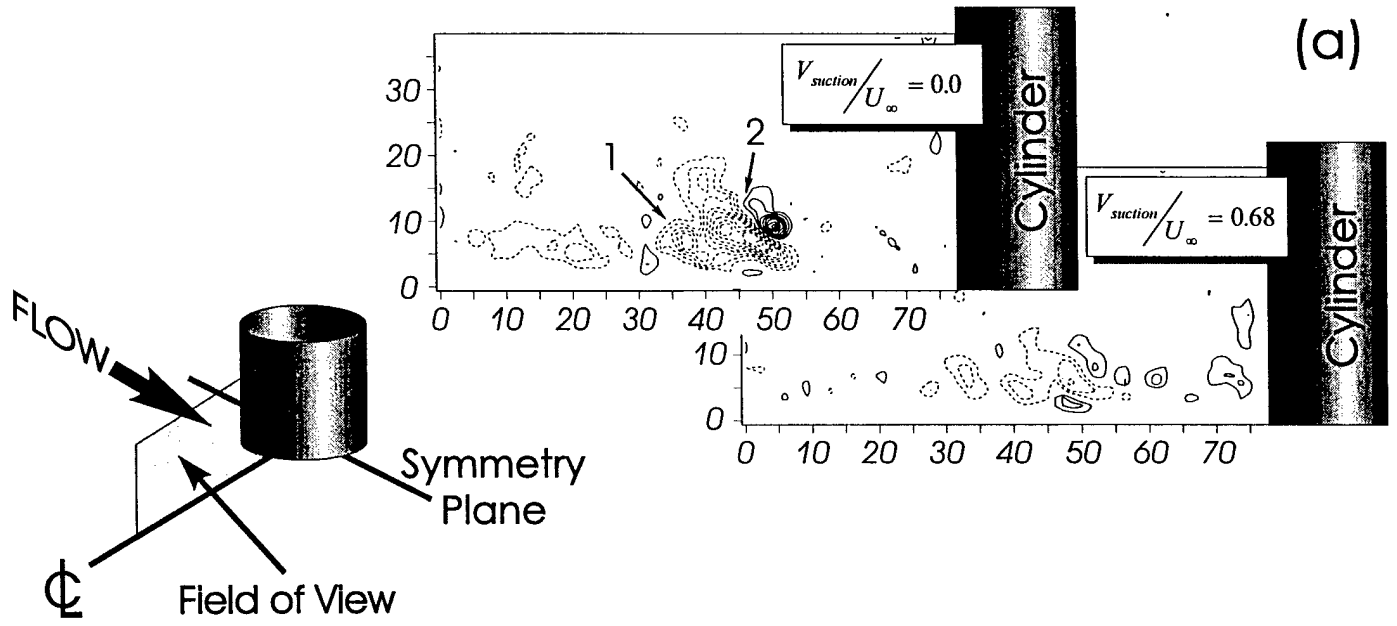

Figure 4.8 End-view Reynolds-stress plots calculated using 33-36 instantaneous data sets acquired at 5 Hz. Contour intervals are -180 to -20 and 20 to 180 in increments of 20 mm^2/s^2; dashed lines indicate negative values and solid lines positive values. (a) Medial cross-stream plane, (b) trailing edge cross-stream plane, and (c) one radius downstream cross-stream plane. Conditions the same as figure 4.1.

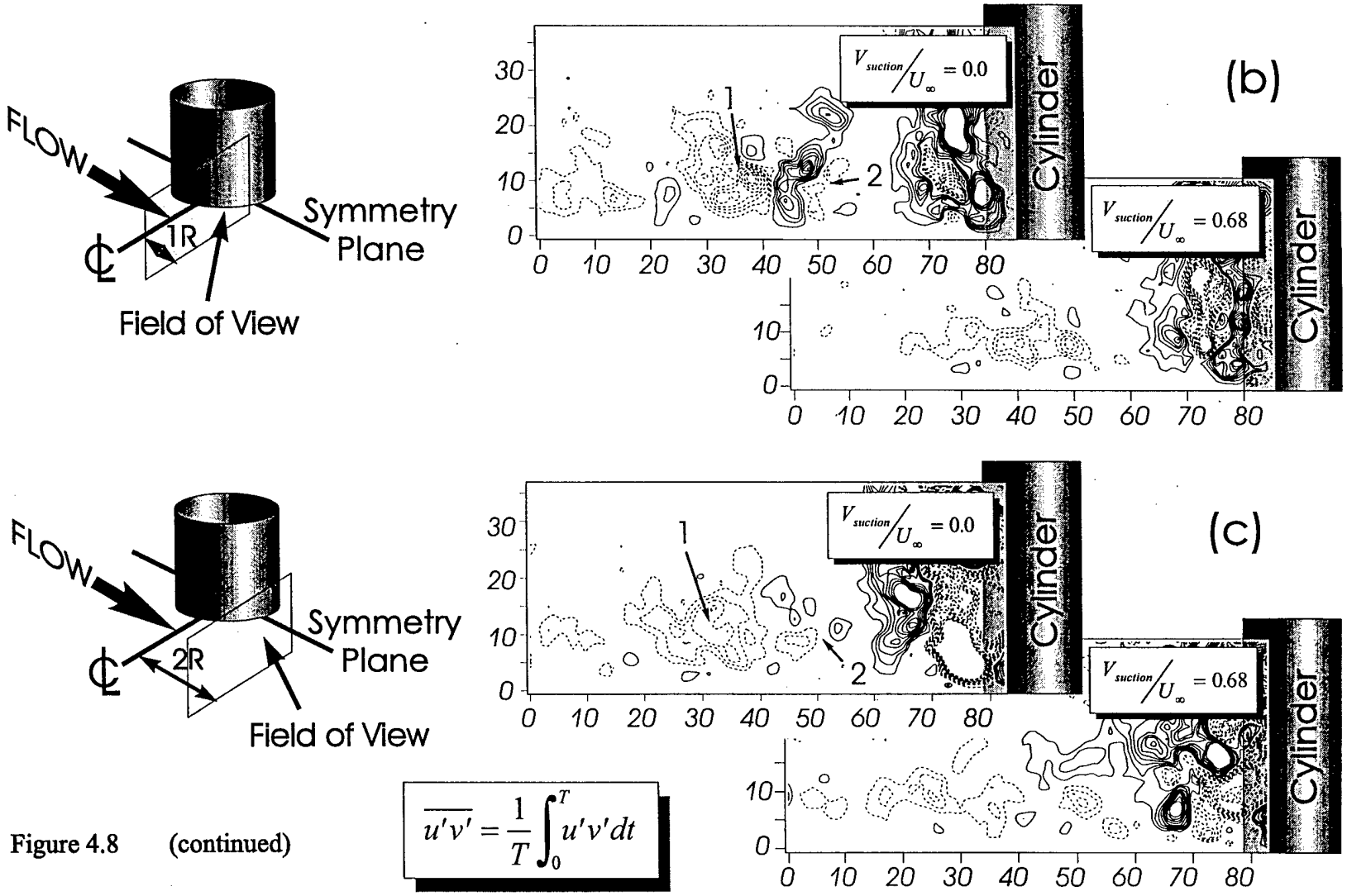

$$\overline{u'v'} = \frac{1}{T}\int_0^T u'v'dt$$

Figure 4.8 (continued)

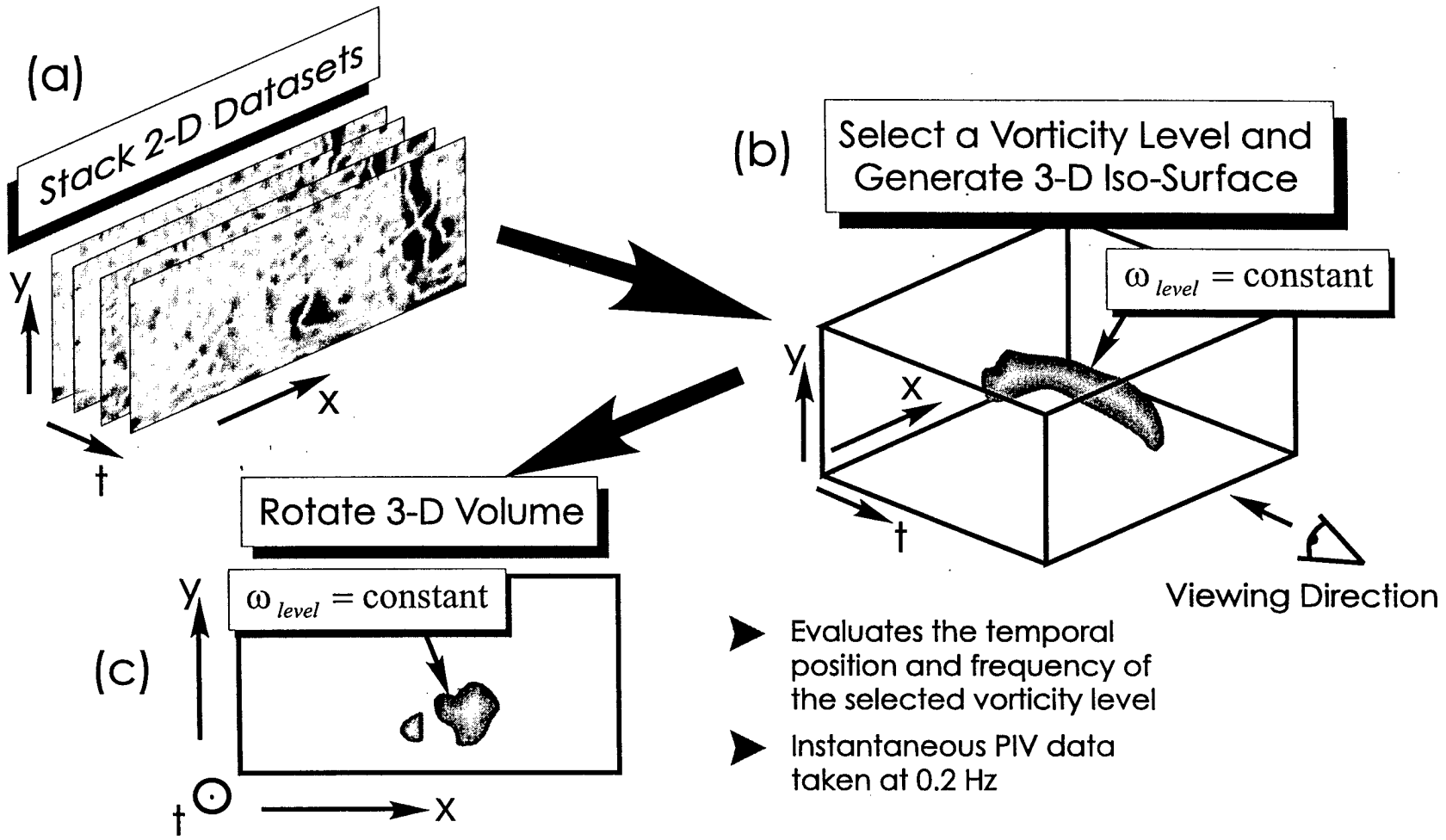

Figure 4.9 Schematic illustrating the method used to determine the effects of suction on the vorticity dynamics of the vortex legs (figures 4.4 through 4.6).

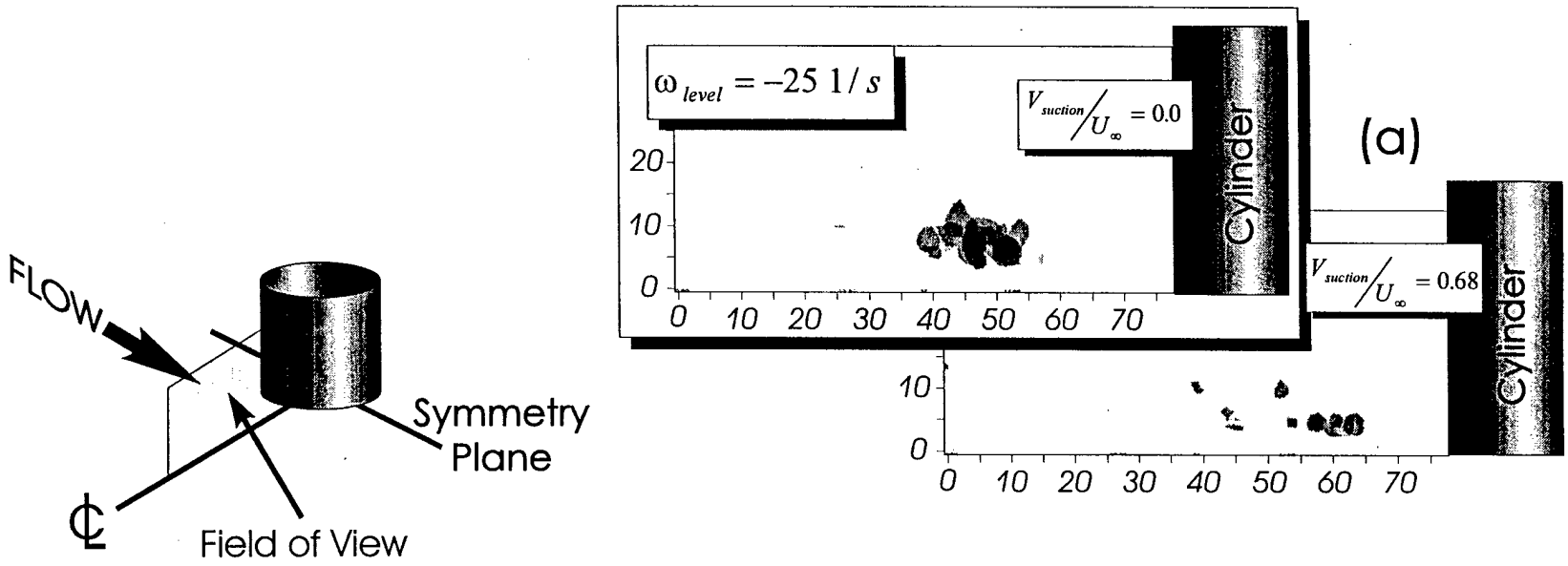

Figure 4.10 End view of an iso-surface plot illustrating the effect of suction on the behavior of the legs of a turbulent necklace vortex.

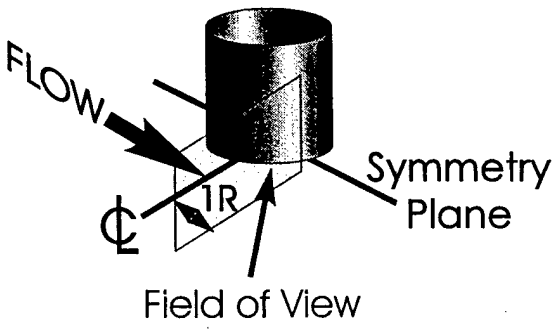

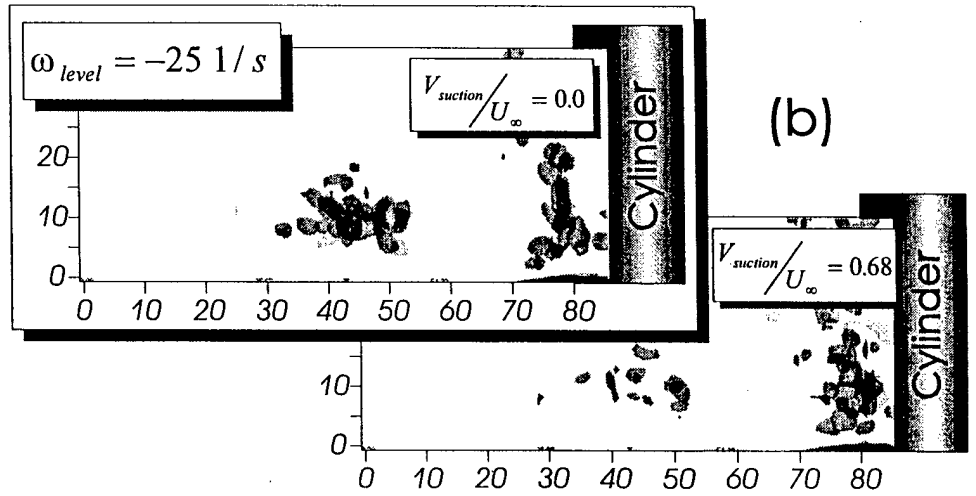

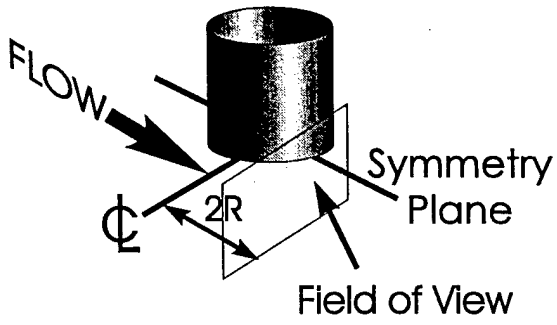

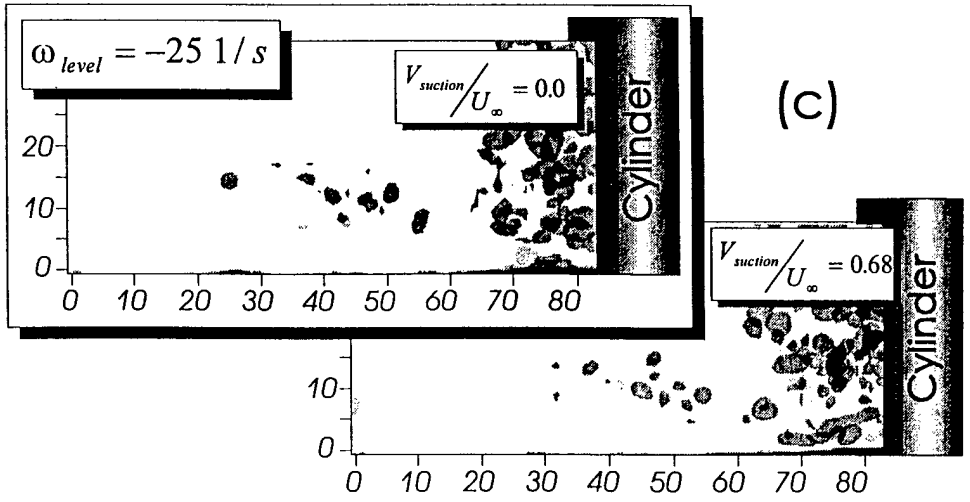

Figure 4.10 (continued)

5.0 SUMMARY and CONCLUSIONS

5.1 Laminar Flow

Control of an unsteady laminar necklace vortex system (formed at a cylinder-flat plate junction, in the breakaway regime) using constant rate surface suction applied through a cross-stream slot of limited spatial extent was examined in detail using hydrogen bubble visualizations for suction rates up to 101% of the free-stream velocity U_∞ and various slot locations relative to the cylinder. It was determined that control of this type is unable to completely eliminate the formation of a necklace vortex system. However, it was observed that this type of control scheme can be effective in *modifying the behavior and topology* of the initial system. The modification generally takes one of four possible forms, depending on slot location and suction rate: 1) a segmentation of the unsteady necklace vortex system into two or more separate vortex systems; 2) the formation of a "braid" system, wherein a complicated interaction between two adjacent necklace vortices arises adjacent to the sides of the cylinder; 3) a modification of the strength and periodicity of the original vortex system; 4) an elimination of the advecting necklace vortex when it encounters the suction slot. Therefore, spatially-limited suction provides a viable alternative to the distributed suction methods of previous studies. It was also observed that the "braid" system displays discrete three-dimensional vortex-vortex and vortex-surface interactions reminiscent of those observed in turbulent

boundary layers, making this system an ideal test-bed for the study of such three-dimensional interactions.

It as observed that at the higher suction rates the edges of the slot were sources of streamwise vorticity; however, preliminary visualizations performed using a curved suction slot indicate that curving the slot could possibly eliminate this vorticity generation effect.

Analysis of detailed Particle Image Velocimetry (PIV) data taken on the symmetry plane indicates that the impinging boundary layer instability is the mechanism which dictates the frequency of the unsteady laminar system, which suggests that the frequency of the unsteady laminar system is susceptible to control via external perturbations. Experiments showed that over a narrow range of frequencies, bracketing the natural formation/breakaway frequency, external perturbation of an unsteady laminar system can be used to override the natural formation/breakaway frequency. Additionally, it was established that a critical disturbance exists, which will artificially trip the laminar junction flow into the transitional flow regime (characterized by turbulent-like flow patterns).

In addition, several passive control devices (i.e. a fillet, control rings, and geometric modification of the flat plate), were cursorily examined using hydrogen bubble visualization to asses their impact on an unsteady laminar necklace vortex system. Interpretation of these results indicates that:

1. Control rings (circular disk-shaped fins mounted on the bluff body) can effectively modify a laminar, unsteady necklace vortex system by segmenting the original system into several smaller-scale steady and unsteady systems
2. A filleted cylinder can eliminate the unsteady necklace vortex system upstream of the cylinder, but residual, steady, vortex legs form outboard of the cylinder.
3. Location of a curved depression in flat plate upstream of a cylinder was observed to modify the unsteady laminar necklace vortex system to a system composed of many steady vortices.

5.2 Turbulent Flow

The effect of spatially limited constant-rate suction (ranging from 0% to 68% of the free-stream velocity U_∞) on a turbulent necklace vortex formed at the junction of a cylinder and flat plate was studied using PIV techniques, with data taken in the symmetry and three downstream, cross-stream, planes. Detailed analysis of these results indicates:

1. Spatially limited surface suction effectively weakens the instantaneous vortex-surface interactions occurring in the vortex system.
2. Spatially-limited suction effectively weakens or eliminates the turbulent necklace vortex on the symmetry plane region.
3. The downstream extensions of the turbulent necklace vortex can be weakened by the application of suction; however the effect of the suction apparently diminishes with streamwise distance.

4. The averaged Reynolds-stress levels in the symmetry and downstream planes can be effectively reduced via surface suction.

Therefore, spatially limited suction again provides a viable (and relatively simple) alternative to the distributed suction methods of previous studies.

5.3 Recommendations

An important observation is that no matter the type of control applied (in this study), the unsteady laminar necklace vortex system was *never* eliminated completely. In fact, the results of the present study suggest that complete removal of the laminar system is not possible with the control methods examined here (e.g. spatially limited suction, fillets, control rings, and circular wall depressions). If total elimination of the laminar system is desired, it is likely that an extension of spatially limited suction, employing several suction slots located at critical points in the flow might work. For example, a promising configuration would employ one slot in the formation region, one in the translation region and one in the corner region. This multiple slot configuration would be similar to the distributed suction methods employed by Goldsmith (1961) and Phillips *et al.* (1992), but would employ far fewer (and simpler) suction orifices and could possibly be effective at suction rates lower than those used by Goldsmith and Phillips.

One particular application of control to a laminar system might involve the flow in the blade-hub junctions of turbomachinery, where velocities are large, but small length scales could result in laminar flow. The unsteady laminar necklace vortex system will cause significant local temperature gradients (Praisner *et al.*, 1997) on the hub surface; these time-varying thermal gradients could contribute to thermal fatigue of the hub.

Because of the small length scales, filleting of a junction may not be possible or practical, and also because turbomachinery blades must periodically be replaced and any complicated geometric shape at the junction could make this replacement difficult. An attractive solution could be the application of suction upstream of the blades, through small slots, with the intention of not removing the vortices, but instead modifying their behavior from unsteady to steady. This flow modification has the benefit of locating the "hot spots" at known locations so that the hub material could be reinforced or treated accordingly.

The turbomachinery problem described above can also be used as an example for turbulent junction flow control. Downstream of the initial rows of rotors and stators, the junction flow is turbulent and the turbulent necklace vortex creates a "hot spot", which contributes to thermal fatigue. Weakening or eliminating the vortex would reduce these thermal gradients, but as mentioned above a fillet may not be possible or desirable. Suction may again be an attractive approach, since the present study indicates that spatially-limited suction can effectively eliminate the turbulent vortex on the symmetry plane and weaken the vortex legs.

Another interesting control possibility is raised by the present study's curved suction slot results, which suggest that it may be possible to construct a suction slot that facilitates fluid exchange in the slot using only the pressure gradients inherent in the flow. This could be particularly attractive when considering the recommendation above regarding the use of multiple slots for elimination of the laminar vortex system. Perhaps implementation of these passive "self-powered" slots alone, or in combination with the active suction slots, could significantly modify, if not eliminate, the laminar and turbulent necklace vortex systems.

References

Acalar, M. S., and Smith, C. R., 1987a, "A study of hairpin vortices in a laminar boundary layer, part 1. Hairpin vortices generated by a hemisphere protuberance," *Journal of Fluid Mechanics*, Vol. 175, pp. 1-41.

Adrian, R. J., "Image Shifting Technique to Resolve, Directional Ambiguity in Double-Pulsed Velocimetry," *Applied Optics*, Vol. 25, 1986, pp. 3855-3858.

Adrian, R. J., 1991, "Particle-imaging techniques for experimental fluid mechanics," *Annual Review of Fluid Mechanics*, Vol. 23, pp. 261-304.

Baker, C. J., "The laminar horseshoe vortex," *Journal of Fluid Mech.*, Vol. 95, part 2, 1979, pp. 347-367.

Bandyopadhyay, P. R., 1994, "Corner vortex suppressor," *United States Patent* 5,303,882, Apr. 19.

Bushnell, D. M., and Donaldson, C. D., 1990, "Control of submersible vortex flows," *NASA Technical Memorandum* #102693, June.

Coon, M. D., and Tobak, M., "Experimental Study of Saddle Point of Attachment in Laminar Juncture Flow," *AIAA Journal*, Vol. 33, No. 12, 1995, pp. 2288-2292.

Devenport, W. J., and Simpson, R. L., "Time-dependent structure in wing-body junction flows," *Turbulent Shear Flows*, Vol. 6, Springer-Verlag, Berlin, 1989, pp. 222-248.

Devenport, W. J., Simpson, R. L., Dewitz, M. B., and Agarwal, N. K., 1992, "Effects of a leading-edge fillet on the flow past an appendage-body junction," *AIAA Journal*, Vol. 30, No. 9, pp. 2177-2183.

Doligalski, T. L., Smith C. R., and Walker, J. D. A., "Vortex interactions with walls," *Annual Review of Fluid Mechanics*, Vol. 26, 1994, pp. 573-616.

Goldsmith, J., 1961, "Laminar flow at the juncture of two aeroplane components," *Boundary Layer and Flow Control, Its Principles and Application*, Vol. 2, Pergamon Press, Oxford, pp. 1000-1006.

Greco, J. J., "The flow structure in the vicinity of a cylinder-flat plate junction: flow regimes, periodicity, and vortex interactions," *M.S. Thesis*, Department of Mechanical Engineering and Mechanics, Lehigh University, Bethlehem, PA, USA, 1990

Gupta, A. K., 1987, "Hydrodynamic modification of the horseshoe vortex at a vertical pier junction with ground," *Physics of Fluids*, Vol. 30, No. 4, pp. 1213-1215.

Haidari, A. H-., 1990, "Generation and growth of single hairpin vortices," *Ph.D. Dissertation*, Department of Mechanical Engineering and Mechanics, Lehigh University, Bethlehem, PA

Hung, C. M., Sung, C. H., and Chen, C. L., "Computation of Saddle Point of Attachment," AIAA Paper 91-1713, June 1991.

Kline, S. J. and McClintock, F. A., 1953, "Describing uncertainties in single-sample experiments," *Mechanical Engineering*, January, p. 3.

Kubendran, L. R., Bar-Sever, A., and, Harvey, W. D., 1988, "Flow Control in a wing/fuselage-type juncture," AIAA Paper AIAA-88-0614, AIAA 26th Aerospace Sciences Meeting, Jan. 11-14, Reno, NV.

Landreth, C. C., Adrian, R. J., and Yao, C. S., "Double Pulsed Particle Image Velocimeter with Directional Resolution for Complex Flows," *Experiments in Fluids*, Vol. 6, 1988 pp. 119-128.

Lugt H. J., 1981, "Numerical modeling of vortex flows in ship hydrodynamics, a review," *The Proceedings of the Third International Conference on Numerical Ship Hydrodynamics*, June 16-19, Paris, France, pp. 297-316.

Lugt, H. J., 1983, Vortex Flow in Nature and Technology, John Wiley & Sons, New York

Monkewitz, P. A., and Huerre, P., "Influence of the velocity ratio on the instability of mixing layers," *Physics of Fluids*, vol. 25, No. 7, 1982, pp. 1137-1143.

Oschwald, M., Bechle, S., and Welke, S., "Systematic Errors in PIV by Realizing Velocity Offsets with the Rotating Mirror Method," *Experiments in Fluids*, Vol. 18, 1995, pp. 329-334.

Panton, R. L., Incompressible Flow, John Wiley and Sons, New York, 1984, pp. 510-513.

Peridier, V. J., Smith, F. T., and Walker, J. D. A., "Vortex-induced boundary-layer separation. Part 1. The unsteady limit problem $Re \rightarrow \infty$," *Journal of Fluid Mech.*, vol. 232, 1991, pp. 99-131.

Perry, A. E., and Steiner, T. R., "Large-scale vortex structures in turbulent wakes behind bluff bodies. Part 1. Vortex formation Processes," *Journal of Fluid Mechanics.*, vol. 174, 1987, pp. 233-270.

Phillips, D. B., Cimbala, J. M., and Treaster A. L., 1992, "Suppression of the wing-body junction vortex by body surface suction," *Journal of Aircraft*, Vol. 29, No. 1, pp. 118-122.

Praisner, T. J., Seal, C. V., Takmaz, L., and Smith, C. R., 1997, "Spatial-temporal turbulent flow-field and heat transfer behavior in end-wall junctions," *International Journal of Heat and Fluid Flow*, Vol. 18, No. 1.

Puhak, R. I., Degani, A. T., and Walker, J. D. A., "Unsteady Separation and Heat Transfer Upstream of Obstacles," *Journal of Fluid Mechanics*, Vol. 305, 1995, pp. 1-27.

Rockwell, D., Magness, C., Towfighi, J., Akin, O., & Corcoran, T., 1993, "High image-density particle image velocimetry using laser scanning techniques," *Experiments in Fluids*, Vol. 14, pp. 181-192.

Rockwell, D., and Lin, J. C., private communication, Lehigh University, Department of Mechanical Engineering, Bethlehem, PA, USA., December, 1995.

Schwind, R. G., "The three-dimensional boundary layer near a strut," Gas Turbine Laboratory Report Number 67, M.I.T., Boston, MA, USA, 1962.

Seal, C. V., Smith, C. R., Akin, O., and Rockwell, D., 1995, "Quantitative characteristics of a laminar necklace vortex system at a rectangular block-flat plate juncture," *Journal of Fluid Mechanics*, vol. 286, pp. 117-135.

Sullivan, R. D., "A two-cell vortex solution of the Navier-Stokes equations," *Journal of the Aero/Space Sciences*, vol. 26, 1959, pp. 767-768.

Sung, C.-H., Yang, C.-I., and Kubendran, L. R., 1988, "Control of horseshoe vortex juncture flow using a fillet," *Proceedings of the Symposium on Hydrodynamic Performance Enhancement for Marine Applications*, Newport, RI, pp. 13-20.

Thomas, A. S. W., "The unsteady characteristics of laminar juncture flow," *Physics of Fluids*, Vol. 30, 1987, pp. 283-285.

Visbal, M. R., "Structure of Laminar Juncture Flows," *AIAA Journal*, Vol. 29, No. 8, 1991, pp. 1273-1281.

Visbal, M. R., and Gordnier, R. E., "Crossflow topology of vortical flows," *AIAA Journal*, vol. 32, no. 5, 1994, pp. 1085-1087.

Visbal, M. R., private communication, Wright Research and Development Center, Wright-Patterson AFB, OH, USA.

Appendix

Laminar Case

Field of View	*M*	*d/M*	*Δl/M*
Symmetry Plane (both views)	0.44	1.7 mm	1.02 mm
Magnified Symmetry Plane (formation region only)	0.63	1.2 mm	0.6 mm

Turbulent Case

Field of View	*M*	*d/M*	*Δl/M*
Symmetry Plane	0.61	1.25 mm	0.62 mm
0R End View	0.369	2.3 mm	1.15 mm
1R End View	0.385	2.21 mm	1.1 mm
2R End View	0.397	2.14 mm	1.07 mm

Table A.1 Magnification and grid parameters for the laminar and turbulent PIV study.

Frequency	Amplitude (cm/s)	Frequency	Amplitude (cm/s)	Frequency	Amplitude (cm/s)
.14	.04	.18	.028	.14	.397
.24	.068	.3	.047	.2	.567
.31	.088	.39	.061	.24	.68
.37	.105	.47	.074	.28	.794
.39	.111	.52	.082	.31	.879
.41	.116	.55	.087	.34	.964
.44	.125	.61	.096	.39	1.106
.48	.136	.7	.11	.44	1.247
.52	.147	.78	.123	.48	1.361
.56	.159	1.34	.211	.51	1.446
.59	.167	1.69	.266	.55	1.559
.62	.176	2.37	.373	.61	1.729
.69	.196			.85	2.409
1.05	.298	.28	.176		
1.35	.383	.39	.246	.28	.088
1.9	.539	.55	.346	.33	.104
		.67	.422	.35	.11
.2	.283	.77	.485	.37	.117
.28	.397	.86	.542	.39	.123
.34	.482	1.21	.762	.43	.135
.39	.553	1.47	.926	.46	.145
.43	.609	1.69	1.065	.49	.154
.47	.666			.52	.164
.55	.78			.55	.173
.61	.865			.61	.192
.67	.95			.95	.299
.77	1.091			.78	.246
.87	1.233			1.22	.384
1.05	1.488			1.71	.539
1.2	1.701				
1.45	2.055				

Table A.2 Surface velocity perturbation frequencies and amplitudes examined.

Suction Rate (ml/s)	Suction Velocity (cm/s)	Non-Dimensional Suction Velocity ($V_{suction}/U_{\infty}$)	Designation
0	0	0	Low
0.8	0.63	0.08	Low
1.07	0.84	0.10	Low
1.35	1.06	0.13	Low
1.62	1.28	0.15	Low
1.89	1.49	0.18	Moderate
2.33	1.83	0.22	Moderate
2.98	2.35	0.28	Moderate
4.53	3.57	0.43	Moderate
6.68	5.26	0.64	High/Max
8.84	6.96	0.84	High/Max
10.56	8.31	1.01	High/Max

Table A.3 Constant suction rates employed in the present study.

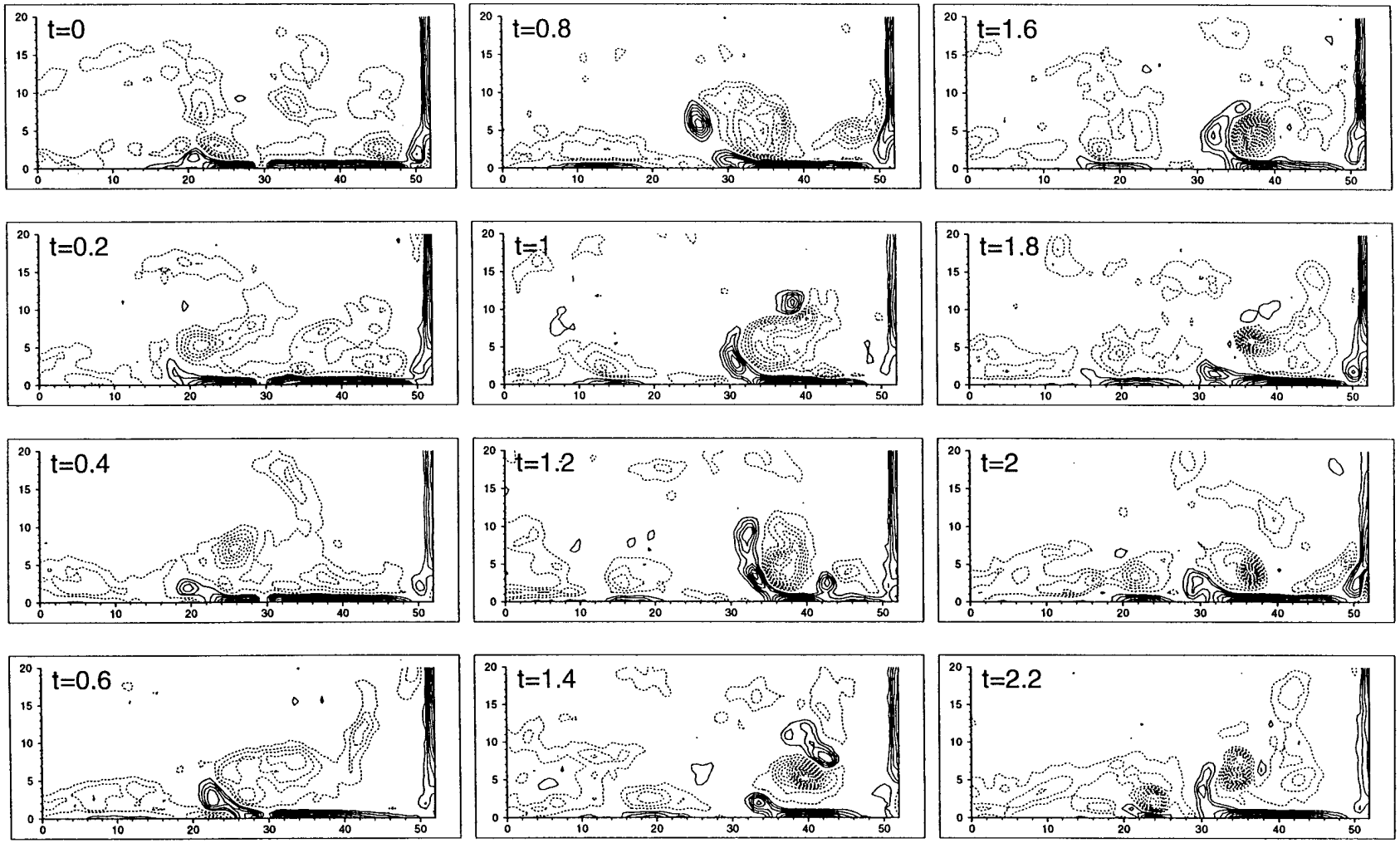

Figure A.1 Temporal vorticity plots on the symmetry plane for flow in a cylinder-flat plate junction with no suction. Vorticity contours are plotted in intervals of 10 s^{-1} from -150 to 150 (excluding the 0 level). Dashed lines indicate negative vorticity; solid lines indicate positive vorticity.

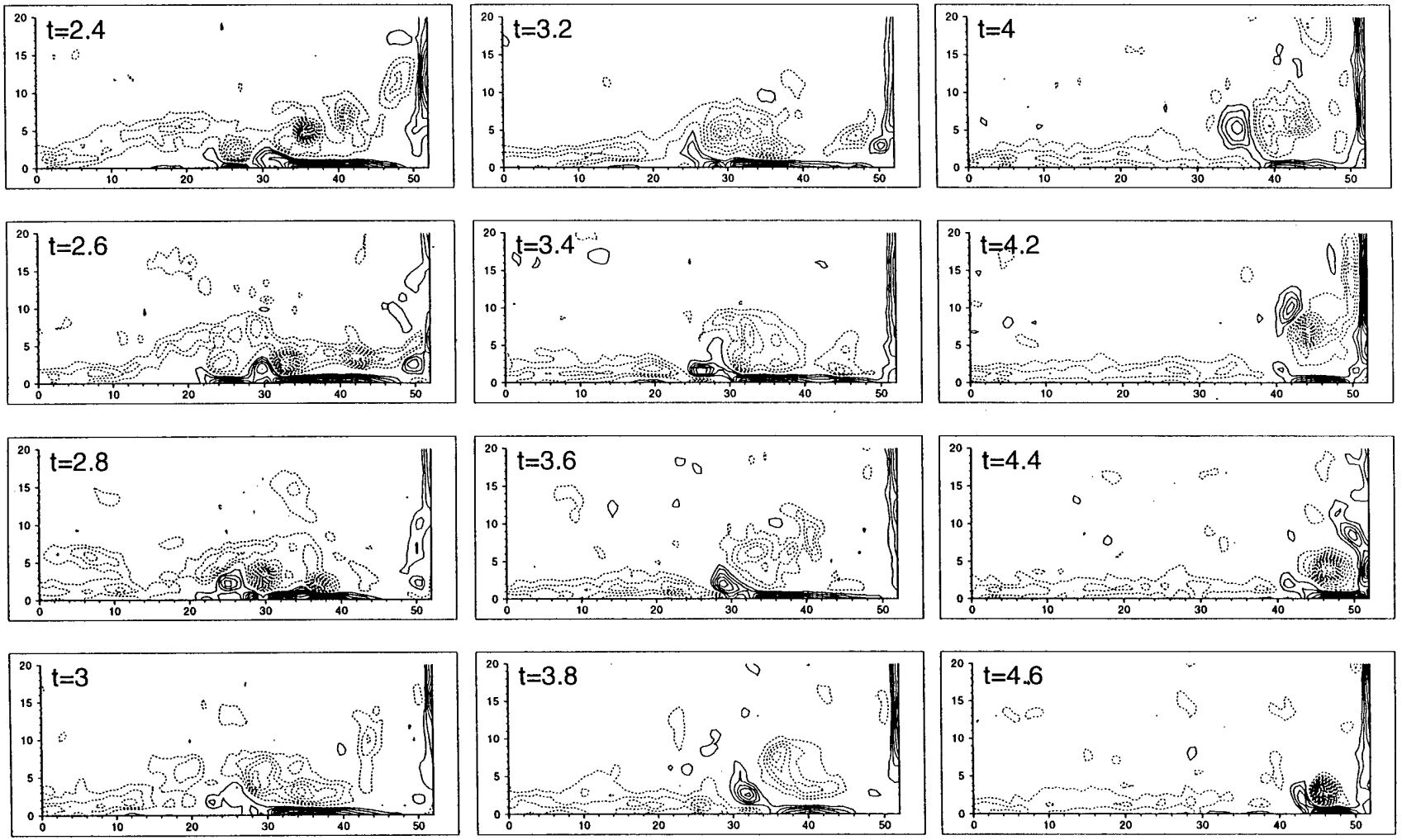

Figure A.1 Continued.

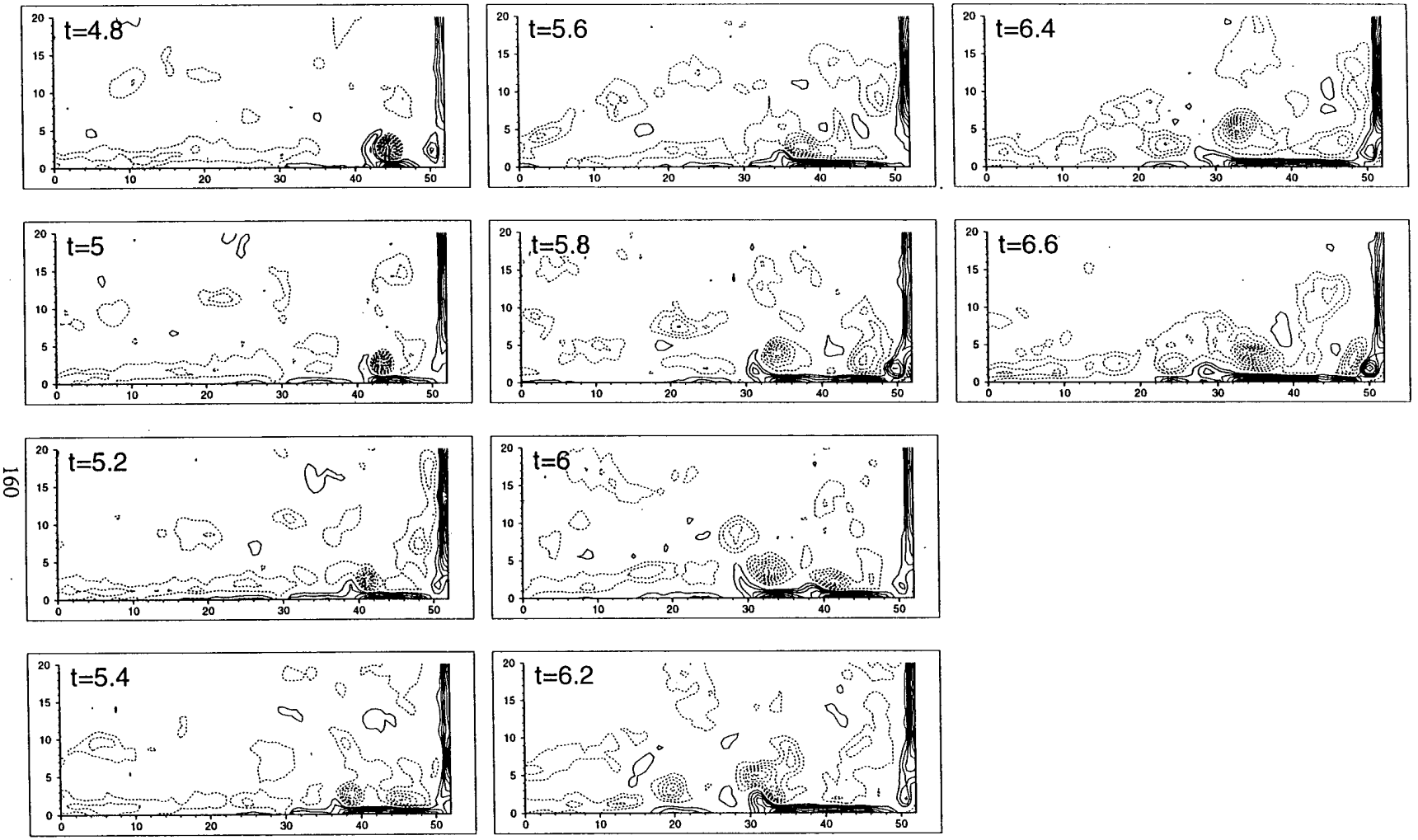

Figure A.1 Continued.

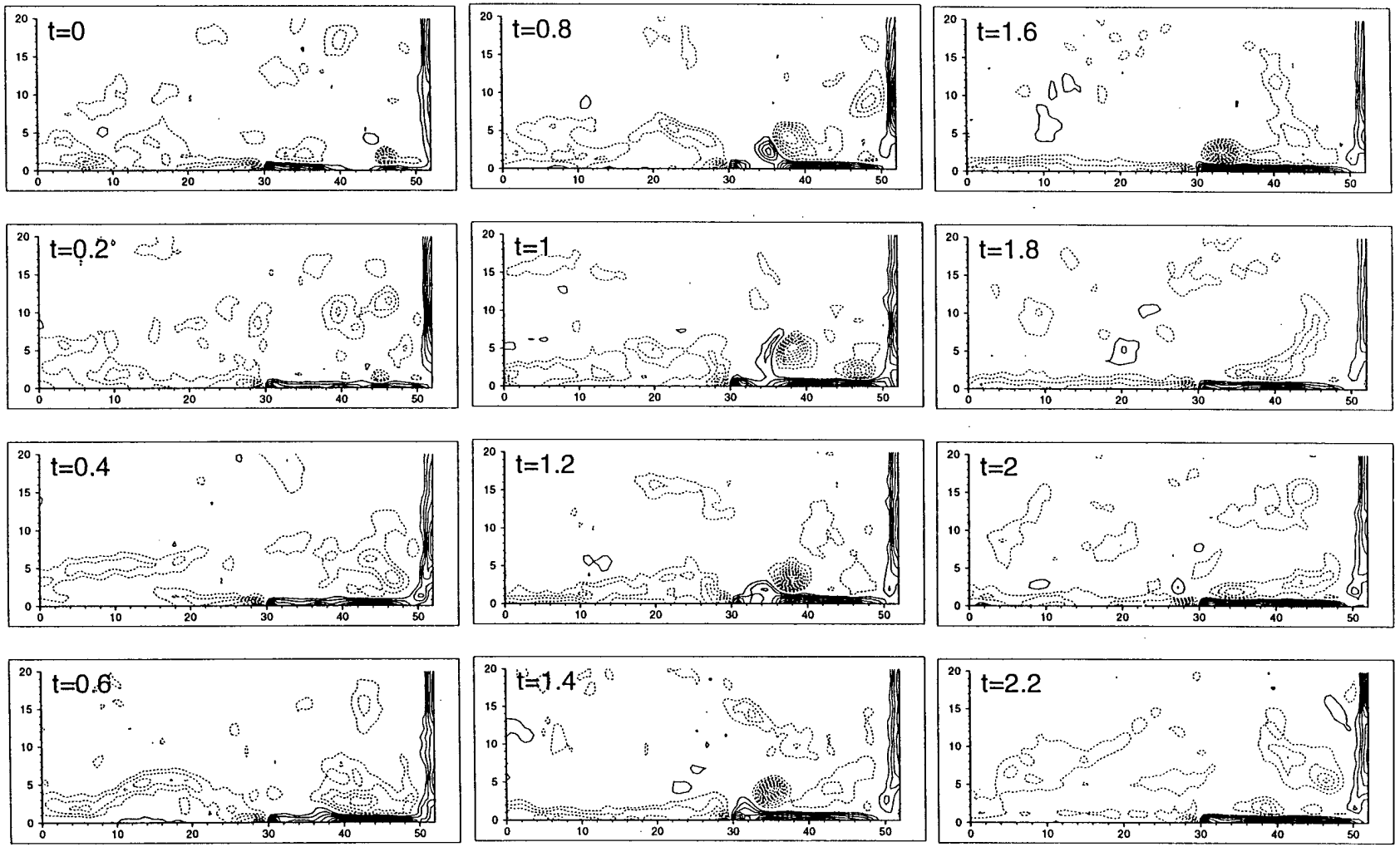

Figure A.2 Temporal vorticity plots on the symmetry plane for flow in a cylinder-flat plate junction with suction applied (68% of the free-stream velocity). Vorticity contours are plotted in intervals of 10 s^{-1} from -150 to 150 (excluding the 0 level). Dashed lines indicate negative vorticity; solid lines indicate positive vorticity.

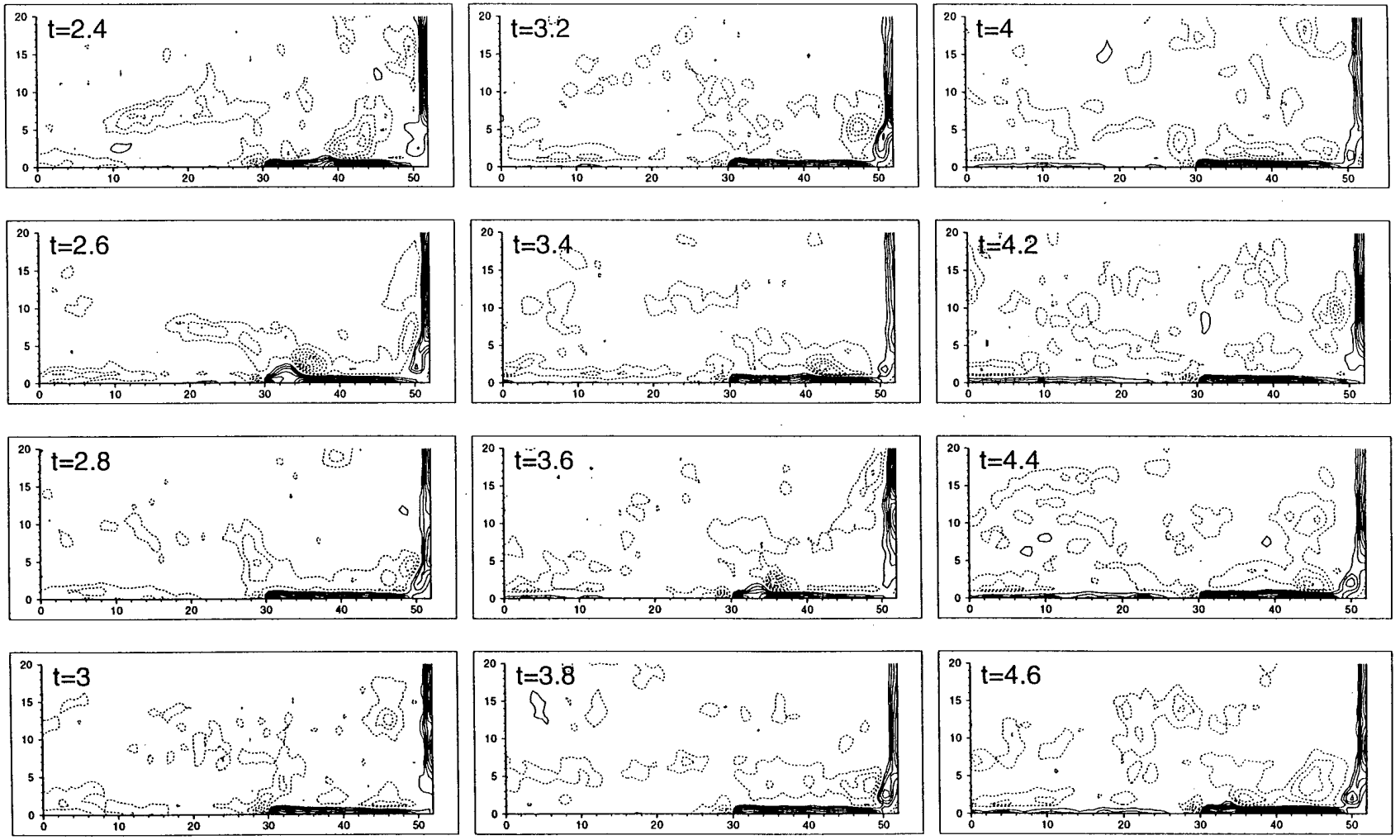

Figure A.2 Continued.

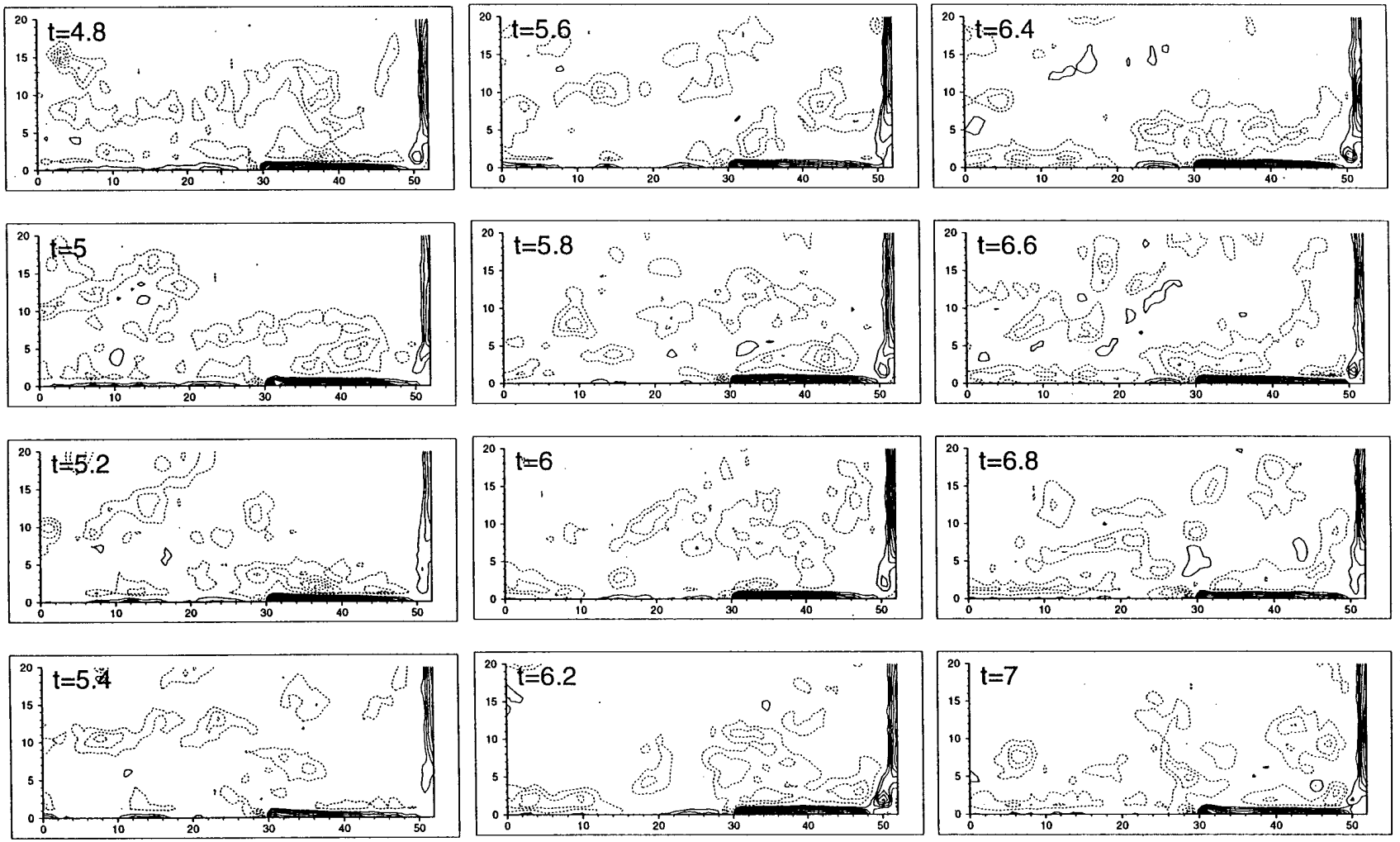

Figure A.2 Continued.

Vita

The author was born in Albany, New York on July 11, 1969 to Charles and Virginia Seal. After graduating from Lakeland Senior High School with honors in 1987, he attended Clarkson University in Potsdam, New York where he received s Bachelor of Science degree in Mechanical Engineering in the spring of 1991. While at Clarkson the author was inducted into the Engineering honor society Tau Beta Pi and the Mechanical Engineering honor society Pi Tau Sigma. Immediately following undergraduate work the author was accepted to Lehigh University as a Fellow, where he earned a Master of Science degree in Mechanical Engineering in October 1993 and a Doctorate in June 1997.

During the course of his graduate work the author has published several articles and presented at meetings of the American Physical Society (APS) and American Institute of Aeronautics and Astronautics (AIAA) (listed below). While at Lehigh the author participated in many extracurricular and service activities, including: summer softball (the Boilermakers), the Graduate Student Counsel, and The Lehigh University Forum. The author also participated several times in the Mechanical Engineering Graduate Student Symposium at Lehigh, winning the S. W. Kung award for best presentation in 1993.

Outside of his research activities, the author enjoys weightlifting, softball, whitewater rafting, and reading. After graduating Lehigh, the author hopes to obtain a position in industry enabling him to use his knowledge of fluid mechanics and experimental methods in an applied research environment.

List of publications and Presentations

"Quantitative characteristics of a laminar, unsteady necklace vortex system at a rectangular block-flat plate juncture", J. Fluid Mech., 1995, v. 286, pp. 117-135

"Quantitative characteristics of a laminar, unsteady necklace vortex system at a rectangular block-flat plate juncture", Presented at the 47th annual DFD APS meeting, November 20-22, 1994, FC-2

"Dynamics of the vorticity distribution in endwall junctions", Presented at the 26th AIAA Fluid Dynamics Conference, June 19-22, 1995, San Diego, CA, AIAA 95-2238

"Dynamics of the vorticity distribution in endwall junctions", Accepted, AIAA J., 1997

"Spatial-Temporal Turbulent Flow-Field and Heat Transfer Behavior in End-Wall Junctions", International J. of Heat and Fluid Flow, Vol. 18, No. 1, 1997

"Spatially-Limited Suction as a Means to Control Turbulent Junction Flows", Presented at the 49th annual DFD APS meeting, November 24-26 1996, Syracuse, NY, FF-04

"Intertwining Laminar Necklace Vortices, " Accepted, Physics of Fluids Gallery of Fluid Motion, 1997

"The Control of Turbulent End-Wall Boundary Layers Using Surface Suction," In Preparation, To be Presented at the 4th AIAA Shear Flow Conference, June 29-July 2, 1997, Snowmass, CO, AIAA 97-2060